MODELLING AND COMPENSATION OF STICK-SLIP FRICTION FOR ROBOT ARM CONTROL

by

Peter D. Tataryn, B.Sc.(ME)

A thesis submitted to the Faculty of Graduate Studies
of the University of Manitoba in partial fulfilment
of the requirements of the degree of

MASTER OF SCIENCE

Department of Mechanical and Industrial Engineering
University of Manitoba
Winnipeg, Manitoba
CANADA R3T 2N2

ISBN 0-612-13525-X

Name Modelling and Compensation of Stick-Slip Friction for Robot Control

Dissertation Abstracts International and *Masters Abstracts International* are arranged by broad, general subject categories. Please select the one subject which most nearly describes the content of your dissertation or thesis. Enter the corresponding four-digit code in the spaces provided.

Mechanical Engineering
SUBJECT TERM

0548
SUBJECT CODE

UMI

Subject Categories

THE HUMANITIES AND SOCIAL SCIENCES

COMMUNICATIONS AND THE ARTS
Architecture 0729
Art History 0377
Cinema 0900
Dance 0378
Fine Arts 0357
Information Science 0723
Journalism 0391
Library Science 0399
Mass Communications 0708
Music 0413
Speech Communication 0459
Theater 0465

EDUCATION
General 0515
Administration 0514
Adult and Continuing 0516
Agricultural 0517
Art 0273
Bilingual and Multicultural 0282
Business 0688
Community College 0275
Curriculum and Instruction 0727
Early Childhood 0518
Elementary 0524
Finance 0277
Guidance and Counseling 0519
Health 0680
Higher 0745
History of 0520
Home Economics 0278
Industrial 0521
Language and Literature 0279
Mathematics 0280
Music 0522
Philosophy of 0998
Physical 0523
Psychology 0525
Reading 0535
Religious 0527
Sciences 0714
Secondary 0533
Social Sciences 0534
Sociology of 0340
Special 0529
Teacher Training 0530
Technology 0710
Tests and Measurements 0288
Vocational 0747

LANGUAGE, LITERATURE AND LINGUISTICS
Language
- General 0679
- Ancient 0289
- Linguistics 0290
- Modern 0291

Literature
- General 0401
- Classical 0294
- Comparative 0295
- Medieval 0297
- Modern 0298
- African 0316
- American 0591
- Asian 0305
- Canadian (English) 0352
- Canadian (French) 0355
- English 0593
- Germanic 0311
- Latin American 0312
- Middle Eastern 0315
- Romance 0313
- Slavic and East European 0314

PHILOSOPHY, RELIGION AND THEOLOGY
Philosophy 0422
Religion
- General 0318
- Biblical Studies 0321
- Clergy 0319
- History of 0320
- Philosophy of 0322

Theology 0469

SOCIAL SCIENCES
American Studies 0323
Anthropology
- Archaeology 0324
- Cultural 0326
- Physical 0327

Business Administration
- General 0310
- Accounting 0272
- Banking 0770
- Management 0454
- Marketing 0338

Canadian Studies 0385
Economics
- General 0501
- Agricultural 0503
- Commerce-Business 0505
- Finance 0508
- History 0509
- Labor 0510
- Theory 0511

Folklore 0358
Geography 0366
Gerontology 0351
History
- General 0578
- Ancient 0579
- Medieval 0581
- Modern 0582
- Black 0328
- African 0331
- Asia, Australia and Oceania 0332
- Canadian 0334
- European 0335
- Latin American 0336
- Middle Eastern 0333
- United States 0337

History of Science 0585
Law 0398
Political Science
- General 0615
- International Law and Relations 0616
- Public Administration 0617

Recreation 0814
Social Work 0452
Sociology
- General 0626
- Criminology and Penology 0627
- Demography 0938
- Ethnic and Racial Studies 0631
- Individual and Family Studies 0628
- Industrial and Labor Relations 0629
- Public and Social Welfare 0630
- Social Structure and Development 0700
- Theory and Methods 0344

Transportation 0709
Urban and Regional Planning 0999
Women's Studies 0453

THE SCIENCES AND ENGINEERING

BIOLOGICAL SCIENCES
Agriculture
- General 0473
- Agronomy 0285
- Animal Culture and Nutrition 0475
- Animal Pathology 0476
- Food Science and Technology 0359
- Forestry and Wildlife 0478
- Plant Culture 0479
- Plant Pathology 0480
- Plant Physiology 0817
- Range Management 0777
- Wood Technology 0746

Biology
- General 0306
- Anatomy 0287
- Biostatistics 0308
- Botany 0309
- Cell 0379
- Ecology 0329
- Entomology 0353
- Genetics 0369
- Limnology 0793
- Microbiology 0410
- Molecular 0307
- Neuroscience 0317
- Oceanography 0416
- Physiology 0433
- Radiation 0821
- Veterinary Science 0778
- Zoology 0472

Biophysics
- General 0786
- Medical 0760

EARTH SCIENCES
Biogeochemistry 0425
Geochemistry 0996
Geodesy 0370
Geology 0372
Geophysics 0373
Hydrology 0388
Mineralogy 0411
Paleobotany 0345
Paleoecology 0426
Paleontology 0418
Paleozoology 0985
Palynology 0427
Physical Geography 0368
Physical Oceanography 0415

HEALTH AND ENVIRONMENTAL SCIENCES
Environmental Sciences 0768
Health Sciences
- General 0566
- Audiology 0300
- Chemotherapy 0992
- Dentistry 0567
- Education 0350
- Hospital Management 0769
- Human Development 0758
- Immunology 0982
- Medicine and Surgery 0564
- Mental Health 0347
- Nursing 0569
- Nutrition 0570
- Obstetrics and Gynecology 0380
- Occupational Health and Therapy 0354
- Ophthalmology 0381
- Pathology 0571
- Pharmacology 0419
- Pharmacy 0572
- Physical Therapy 0382
- Public Health 0573
- Radiology 0574
- Recreation 0575
- Speech Pathology 0460
- Toxicology 0383

Home Economics 0386

PHYSICAL SCIENCES
Pure Sciences
Chemistry
- General 0485
- Agricultural 0749
- Analytical 0486
- Biochemistry 0487
- Inorganic 0488
- Nuclear 0738
- Organic 0490
- Pharmaceutical 0491
- Physical 0494
- Polymer 0495
- Radiation 0754

Mathematics 0405
Physics
- General 0605
- Acoustics 0986
- Astronomy and Astrophysics 0606
- Atmospheric Science 0608
- Atomic 0748
- Electronics and Electricity 0607
- Elementary Particles and High Energy 0798
- Fluid and Plasma 0759
- Molecular 0609
- Nuclear 0610
- Optics 0752
- Radiation 0756
- Solid State 0611

Statistics 0463

Applied Sciences
Applied Mechanics 0346
Computer Science 0984
Engineering
- General 0537
- Aerospace 0538
- Agricultural 0539
- Automotive 0540
- Biomedical 0541
- Chemical 0542
- Civil 0543
- Electronics and Electrical 0544
- Heat and Thermodynamics 0348
- Hydraulic 0545
- Industrial 0546
- Marine 0547
- Materials Science 0794
- Mechanical 0548
- Metallurgy 0743
- Mining 0551
- Nuclear 0552
- Packaging 0549
- Petroleum 0765
- Sanitary and Municipal 0554
- System Science 0790

Geotechnology 0428
Operations Research 0796
Plastics Technology 0795
Textile Technology 0994

PSYCHOLOGY
General 0621
Behavioral 0384
Clinical 0622
Developmental 0620
Experimental 0623
Industrial 0624
Personality 0625
Physiological 0989
Psychobiology 0349
Psychometrics 0632
Social 0451

THE UNIVERSITY OF MANITOBA

FACUTY OF GRADUATE STUDIES

COPYRIGHT PERMISSION

MODELLING AND COMPENSATION OF STICK-SLIP FRICTION FOR ROBOT ARM CONTROL

BY

PETER D. TATARYN

A Thesis/Practicum submitted to the Faculty of Graduate Studies of the University of Manitoba in partial fulfillment of the requirements for the degree of

MASTER OF SCIENCE

Abstract

Friction force is the resistance to motion due to the interaction of a body with its surroundings. The body and its surroundings in consideration are robotic joints and the resistance to motion is coulomb friction. Present-day robot control system designs have neglected the integration of an accurate friction model and are realizing unsatisfactory control during fine motions. In this thesis, two approaches to accurate modelling of coulomb friction and six approaches to compensation are presented.

The two friction models are the Karnopp and the Reset Integrator models. The first part of this study compares and evaluates these models to previous work through simulations. The Karnopp model has better computing times and closer resembles the classical stick-slip friction model than the Reset Integrator model. The Reset Integrator model on the other hand is simpler to implement for various applications than the Karnopp model.

The second part of this thesis reports the results of an experimental and simulation study, conducted on an industrial manipulator, to evaluate the performances of six selected friction compensation techniques. Experiments are performed and simulations are modelled on the base axis of a GCA/DK electric-driven robot which has been retrofitted as a research manipulator. The main element of the controller is a simple PD control. First, the addition of three modified integral actions namely, Reset Integral (RI), Rate Variable Integral (RVI) and Reset Offset Integral (ROI) to this control is examined. Next, the application of a slip friction feedforward compensator is evaluated. Finally, two robust nonlinear compensators namely, Discontinuous Nonlinear Proportional Feedback (DNPF) and Smooth Robust Nonlinear Feedback (SRNF) are evaluated. Presently, there is little or no experimental record of applying these techniques to an actual industrial manipulator. Overall, the RVI, ROI, Feedforward, and SRNF compensators demonstrate potential in creating more accurate and simpler compensators for friction, the SRNF compensator displaying the most potential.

Acknowledgements

Many thanks go out to all the people and organizations who supported me throughout my thesis. I would like to thank Dr. N. Sepehri and Dr. D. Strong for their distinguished guidance and support as my thesis co-advisors, Al Lohse for his superiority in technical support for all of my experimental needs, and Dr. J. Shewchuck for his support in the early parts of this program. I would also like to thank my family, peers, and friends for their endless understanding and motivation speeches. I would also like to thank the University of Manitoba Engineering Library and its services for their irreplaceable convenience and Computer Services for their software, software support, and hardware facilities where I spent copious amounts of time researching, writing projects, reports, papers, and finally writing this thesis.

Finally, I would like to acknowledge the support of the Natural Sciences and Engineering Research Council (NSERC) of Canada, the Institute of Robotics and Intelligent Systems (IRIS) and Precarn Associates Inc.

Table of Contents

List of Figures

List of Tables

List of Symbols

α	SRNF constant
β	Reset Integrator damping coefficient
γ	RVI gain
ε	positive constant
θ_a	actual angular displacement
$\dot{\theta}_a$	actual angular velocity
θ_b	DNPF threshold value
θ_d	desired angular displacement
$\dot{\theta}_d$	desired angular velocity
$\ddot{\theta}_d$	desired angular acceleration
θ_e	displacement error
$\dot{\theta}_e$	velocity error
θ_{ri}	RI compensator range
a	Reset Integrator static friction gradient
b	DC motor viscous coefficient
D_v	Karnopp static (stick) friction velocity range
F_d	dynamic (slip) friction force
F_f	resultant friction force
F_i	input force
F_s	maximum static (stick) friction force
I	DC motor current
J	link inertia
K	spring rate
K_a	current amplifier gain
K_d	derivative gain
K_i	integral gain
K_p	proportional gain

K_r	Reset Integrator static friction spring rate
K_t	DC motor torque constant
l	manipulator length
m	mass
n	gear ratio/number of degrees-of-freedom (dof)
p	Reset Integrator position variable
$\dot{p}$	Reset Integrator velocity variable
p_o	Reset Integrator static friction range
t	time
T_d	dynamic (slip) friction torque
T_f	resultant friction torque
T_i	input torque
T_{in}	input torque for link n
T_{roi}	ROI time delay
T_s	maximum static friction torque
$v(t)$	control voltage input signal
$v_c(t)$	compensator voltage signal
$v_{PD}(t)$	PD control signal
v_{ms}	SRNF maximum static friction voltage equivalent
v_{slip}	dynamic (slip) friction voltage equivalent
v_{stick}	maximum static (stick) friction voltage equivalent
V	relative velocity
$\dot{V}$	relative acceleration
V_o	input velocity
V_{roi}	ROI threshold velocity

Chapter 1 Introduction

1.1 Overview

Friction is the resistance to motion due to the interaction of a body with its surroundings. There are three types of friction: rolling, viscous, and stick-slip. Rolling friction is the resistance due to the action of the body "pealing" away from its interacting surroundings. Viscous friction is the resistance to motion proportional to the velocity of a body with its surroundings. Stick-slip friction, also referred to as dry friction or coulomb friction, is the resistance to sliding motion and is related to the normal force acting on a body. Stick-slip friction has two regions linked by an exponential transition [8,45]. One region is a static (stick) region in which there is no motion between the body and its surroundings. The other is a dynamic (slip) region when there is motion between the body and its surroundings. The classical example of coulomb friction is shown in Figure 1a. In the static region, the friction force is proportional to the force acting on the body adjacent to the direction of motion. In the dynamic region, the friction force is arbitrary and changes when there is a change in direction of motion. The maximum friction force in the static region is usually larger than the friction force in the dynamic region. Rolling and stick-slip friction are both nonlinear in nature except that stick-slip friction has a significantly higher proportion to normal force. Viscous and stick-slip friction can have the same magnitude, but viscous friction is continuous.

Stick-slip friction is one of the major contributing factors for problems associated with accurate control in manipulators. The science of tribology has been contributing to the reduction of stick-slip friction effects by designing new and improved actuators, linkages, and lubricants; however, dealing effectively with what remains is an ongoing challenge left to control engineers [20]. Up to 25% of the torque produced by gear-driven motors of robotic joints is dissipated in overcoming joint stick-slip friction [10]. A similar

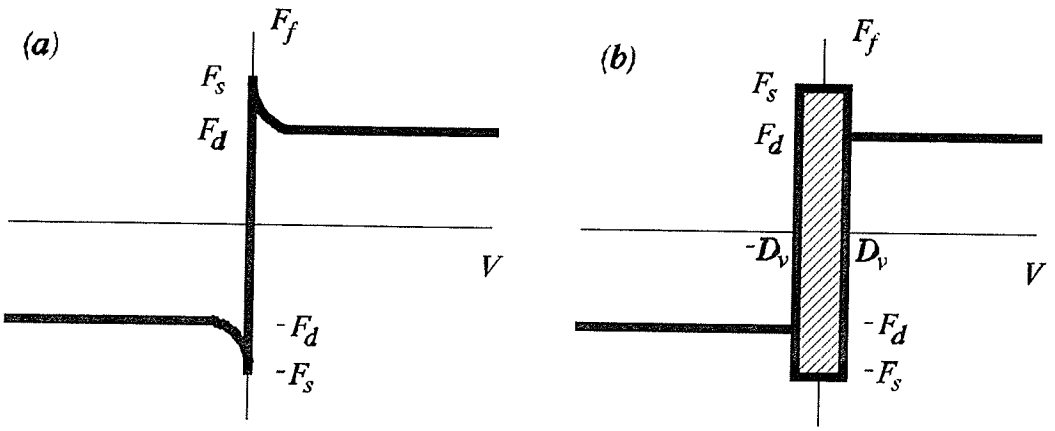

Figure 1 Stick-slip friction models: (a) Classical; (b) Karnopp.

observation was also made in [19] for the IBM 7545 robot with high reduction harmonic robot. Stick-slip friction compensation must therefore be considered in the design of robot controllers.

The initial step to dealing effectively with coulomb friction in manipulators is to derive an accurate model and implement it in simulations for given applications. The classical coulomb friction model was found computationally inaccurate in representing friction in the static region due to the fact that static friction occurred at zero velocity: computer simulations could rarely give a perfect zero velocity output. Karnopp [20] introduced a small region around zero velocity to eliminate this computation problem. For a velocity within this region, static friction is considered to be applied. Another model was derived with the idea of having many bristles "brush" along the surface acting as the friction force. This model took up a lot of computing time but was found to produce accurate results [20]. To reduce the amount of computing time at the cost of accuracy, this model was simplified by using only one single bristle along with a damping coefficient [20]. Other models were also derived which only included dynamic friction and excluded static friction. One such model was derived by Dahl [20]. Generally, the more complex the models were, the more accurate they became and the more time they took to compute.

The next step in dealing with friction is to implement control techniques that can eliminate its effects. Friction compensation is not as simple as implementing inverse friction models in the feedback loop [25]. There is in fact, many forms of friction compensators. Various techniques that have been developed to eliminate the effects range from straightforward, nonmodel-based strategies, i.e. strategies that do not require a complete knowledge of the dynamics of friction, to a more knowledge-based and dedicated approaches. A simple, nonmodel-based approach to reduce errors caused by friction is to apply a stiff PD control, i.e. a PD control with high proportional and velocity gains [9]. Instabilities may however occur due to a compliant drive train, existence of frictional memory, and the fact that in practical situations, it is impossible to obtain a true derivative from the measurements [1,6]. Integral actions are therefore utilized to eliminate friction-induced steady-state errors without the need of a high proportional gain [33,43]. Although integral control eliminates tracking errors, it may produce limit cycling about a set point for the class of coulomb friction [33]. The limit cycle is produced by the integral controller initially building up its signal until the manipulator breaks free from stick friction. The manipulator then experiences overshoot and comes to rest on the opposite side of the origin. This reaction continues again on the return motion.

Various other control techniques were subsequently developed to more accurately eliminate the effects of stick-slip friction. These techniques presently include adaptive control, bang-bang (impulsive) control, joint torque control, repetitive or learning control, nonlinear feedforward and feedback compensation, dithered control and table-lookup methods [7,11,34,41,44]. Adaptive control identifies friction online, but its compensation signal is of a linear nature and therefore inaccurate since it is compensating for a nonlinearity [6,9]; bang-bang control eliminates stick-slip error using sudden changes in torque which may add strain to the power train [6]; repetitive control requires cycling of at least one trajectory to achieve precise control [44]; and methods based on the friction forward cancellation techniques only work well when the friction model is exactly known or predictable. An excellent review on models, analysis and control tools for friction compensation can be found in [1,3,11].

1.2 Objective

The objective of this thesis is twofold. The first objective is, using simulations, to compare and evaluate two selected friction models with respect to previous works. The first model is the Karnopp friction model [22] and the second model is the Reset Integrator friction model [20]. These models were selected over others for their potential in being simple to utilize and their ability to produce accurate, yet computationally quick results. Also, there is record of evaluating these models for multiple-degree-of-freedom robotic manipulators. Both models will be evaluated in terms of simplicity, efficiency, and accuracy. Simplicity will be evaluated in terms of the number of parameters involved in describing the friction model and the mathematical flexibility of the model to different applications, that is, its ability to adjust. Efficiency will be evaluated in terms of computer processing time for the simulation. Accuracy will be evaluated with respect to how close the model resembles the classical friction model. Generally, the more accurate friction models are, the more complex the models become. Previous works have studied various friction models, some being complex and time-consuming [15,20]. It is critical and also difficult to develop an accurate, yet simple friction model. The significance of this work also lies in the fact that there is no record of the Karnopp and the Reset Integrator friction models being implemented in simulations of robotic manipulator dynamics. The Karnopp and Reset Integrator models provide a step towards simple and accurate solutions to modelling friction, specifically in robot joints. Viscous friction modelling will not be considered in this study.

The second objective is to present a performance qualification, in both experiments and simulations, of some techniques proposed towards accurate control of manipulators with joint stick-slip friction. This study is mainly concerned with methods that require a minimum knowledge of the friction model, and thus can be easily adopted in practical situations. The first three techniques are integral-based. The first integral method is a variation of traditional integral control with a reset action. The second integral method

namely, Rate-Variable Integral (RVI) [29] has been chosen for its effectiveness during initial start as well as its ability to control integral windup. The third integral action is called the Reset-Offset Integral (ROI) [35] and was recently proposed to remove the steady-state errors observed in positioning of hydraulic actuators with flow deadbands. The next controller uses feedforward to compensate for slip friction only. The last two control techniques fall into the category of feedback compensators. They are the Discontinuous Nonlinear Proportional Feedback (DNPF) control [39], and the Smooth Robust Nonlinear Feedback (SRNF) control [6]. All six techniques have been selected based on a number of reasons. First, they have been recently developed with good theoretical backing and have shown experimental potential. Second, in spite of their proven potential, there is little or no experimental record of applying them on actual robotic manipulators. Third, they appear to be easily added (plugged-in) to any PD-type controller without disturbing the controller structure. Finally, they seem to be less dependent on the friction identification whose characteristics are partially known.

The significance of this part of the work also lies in the fact that all the above selected compensation techniques are, for the first time, experimentally compared on an existing industrial robot, and under the same experimental environment. In particular, the use of an integral action is only discussed in most friction control literature as a motivation for more complicated strategies which, according to Armstrong-Hélouvry et al. in [1], "... is in direct contrast with its widespread use and with the variety of techniques developed to circumvent its shortcoming." These experiments permit us to compare the results obtained from the same manipulator and environment system, and draw conclusions about capacity of modified integral actions as opposed to more complicated algorithms in producing the desired effect in practical situations.

The simulations were run on a 50 MHz, 486DX personal computer based on a fourth-order Runge-Kutta variable step algorithm using double precision [32] and the experiments were performed on the base joint of an instrumented GCA/DK-2600 electrically actuated manipulator with a harmonic-drive transmission. Performing tests

on the gravity-independent, single degree-of-freedom (dof) link eliminates the effects of gravity and coupled dynamics.

All the experiments in this thesis are also performed in simulations to further study the influence caused by changing the physical parameters in the model or the controller and also, to confirm that the observations made from the experiments truly reflect the nature of the controllers and not some intrinsic properties (such as gear backlash) inherent to any real-world industrial system. The structure and physical parameters of the manipulator used in the simulation were chosen to resemble the GCA/DK-2600 robot.

Chapter 2 Modelling Coulomb Friction

2.1 Model Descriptions

2.1.1 Karnopp Model

When using the classical coulomb friction model (Figure 1a) for simulations, an exact value of zero for velocity can not be computed for the static region of coulomb friction and the model will end up not computing the friction force or torque in that region. Karnopp first defined a region $-D_v < V < D_v$, where D_v is a minute velocity. Outside this region, the friction force, F_f, is dynamic and is a sign function of the velocity, V, as shown in Figure 1b. Inside this region, V is considered zero and F_f is static determined by other forces in the system as long as V remains in the region until the maximum value of static friction force is reached. When the driving force exceeds the maximum static friction force, the body accelerates and shortly after, the magnitude of V will reach D_v and the model will switch from the static region to the dynamic region. Summarizing for a linear application,

$$F_f = \begin{cases} F_d\ sgn(V) & |V| > D_v \\ F_i & |V| \le D_v \text{ and } |F_i| \le F_s \\ F_s\ sgn(V) & |V| \le D_v \text{ and } |F_i| > F_s \end{cases} \quad (1)$$

where F_d is a constant value of dynamic or slipping friction, F_i is an input force parallel to the direction of motion, and F_s is the maximum static or sticking friction force. A block diagram of the Karnopp model for a single mass system is shown in Figure 2 [22].

When choosing the parameters for the Karnopp model, one has to know the maximum static friction, F_s, the speed at which dynamic friction is attained, D_v, and the dynamic friction, F_d. Choosing D_v depends on the compliance on the interacting surfaces. For

example, for metal interacting with metal, compliance is small, therefore D_v is small. For rubber interacting with rubber, compliance is large, therefore D_v is large.

Note that this model has not provided a "stand-alone" model of coulomb friction, but an approach for modelling dynamic systems that contains coulomb friction. In other words, a new friction model has to be developed for every different application. In some applications, the Karnopp model becomes difficult to integrate into a dynamic system leaving no choice but to focus attention on other methods of modelling friction.

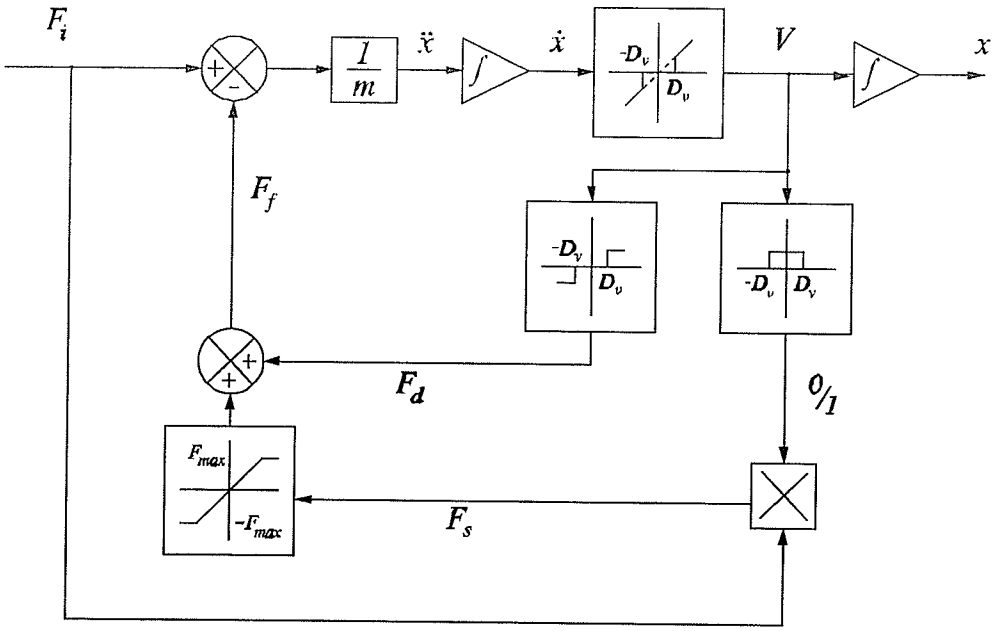

Figure 2 Karnopp stick-slip friction model block diagram.

2.1.2 Reset Integrator Model

The Reset Integrator model, unlike the Karnopp model, escapes the difficulty of deriving a new model for each different application and can be easily integrated into applications. The Reset Integrator uses an auxiliary integrator to represent the phenomenon of coulomb friction, hence the name of the model. A block diagram of the Reset Integrator friction

model is shown in Figure 3 [20]. The input to the Reset Integrator model is the velocity, V, between the body and its surroundings. This input is compared to the output of a nonlinear block that has the effect of turning off the input to the integrator with a given break-free deflection, p_o, according to the conditions below:

$$\begin{array}{ll} \dot{p}=0 & \begin{cases} V>0 \text{ and } p\geq p_o \\ \quad \text{or} \\ V<0 \text{ and } p\leq -p_o \end{cases} \\ \dot{p}=V & \text{otherwise} \end{array} \tag{2}$$

In the static region, the Reset Integrator becomes a spring-mass system with damping and represents friction force as a function of position via the position variable, p. Thus, for a given spring-mass with mass m, the friction force in the static region becomes

$$F_f=K_r(1+a)p+\beta\dot{p} \quad \text{for } |p|<p_o \tag{3}$$

where

$$\begin{aligned} a &= \frac{F_s-F_d}{F_d} && (a) \\ K_r &= \frac{F_d}{p_o} && (b) \\ \beta &= 0.707\sqrt{K_r(1+a)m} && (c) \end{aligned} \tag{4}$$

In the dynamic region, $\dot{p}$ becomes zero and when integrated, becomes a constant value, p. This value of p is then multiplied by K_r to get a value of dynamic friction force F_d, ie.,

$$F_d=K_r p \tag{5}$$

When choosing the parameters for the Reset Integrator model, one has to know the maximum static friction, F_s, the static damping coefficient, β, the break-free deflection, p_o, and the dynamic friction, F_d. Choosing p_o, just like choosing D_v, depends on the compliance of the interacting surfaces. The spring rate, K_r is set to a value so that when p is at an extreme, the friction force, $K_r p$, equals the dynamic friction value. The static

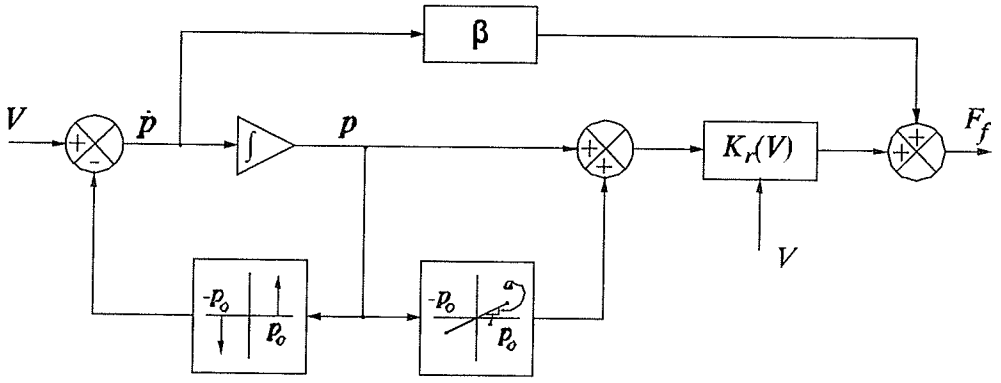

Figure 3 Reset Integrator stick-slip friction model block diagram.

friction gradient, a, adds the required additional friction when sticking such that the maximum static friction force is achieved. The damping term, $\beta\dot{p}$, is in the equation to include dissipation for oscillations that occur once the system has entered the static region. These oscillations quickly dissipate into the surrounding material as heat as the moving body comes to rest. If there is no information in regards to damping in the static region, the damping factor can be set using Equation (4c) above. Equation (4c) is derived from the dynamic equation of a spring-mass system with linear viscous damping at $1/2\sqrt{2}$ the value of critical damping. For example, deriving the critical damping of a single mass with Reset Integrator stick-slip friction is as follows:

$$m\ddot{x}+F_f=0 \tag{6}$$

Substituting for F_f using Equation (3),

$$m\ddot{x}+K_r(1+a)p+\beta\dot{p}=0 \tag{7}$$

Letting p = x and rearranging,

$$\ddot{x}+\frac{\beta}{m}\dot{x}+\frac{K_r}{m}(1+a)x=0 \tag{8}$$

The characteristic equation becomes

$$r^2+\frac{\beta}{m}r+\frac{K_r}{m}(1+a)=0 \tag{9}$$

Solving for r using the quadratic equation,

$$r=\frac{-\frac{\beta}{m}\pm\sqrt{\left(\frac{\beta}{m}\right)^2-4\frac{K_r}{m}(1+a)}}{2} \tag{10}$$

For critical damping,

$$\left(\frac{\beta}{m}\right)^2-4\frac{K_r}{m}(1+a)=0 \tag{11}$$

therefore,

$$\beta_{cr}=2\sqrt{K_r(1+a)m} \tag{12}$$

For unknown conditions, β_{cr} is multiplied by a factor of $1/2\sqrt{2}$ to become identical to Equation (4c). Note that β may add extra static friction forces exceeding the maximum given static friction, F_s.

This approach to computing friction does not require great changes for each application as is in the Karnopp model. As one can realise; however, there are more parameters to consider than the Karnopp model. Also, simulation time suffers since the calculation of p involves another state for each degree-of-freedom (dof).

2.2 Friction Simulations

2.2.1 Model Validation

The purpose of this section is firstly, to evaluate previous research on the Karnopp and Reset Integrator stick-slip friction models and secondly, to study the effect of stick-slip friction in manipulators on a theoretical level. Evaluating the two friction models involves reproducing previous simulations on stick-slip friction in linear motion found in [20]. Proceeding into original work then allows us to more closely study stick-slip friction in revolute manipulators. This includes introducing kick-back acceleration into the models.

A variable, time-step algorithm is used for the simulations. To determine the required step size with a certain degree of accuracy, the algorithm compares the results of each time step using a dimensionless value, *eps*. With this value of *eps*, the algorithm determines whether to increase or decrease the time step accordingly. The value of *eps* used in our simulations is 2.0×10^{-4}.

2.2.1.1 One-Degree-of-Freedom (dof) Spring-mass

The first example to be considered is a one-degree-of-freedom spring-mass system as shown in Figure 4. The dynamic equation for this system is as follows:

$$KV_o t = m\dot{V} + K\int V dt + F_f \tag{13}$$

where V_o is the input velocity to the system. The properties and conditions for this example are given in Table 1. These parameters for coulomb friction are reasonable considering the body weighs approximately one newton. Dynamic friction is assumed to be only a sign function of the block's velocity. The parameters selected for this model are given in Table 2.

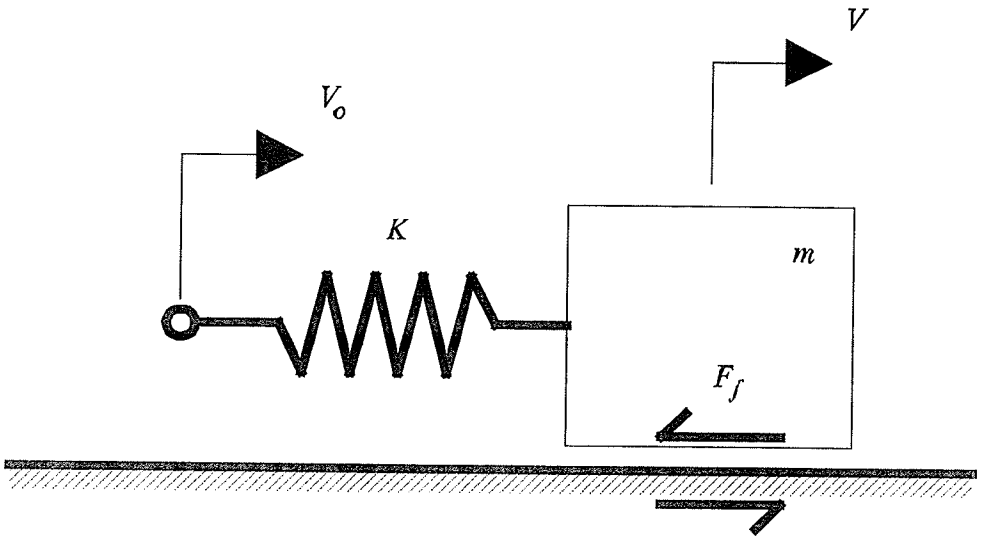

Figure 4 One-dof spring-mass.

Table 1 Properties and conditions for one-dof spring-mass.

Description	Value
m, block mass	0.1 kg
F_d, dynamic friction	0.20 N
F_s, maximum static friction	0.25 N
K, spring constant	100 N/m
V_o, input velocity	0.002 m/s
t, time	5.0 s

The selection of parameters for the Karnopp model only depends on choosing a value for D_v. For this case, D_v was set to a value of one percent of the step input velocity, V_o. Haessig and Friedland in [20] selected this value after trying several larger values and it was felt that the value of V_o was already sufficiently small. The static and dynamic friction values were set in accordance with the given values of F_s and F_d, respectively.

Table 2 Friction model parameters for one-dof spring-mass.

Model	Parameters	Value
Karnopp	D_v, static velocity range	2.0×10^{-5} m/s
	F_s, maximum static friction	0.25 N
	F_d, dynamic friction	0.20 N
Reset Integrator	p_o, static friction range	1.0×10^{-5} m
	K_r, spring rate	2.0×10^{-4} N/m
	β, damping coefficient	30 N/(m/s)
	a, static friction gradient	0.25

The Reset Integrator has parameters to calculate. The static friction range p_o, is selected with a minute displacement. Knowing the static and dynamic frictions, F_s and F_d, and using the selected value of the static friction range, p_o, the spring rate, K_r, the static friction gradient, a, and the damping coefficient, β, are calculated according to the given formulas in Section 2.1.2. Note that the formula for β is merely a guideline and should be used if no other information regarding damping in the static region is given.

The simulation time histories are given in Figure 5. Comparing plots, both models exhibit the same staircase behaviour of position versus time caused by periods of slipping separated by periods of sticking as shown in Figure 5a. The friction forces, however, differ in their static regions. The static friction forces of the Reset Integrator model in Figure 5c, unlike the Karnopp model in Figure 5b, peaks with quickly dissipating oscillations. This phenomenon is due to the nature of how the Reset Integrator functions in the static region of friction according to the given equation in Section 2.1.2 for static friction forces.

Both models' results coincide with that presented in [20] except that of the static friction forces for the Reset Integrator model. Unlike the plot given in [20], the static friction force peaks are at uniform values each time the block sticks. When single precision was

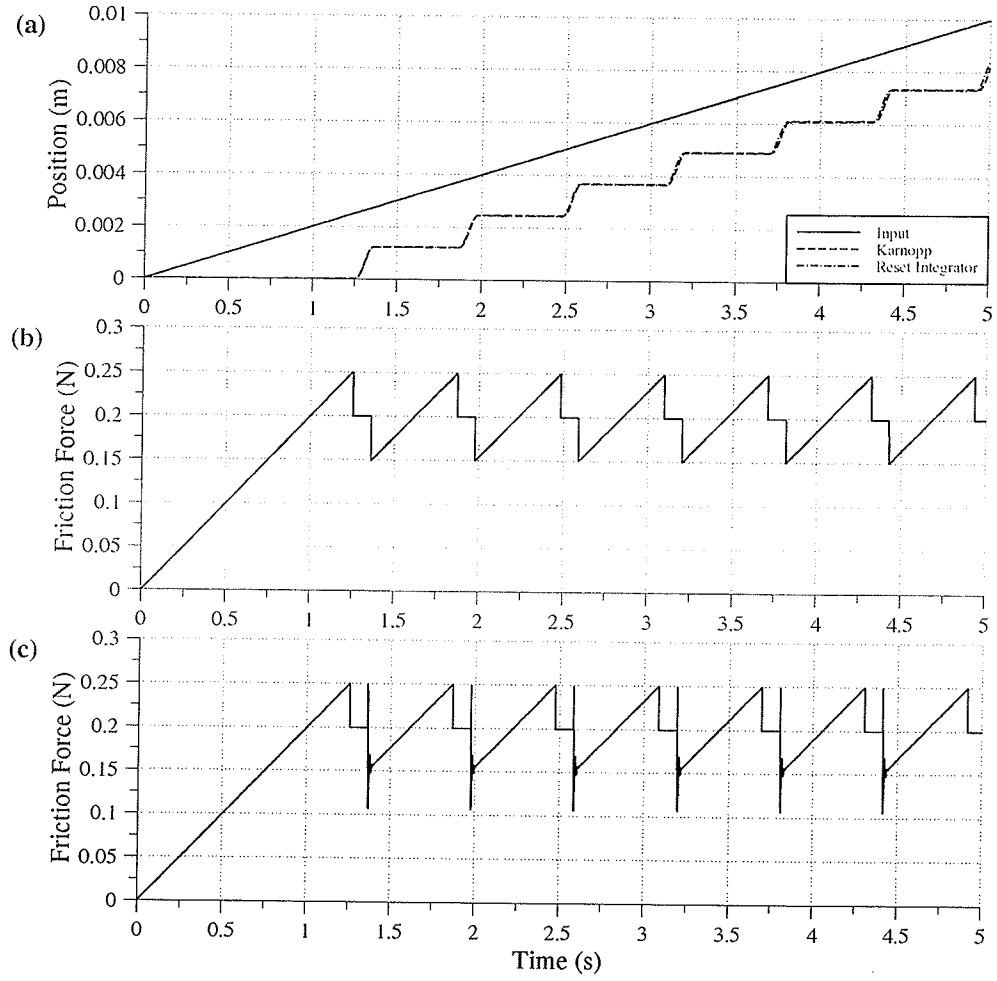

Figure 5 One-dof spring-mass results: (a) displacement; (b) Karnopp friction force; (c) Reset Integrator friction force.

used in this present program, the peaks were not uniform and the results coincided with those in [20]. When double precision was used however, accuracy was increased and the uniform peaks were attained. The authors probably did not have the required accuracy to attain these uniform peaks because only single precision was used in their simulations.

The peaks and oscillations in the Reset Integrator model are unlike the static friction forces as in the Karnopp model. It is believed that the extra static friction is developing from the damping coefficient, β. In previous trial simulations, reducing β reduced these

peaks, but at the same time, reduced oscillation dissipation due to less damping. On the other hand, increasing β increased these peaks. These peaks and oscillations are the nature of the Reset Integrator model and cannot be avoided.

Computing times for each model is given in Table 3. Note that the time period, t, of this simulation is 5.0 s. The Reset Integrator model was approximately twice as slow for two possible reasons. Firstly, the Reset Integrator model required numerical integration of a third state, p, and secondly, the variable step integrator required more steps for "tip-toeing" through the areas of static friction where the oscillations occurred.

Table 3 Computing times for one-dof spring-mass.

Model	Computation Time (s)
Karnopp	0.44
Reset Integrator	0.99

2.2.1.2 Two-dof Spring-mass

The second example to be considered is a two-degree-of-freedom spring-mass system as shown in Figure 6. The dynamic equation for this system is as follows:

$$\begin{pmatrix} K_1 V_o t \\ 0 \end{pmatrix} = \begin{bmatrix} m_1 & 0 \\ 0 & m_2 \end{bmatrix} \begin{pmatrix} \dot{V}_1 \\ \dot{V}_2 \end{pmatrix} + \begin{bmatrix} (K_1+K_2) & -K_2 \\ -K_2 & K_2 \end{bmatrix} \begin{pmatrix} \int V_1 dt \\ \int V_2 dt \end{pmatrix} + \begin{pmatrix} F_{f1} \\ -F_{f1}+F_{f2} \end{pmatrix} \qquad (14)$$

where V_o is the step input to the system. The properties and conditions for this example are given in Table 4 and the friction model parameters are listed in Table 5. The letter, n, represents the block number, for example, m_n for n=1,2 are the masses of block 1 and block 2, respectively.

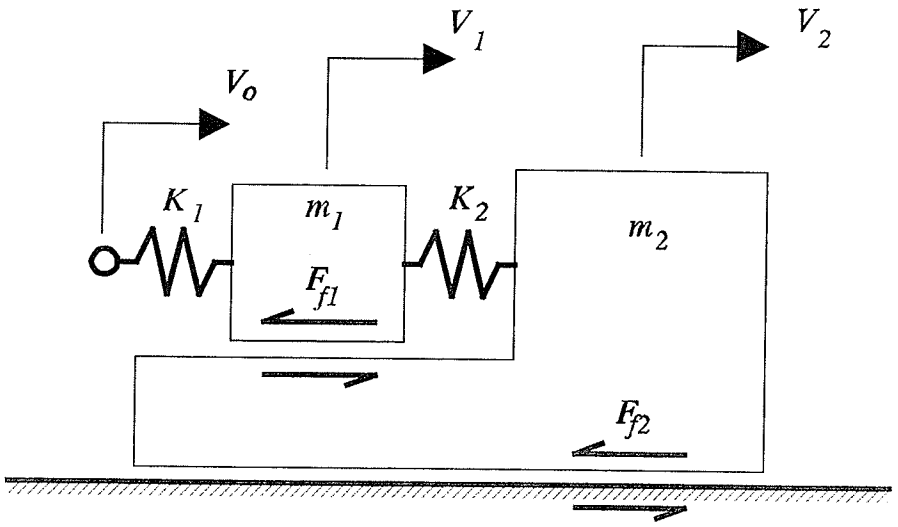

Figure 6 Two-dof spring-mass.

Table 4 Properties and conditions for two-dof spring-mass.

Description	Block 1	Block 2
m_n, mass	0.1 kg	0.1 kg
F_{dn}, dynamic friction	0.10 N	0.20 N
F_{sn}, maximum static friction	0.15 N	0.30 N
K_n, spring constant	100 N/m	200 N/m
V_o, input velocity	0.2 m/s $t<0.25$ s 0.0 m/s $t\geq 0.25$ s	
t, time	0.5 s	

Note that the Karnopp model changes for the two-degree-of-freedom example. Instead of having only two cases, ie. sticking and slipping, in the two body example, there are now four cases: (1) both bodies are sticking, (2) the first body is sticking and the second body is slipping, (3) both bodies are slipping, and (4) the first body is slipping and the second body is sticking. These four cases are now what makes up the Karnopp model for the two-degree-of-freedom spring-mass in Figure 6. Reconfiguring for different applications is one of the Karnopp model's drawbacks.

Table 5 Friction model parameters for two-dof spring-mass.

Model	Parameter	Block 1	Block 2
Karnopp	D_{vn}, static velocity range	$1.0\text{x}10^{-4}$ m/s	$1.0\text{x}10^{-4}$ m/s
	F_{sn}, maximum static friction	0.15 N	0.30 N
	F_{dn}, dynamic friction	0.10 N	0.20 N
Reset Integrator	p_{on}, static friction range	$1.0\text{x}10^{-5}$ m	$1.0\text{x}10^{-5}$ m
	K_{rn}, spring rate	$1.0\text{x}10^{4}$ N/m	$2.0\text{x}10^{4}$ N/m
	β_n, damping coefficient	40 N/(m/s)	40 N/(m/s)
	a_n, static friction gradient	0.5	0.5

The simulation results for this example are shown in Figure 7. The Karnopp model results matches the results in [20]. The stick friction values for the Reset Integrator are once again higher than the given values of stick friction as shown in Figure 7b. Computing times for both models is given in Table 6. Note that the time period, t, of this simulation is 0.5 s. Computing times for the Karnopp model is identical to its one-degree-of-freedom simulation but slower than the Reset Integrator model.

One would expect the Reset Integrator model to be slower because it has an extra state to calculate but unlike the one-degree-of-freedom example, there are less oscillations in the static friction region to slow down the computation time. Since there are less oscillations, the variable step integrator code requires less steps to "tip-toe" through the static region. Computation time in our case therefore, does not only depend on the number of states required to compute, but also the number of steps required in the variable step algorithm.

Table 6 Computing times for two-dof spring-mass.

Model	Computation Time (s)
Karnopp	0.44
Reset Integrator	0.38

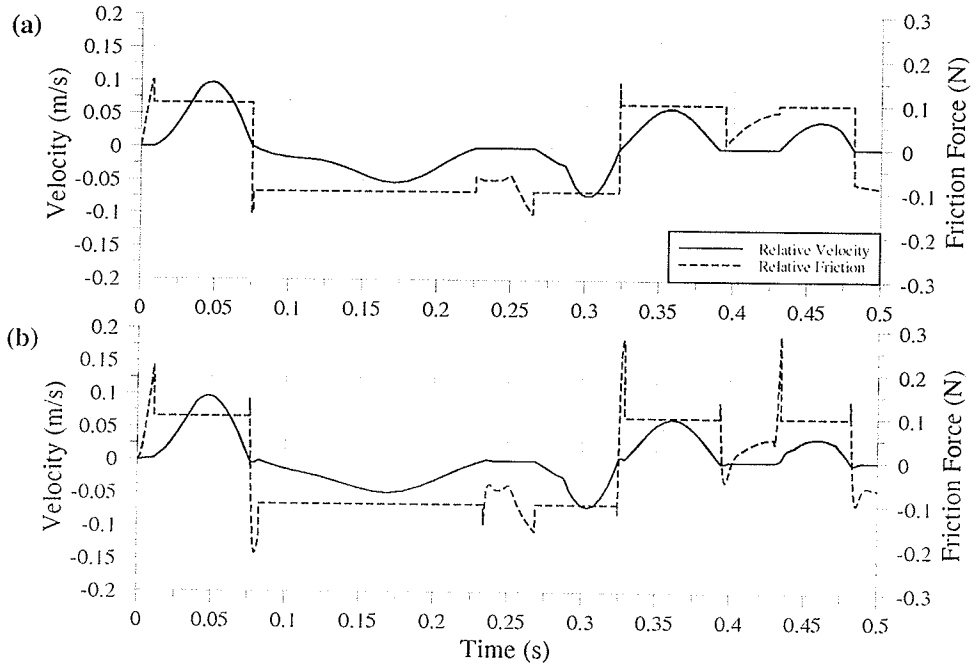

Figure 7 Two-dof spring-mass results: (a) Karnopp; (b) Reset Integrator.

2.2.2 Manipulator Analysis

There are presently two methods of deriving the dynamics of a multiple degree-of-freedom manipulator: the Lagrangian method and the Newton-Euler method. The Lagrangian method of forward dynamics calculates only the moment reactions at each joint and the Newton-Euler method of forward dynamics calculates the moment reactions as well as the reaction forces at each joint. Friction in robot joints can result from the normal forces applied by the input torque from the actuator and the reaction forces at the joint of the arm. In this thesis, only the Lagrangian method will be implemented.

2.2.2.1 One-dof Manipulator

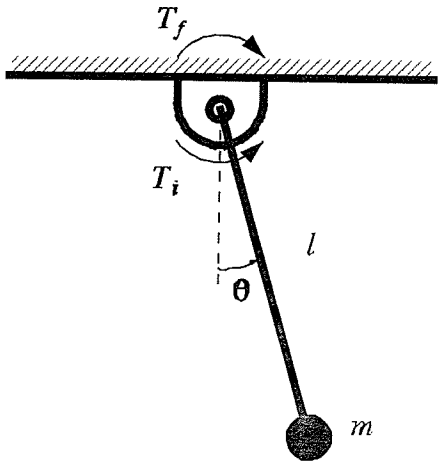

Figure 8 One-dof manipulator.

Consider the one-degree-of-freedom manipulator as shown in Figure 8. It is assumed that all the weight of the robot is concentrated at the ends of each link. The dynamic equation for this system is as follows:

$$T_i = ml^2\ddot{\theta} + T_f \tag{15}$$

The properties and conditions for this example are given in Table 7. Notice the values of the maximum static friction and dynamic friction are a little less than 25% of the input torque, the amount of torque dissipated to overcome friction in robot joints according to Craig in [10].

The friction parameters are given in Table 8. The static velocity range, D_v is given a value based on what is mentioned in Section 2.1.1. It is assumed that the interacting surfaces are steel gear teeth from harmonic drives having negligible compliance and therefore the value of D_v is small. All values of the Reset Integrator model are calculated using Equations (4a), (4b), and (4c) given the value of the static friction range, p_o. This static friction range is selected based on the selection methods in Section 2.1.2 and

Table 7 Properties and conditions for one-dof manipulator.

Description	Link 1
m_1, pendulum mass	1.0 kg
l_1, pendulum length	1.0 m
F_{d1}, dynamic friction	1.2 Nm
F_{s1}, maximum static friction	0.96 Nm
T_1, Input torque	6.0 Nm
θ_1, initial joint angle	0 deg
t, time	5.0 s

Table 8 Friction model parameters for one-dof manipulator.

Model	Parameter	Link 1
Karnopp	D_{v1}, static velocity range	5.7×10^{-4} deg/s
	T_{s1}, maximum static friction	1.2 Nm
	T_{d1}, dynamic friction	0.96 Nm
Reset Integrator	p_{o1}, static friction range	5.7×10^{-4} deg
	K_{r1}, spring rate	1700 Nm/deg
	β_1, damping coefficient	4.3 Nm/(deg/s)
	a_1, static friction gradient	0.25

assuming the interacting surfaces are steel. The initial condition for the joint angle, θ, is zero or the manipulator hanging straight down.

The resultant plots are given in Figure 9 for the Karnopp and the Reset Integrator models. With regards to the Karnopp model, static friction being greater than the dynamic friction only occurred on the first two instances where the manipulator entered the static region. The Reset Integrator on the other hand, static friction was greater than the dynamic friction every time the manipulator entered the static region. This is a familiar trend of the Reset Integrator due to the model's viscous damping experienced during sticking to

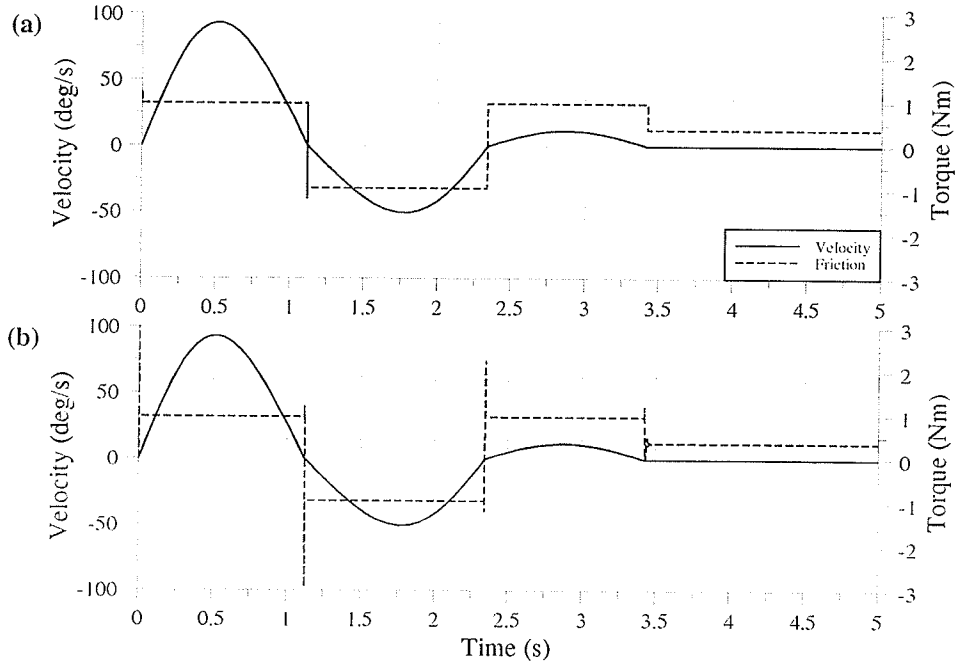

Figure 9 One-dof manipulator results: (a) Karnopp; (b) Reset Integrator.

dissipate oscillations. The angular velocities for both models however, turn out similar to each other.

The computation times for the one-degree-of-freedom manipulator are given in Table 9. Note that the time period, *t*, for this simulation is 5.0 s. The Karnopp model has a faster time than the Reset Integrator model. This is due to the same two reasons as mentioned in Section 2.2.1.1 and Section 2.2.1.2, more so the second reason of requiring more time steps during the static friction regions in the Reset Integrator model due to dissipating oscillations.

Table 9 Computing times for one-dof manipulator.

Model	Computation time (s)
Karnopp	0.16
Reset Integrator	0.44

2.2.2.2 Two-dof Manipulator

Consider now, the two-degree-of-freedom manipulator with friction in Figure 10. The dynamic equation for the two-degree-of-freedom manipulator is as follows:

$$\begin{pmatrix} T_1 \\ T_2 \end{pmatrix} = \begin{bmatrix} D_{11} & D_{12} \\ D_{21} & D_{22} \end{bmatrix} \begin{pmatrix} \ddot{\theta}_1 \\ \ddot{\theta}_2 \end{pmatrix} + \begin{bmatrix} D_{111} & D_{112} & D_{121} & D_{122} \\ D_{211} & D_{212} & D_{221} & D_{222} \end{bmatrix} \begin{pmatrix} \dot{\theta}_1\dot{\theta}_1 \\ \dot{\theta}_1\dot{\theta}_2 \\ \dot{\theta}_2\dot{\theta}_1 \\ \dot{\theta}_2\dot{\theta}_2 \end{pmatrix} + \begin{pmatrix} D_1 \\ D_2 \end{pmatrix} + \begin{pmatrix} T_{f1} \\ T_{f2} \end{pmatrix} \tag{16}$$

where

$$\begin{aligned}
&D_{11}=(m_1+m_2)l_1^2+m_2l_2^2+2m_2l_1l_2\cos(\theta_2)\\
&D_{12}=m_2l_2^2+m_2l_1l_2\cos(\theta_2)\\
&D_{21}=D_{12}\\
&D_{22}=m_2l_2^2\\
&\\
&D_{111}=0\\
&D_{112}=D_{121}=D_{122}=-m_2l_1l_2\sin(\theta_2)\\
&D_{211}=m_2l_1l_2\sin(\theta_2)\\
&D_{212}=D_{221}=D_{222}=0\\
&\\
&D_1=(m_1+m_2)gl_1\sin(\theta_1)+m_2gl_2\sin(\theta_1+\theta_2)\\
&D_2=m_2gl_2\sin(\theta_1+\theta_2)
\end{aligned} \tag{17}$$

Aid in deriving the dynamics of a two-degree-of-freedom manipulator using the Lagrangian method is given in [10]. The properties and conditions for both links of this model were based on the previous example. Two step input torques are applied at each joint. These properties and conditions are given in Table 10 and the friction parameters for the two friction models are given in Table 11.

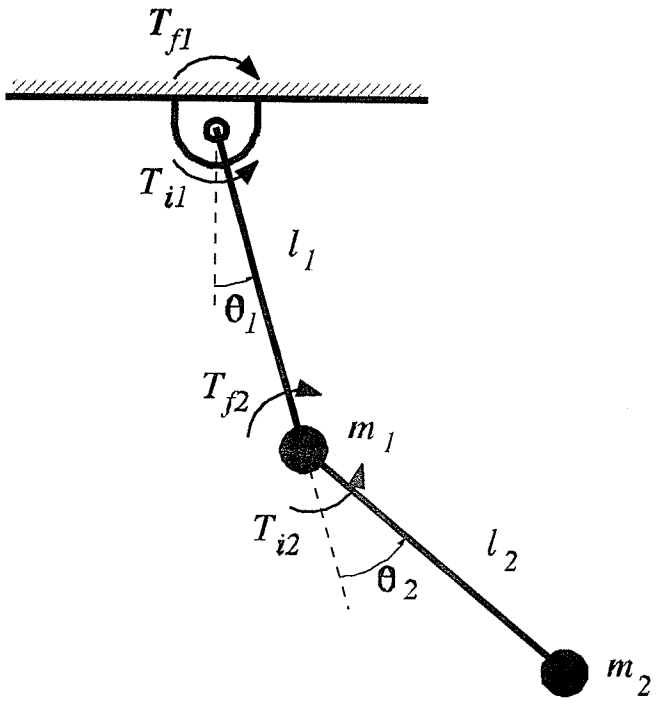

Figure 10 Two-dof manipulator.

Table 10 Properties and conditions for two-dof manipulator.

Description	Link 1	Link 2
m_n, pendulum mass	1.0 kg	1.0 kg
l_n, pendulum length	1.0 m	1.0 m
F_{dn}, dynamic friction	0.08 Nm	0.06 Nm
F_{sn}, maximum static friction	0.10 Nm	0.075 Nm
T_n, input torque	0.4 Nm	0.3 Nm
θ_n, initial joint angle	0 deg	0 deg
t, time	5.0 s	

Table 11 Friction parameters for two-dof manipulator.

Model	Parameter	Link 1	Link 2
Karnopp	D_{vn}, static velocity range	5.7×10^{-4} deg/s	5.7×10^{-4} deg/s
	T_{sn}, maximum static friction	0.10 Nm	0.075 Nm
	T_{dn}, dynamic friction	0.08 Nm	0.06 Nm
Reset Integrator	p_{on}, static friction range	5.7×10^{-5} deg	5.7×10^{-5} deg
	K_{rn}, spring rate	1400 Nm/deg	1000 Nm/deg
	β_n, damping coefficient	3.8 Nm/(deg/s)	3.3 Nm/(deg/s)
	a_n, static friction gradient	0.25	0.25

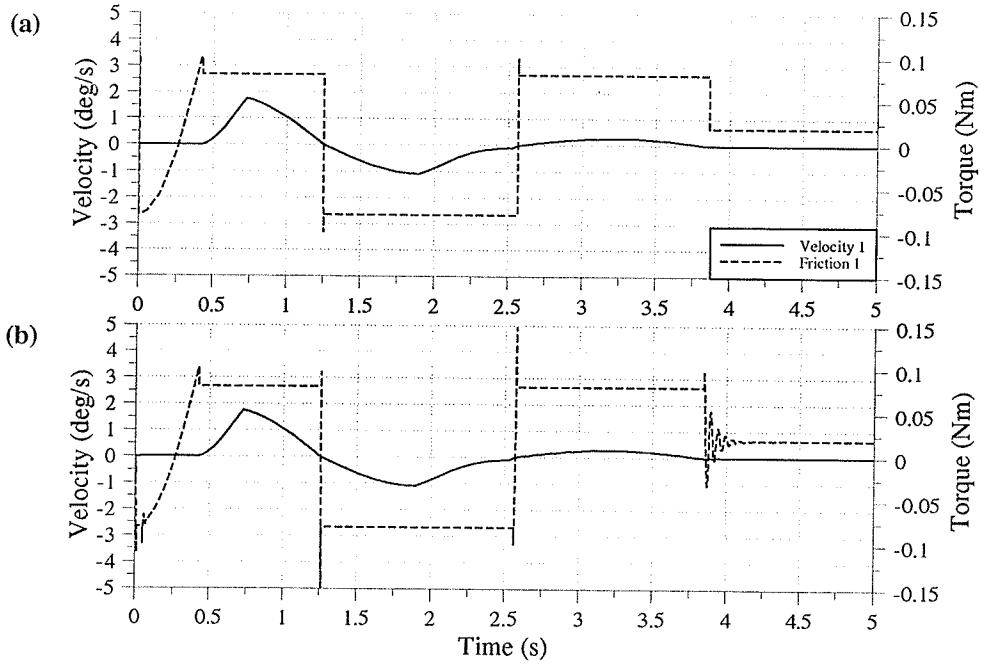

Figure 11 Two-dof manipulator link 1 results: (a) Karnopp; (b) Reset Integrator.

The results given in Figure 11 and Figure 12 show similar results for velocities, however as before, the stick friction forces computed by the Karnopp and the Reset Integrator models are different. The Reset Integrator model once again has peaks in the static region, losing accurate representation of given static friction values. The computational times for the two-degree-of-freedom manipulator are given in Table 12. Note that the time period, t, for this simulation is 5.0 s.

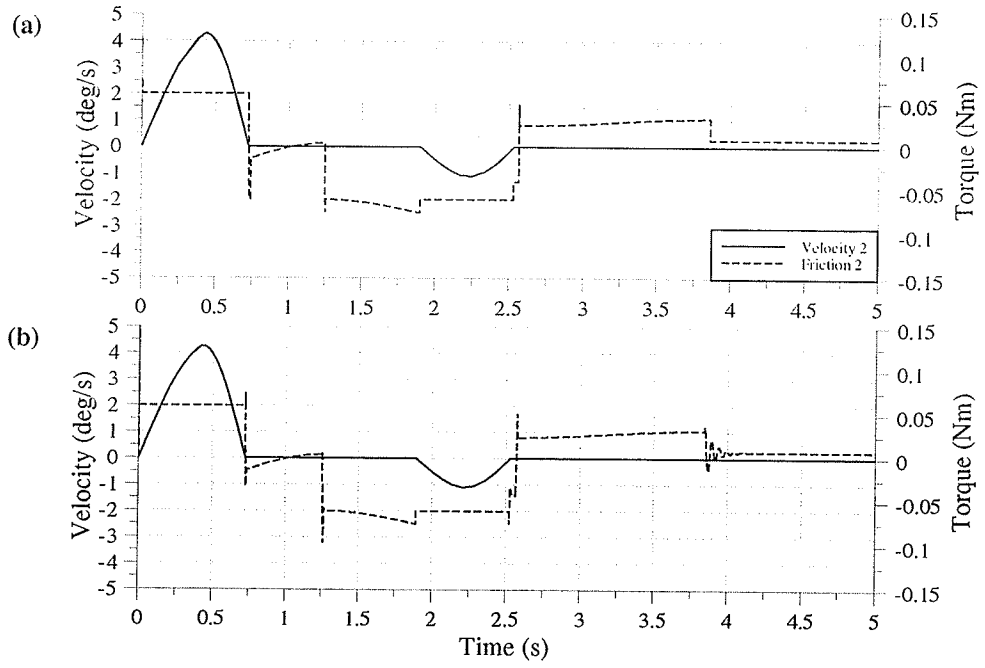

Figure 12 Two-dof manipulator link 2 results: (a) Karnopp; (b) Reset Integrator.

Table 12 Computing times for two-dof manipulator.

Model	Computation time (s)
Karnopp	1.10
Reset Integrator	3.46

A special assumption has to be made for this example with regards to the Karnopp model. Just as in the two-degree-of-freedom spring-mass, the two-degree-of-freedom manipulator has four cases. The case in which both joints are in the dynamic region is simple to derive but the three other cases where at least one joint is in the static region becomes complicated. The reason for this difficulty is that there are kick-back accelerations coupling on the links producing a torque which is directly affecting the static friction force modelling. To include these into the simulation, one must overhaul the algorithm to include some type of iteration or utilize the acceleration from the previous time step. For these results, the coupled accelerations are assumed negligible. The Karnopp model two-degree-of-freedom simulation can be broken up into four cases, namely:

Case (1) $\dot{\theta}_1 \approx 0, \dot{\theta}_2 \approx 0$

Case (2) $\dot{\theta}_1 \neq 0, \dot{\theta}_2 \approx 0$

Case (3) $\dot{\theta}_1 \approx 0, \dot{\theta}_2 \neq 0$

Case (4) $\dot{\theta}_1 \neq 0, \dot{\theta}_2 \neq 0.$

Solving the friction components using Equation (16) for Case (1):

$$T_{f1} = \begin{cases} T_1 - D_1 & |T_{f1}| \leq T_{s1} \\ T_{s1} sgn(T_{f1}) & |T_{f1}| > T_{s1} \end{cases}$$
$$T_{f2} = \begin{cases} T_2 - D_2 & |T_{f2}| \leq T_{s2} \\ T_{s2} sgn(T_{f2}) & |T_{f2}| > T_{s2} \end{cases} \qquad (18)$$

For Case (2):

$$T_{f1} = T_{d1} sgn(\dot{\theta}_1)$$
$$T_{f2} = \begin{cases} T_2 - (D_{211}\dot{\theta}_1^2 + D_2) - \dfrac{D_{21}}{D_{11}}[T_1 - (D_{111}\dot{\theta}_1^2 + D_1) - T_{f1}] & |T_{f2}| \leq T_{s2} \\ T_{s2} sgn(T_{f2}) & |T_{f2}| > T_{s2} \end{cases} \qquad (19)$$

For Case (3):

$$T_{f1} = \begin{cases} T_1 - (D_{122}\dot{\theta}_2^2 + D_1) - \dfrac{D_{12}}{D_{22}}[T_2 - (D_{222}\dot{\theta}_2^2 + D_2) - T_{f2}] & |T_{f1}| \le T_{s1} \\ T_{s1}\,sgn(T_{f1}) & |T_{f1}| > T_{s1} \end{cases}$$
$$T_{f2} = T_{d2}\,sgn(\dot{\theta}_2) \tag{20}$$

For Case (4):

$$T_{f1} = T_{d1}\,sgn(\dot{\theta}_1)$$
$$T_{f2} = T_{d2}\,sgn(\dot{\theta}_2) \tag{21}$$

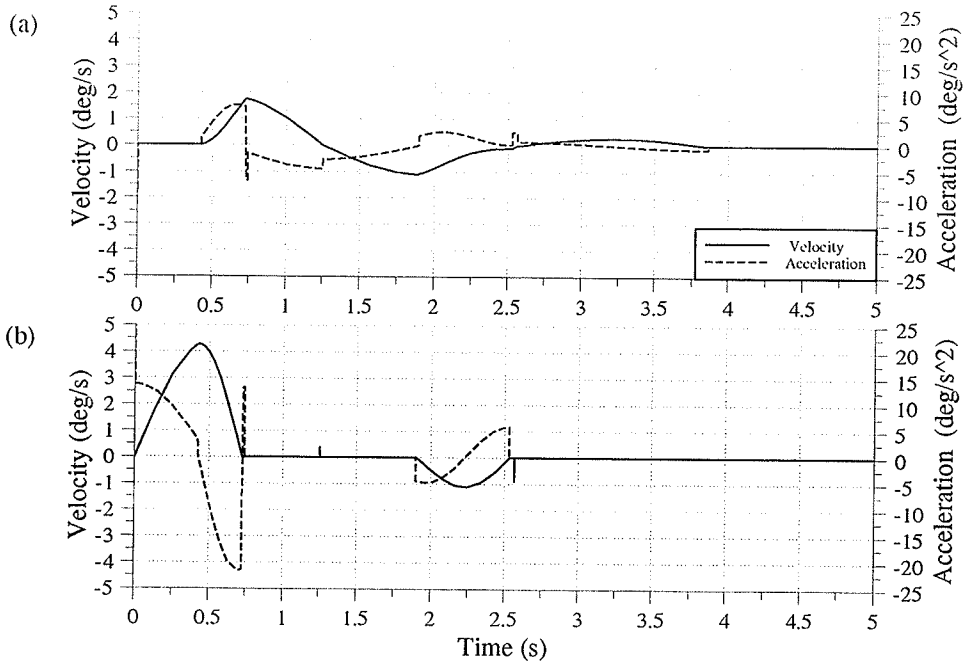

Figure 13 Two-dof manipulator velocities and accelerations, Karnopp model: (a) link 1; (b) link 2.

Neglecting these coupled accelerations in the Karnopp model is invalid. The accelerations at approximately t=1.25 seconds and t=2.5 seconds shown in Figure 13 are examples of magnitudes of accelerations when both joints are sticking (notice both joint velocities are zero at these instances). The Reset Integrator model is not directly affected by the

coupling accelerations since its static friction model is only a function of the joint velocities. An iteration loop added to rectify this problem would likely slow down computation time making the algorithm inefficient. Utilizing values of acceleration from the previous time step would be a quicker solution but not as accurate as having iterations. Utilizing the values from the previous time step will however be more accurate than having no acceleration component.

Let us now include the accelerations of the previous time step, $t_{(i-1)}$, into the Karnopp friction equations. From Equation (16), for Case (1):

$$T_{f1} = \begin{cases} T_1 - D_1 - [D_{11}\ddot{\theta}_{1(i-1)} + D_{12}\ddot{\theta}_{2(i-1)}] & |T_{f1}| \le T_{s1} \\ T_{s1} sgn(T_{f1}) & |T_{f1}| > T_{s1} \end{cases}$$
$$T_{f2} = \begin{cases} T_2 - D_2 - [D_{21}\ddot{\theta}_{1(i-1)} + D_{22}\ddot{\theta}_{2(i-1)}] & |T_{f2}| \le T_{s2} \\ T_{s2} sgn(T_{f2}) & |T_{f2}| > T_{s2} \end{cases} \quad (22)$$

For Case (2):

$$T_{f1} = T_{d1} sgn(\dot{\theta}_1)$$
$$T_{f2} = \begin{cases} T_2 - (D_{211}\dot{\theta}_1^2 + D_2) - (D_{21}\ddot{\theta}_{1(i-1)} + D_{22}\ddot{\theta}_{2(i-1)}) & |T_{f2}| \le T_{s2} \\ T_{s2} sgn(T_{f2}) & |T_{f2}| > T_{s2} \end{cases} \quad (23)$$

For Case (3):

$$T_{f1} = \begin{cases} T_1 - (D_{122}\dot{\theta}_2^2 + D_1) - (D_{11}\ddot{\theta}_{1(i-1)} + D_{12}\ddot{\theta}_{2(i-1)}) & |T_{f1}| \le T_{s1} \\ T_{s1} sgn(T_{f1}) & |T_{f1}| > T_{s1} \end{cases} \quad (24)$$
$$T_{f2} = T_{d2} sgn(\dot{\theta}_2)$$

For Case (4):

$$T_{f1} = T_{d1} sgn(\dot{\theta}_1)$$
$$T_{f2} = T_{d2} sgn(\dot{\theta}_2) \quad (25)$$

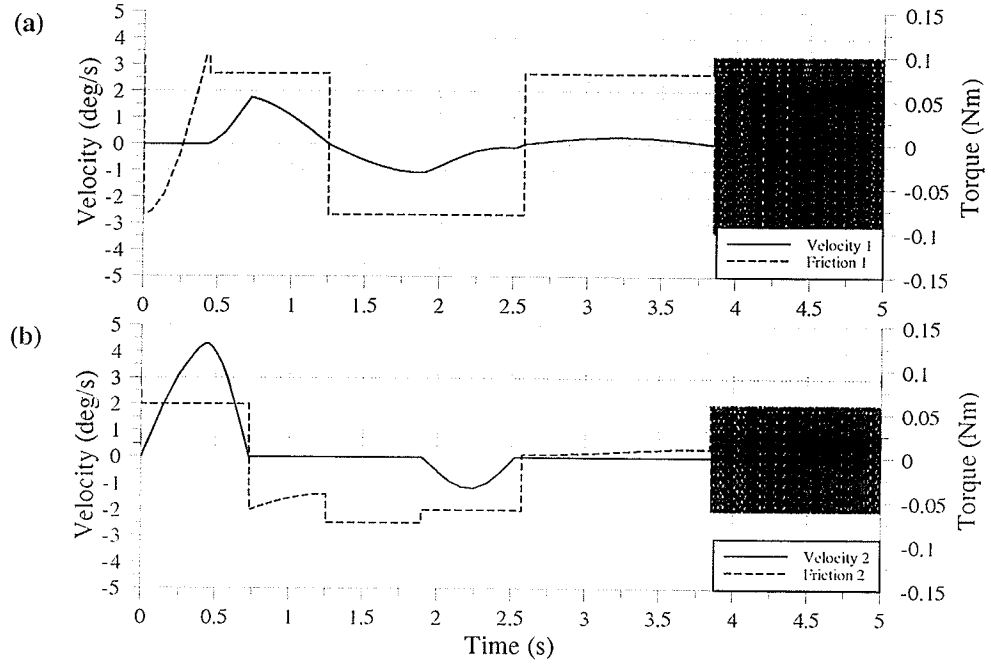

Figure 14 Two-dof manipulator results w/acceleration components: (a) link 1; (b) link 2.

With the addition of the acceleration components, the stick-slip friction results for both joints changes slightly as shown in Figure 14. The only parameter changed for this simulation was the value for D_v=5.7x10^{-3} *deg/s*. The computation time increases to 70 minutes on a NCD Workstation. The reason for this large increase in time is due to the sudden spikes of acceleration occurring close to zero velocity (as shown in Figure 13). The variable-step algorithm continuously iterates in this region to achieve a result within the accuracy of *eps*. Another observation is that maximum stick friction is achieved only in some parts of the simulation where the velocities are within the range of D_v. The simulation program does not save data from all of the times because of a limited data file size the plotting program, *RPlot*, could take. Also, when the joint velocities are both within the range of D_v, ie, Case (a), the stick frictions oscillate between the maximum values of stick friction. These oscillations are from the maximum values of stick friction switching back and forth from limit to limit, creating spikes in the accelerations.

2.3 Detailed Analysis of Friction Models

The previous section displayed the simulation performances of both friction models; however, it did not advance into great detail on the mechanics of either model. Grasping the concept behind the Karnopp model and especially the Reset Integrator model is difficult. The purpose of this section is therefore to gain a better understanding of both models through simulations. The chosen simulation is a block moving along a stick-slip frictional surface. Grasping the concept behind these two friction models is necessary to fully understand them for when they are implemented in simulations.

This analysis starts by first breaking down the models into simpler forms and then adds on components until the final products. The analysis of these simpler forms will not be covered in this thesis, only the analysis of the complete models will be covered. For both models however, each state will be analyzed with the aid of plots. That is, for the Karnopp model, the states would be the input force, acceleration, velocity, and friction force. For the Reset Integrator, the states would be the input force, acceleration, velocity, velocity variable, position variable, and friction force.

Three different types of input forces are applied to the block. First, a square wave input force is applied for studying transients, then a triangular wave input force for ramp effects, and finally, a spring with constant velocity input as done in Section 2.2.1.1. Analysing the friction models this way proves to be effective in displaying the mechanics of each model in motion as well as analysing exactly how and why these models perform.

2.3.1 Karnopp Model

2.3.1.1 Square Wave Input Force

Table 13 Parameters for square wave input force on a single mass, Karnopp model.

Description	Value
m, block mass	1.0 kg
F_d, dynamic friction	0.6 N
F_s, maximum static friction	0.8 N
F_i, input force	±1.0 N square wave
D_v, static velocity range	0.001 m/s
t, time	8.0 s

Consider the square wave input force induced on the block using the Karnopp model as shown in the plots in Figure 15. The parameters for this simulation are given in Table 13. It should be noted that in this analysis, slip friction is set at approximately 25% less than that of stick friction. First, the block is initially at rest. Suddenly, an input force of one Newton is applied to the block. Since the block is at zero velocity, the friction force is in the sticking region. The sticking force however is too small to match the input force and there is an imbalance of force causing the block to move. Once the block exceeds the value of the static velocity range, D_v, the friction force switches from stick to slip friction. Since the slip friction is less than the maximum stick friction, the acceleration jumps to a slightly larger value. After one second, the input force drops to zero and the velocity of the block starts to decrease. Once the block's velocity decreases to the value of D_v, the friction force switches from slip back to stick and since the input force is zero, so is the stick friction force. At two seconds, the input force becomes negative one Newton and the same stick-slip trend occurs except in the negative region. The same stick-slip trend follows for the remainder of the simulation.

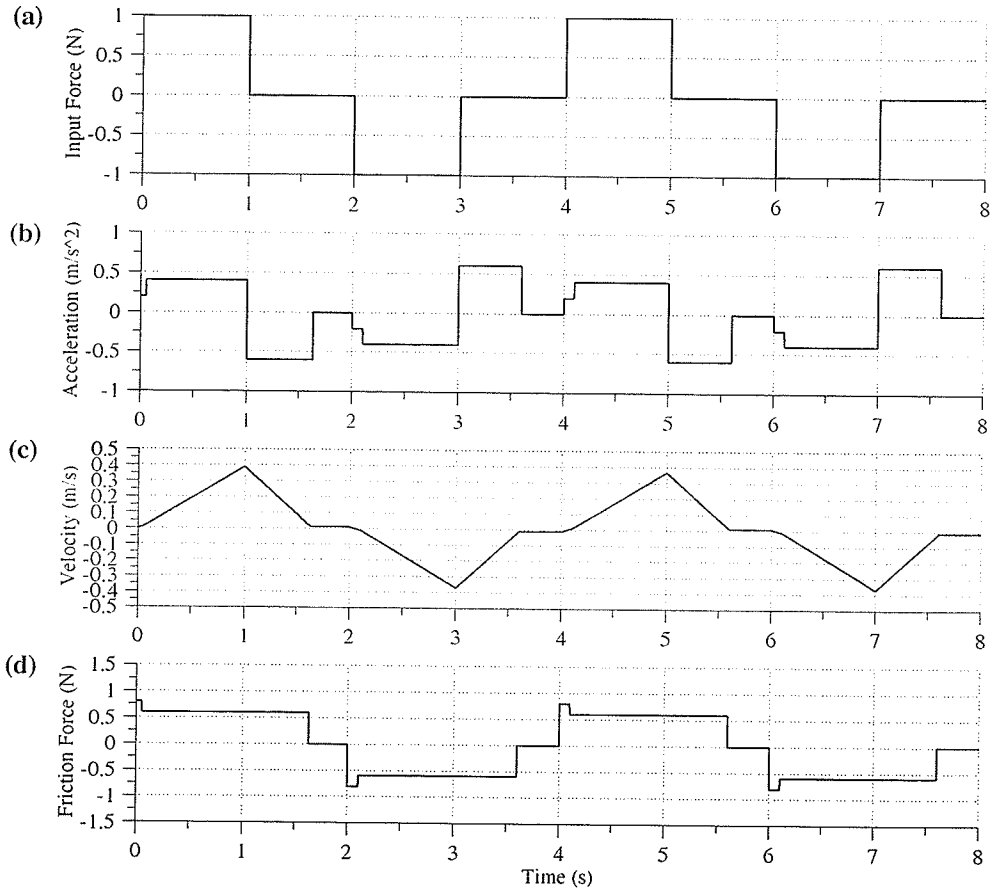

Figure 15 Square wave results, Karnopp model: (a) F_i; (b) $\dot{V}$; (c) V; (d) F_f.

A small value of the static velocity range, D_v, reduces the amount of time sticking and also reduces the value of the velocity of the block when it is at rest. Note that this is how the Karnopp model operates. Once the velocity reaches the static velocity range, either from the positive or the negative region, the slip friction switches to stick. In the plots, the velocity is close to zero when the velocity is near $\pm D_v$.

2.3.1.2 Triangular Wave Input Force

Table 14 Parameters for triangular wave input force on a single mass, Karnopp model.

Description	Value
m, block mass	1.0 kg
F_d, dynamic friction	0.6 N
F_s, maximum static friction	0.8 N
F_i, input force	±1.0 N triangle wave
D_v, static velocity range	0.001 m/s
t, time	8.0 s

Consider now, the triangular wave input force test with the resultant plots shown in Figure 16 with the parameters given in Table 14. Let us go through the plots starting at the initial conditions. The block is initially at rest, therefore, the friction force is in the stick region. The input force steadily increases, stick friction matches it resulting in cancelling out acceleration and keeps the block from moving. Once the input force reaches the maximum value of stick friction, the friction force cannot match the input force. An imbalance of force occurs resulting in an acceleration and the block starts to move. Once the velocity reaches D_v, the friction force switches from sticking friction to slipping friction. This value of friction is less than the maximum stick friction, therefore, acceleration jumps up. Soon after, the input force starts to decrease linearly. This decrease in force decreases the acceleration which in turn eventually slows down the block until it reaches the positive value of D_v. Once the velocity reaches this value, the friction force switches back from slip to stick and, since the input force is less than the maximum stick friction force the sticking force takes on the value of the input force. The value of velocity however, is still not zero. In fact, it has remained at D_v when the velocity of the block initially was slowing down and entering the stick region. The velocity of the block will remain at this limit until the input force exceeds the value of

maximum stick friction. This occurs just before the three second mark. Once the input force exceeds the value of maximum stick friction, acceleration decreases resulting in the velocity to be decreasing starting from $+D_v$ and then going into the negative velocity region. This trend repeats itself a few more times until the end of the simulation. Generally, for best results, D_v must be less than one percent of the maximum velocity of the object. For this case, D_v is 0.001 m/s, a good estimate since the maximum velocity is slightly larger than 0.1 m/s.

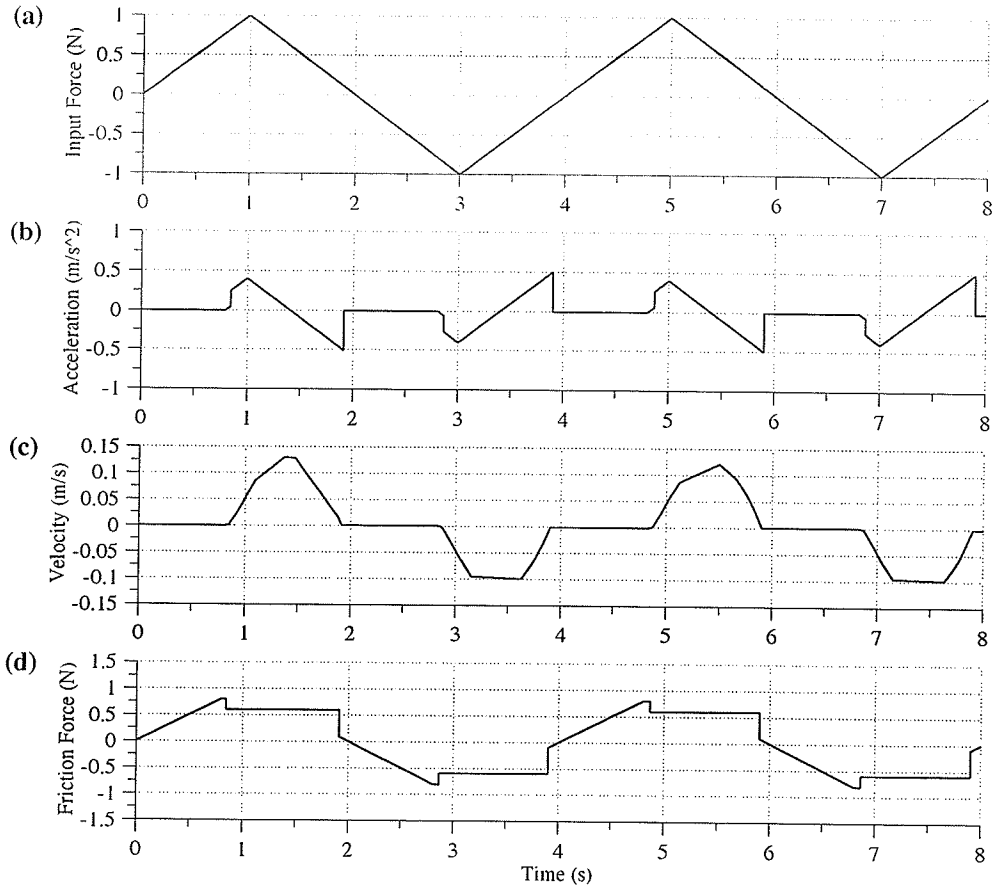

Figure 16 Triangular wave results, Karnopp model: (a) F_i; (b) $\dot{V}$; (c) V; (d) F_f.

2.3.1.3 One-dof Spring-mass Revisited

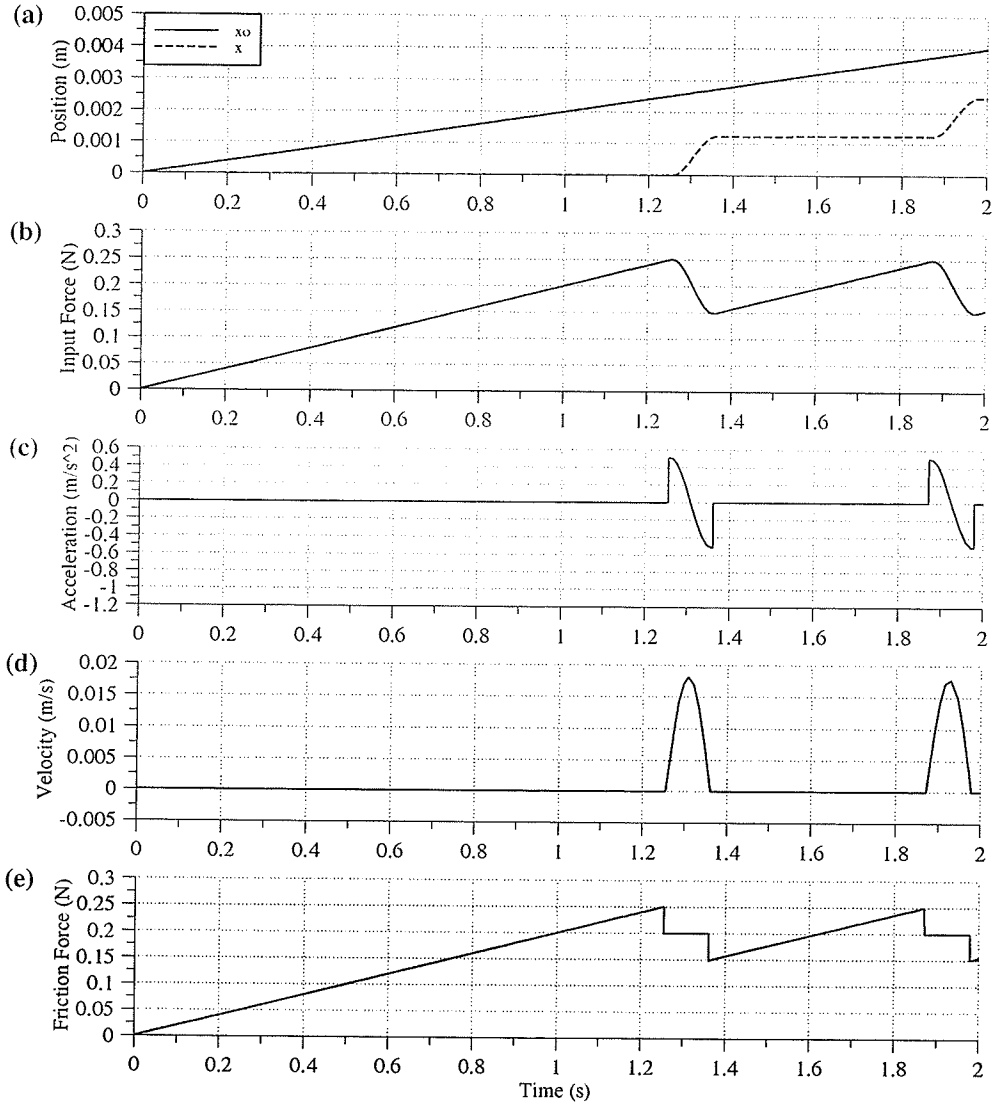

Figure 17 One-dof spring-mass results, Karnopp model: (a) displacements; (b) F_i; (c) $\dot{V}$; (d) V; (e) F_f.

Let us now proceed to the detailed analysis of the simulation in Section 2.2.1.1: input force induced by a spring attached to the mass with a constant velocity. The parameters used are the same as in Section 2.2.1.1 (Table 1 and Table 2) except that the simulation time is only 2.0 s. The simulation results are shown in Figure 17. The input force is the

difference between the displacement of the constant velocity and the displacement of the block multiplied by a spring constant as shown in the first two plots. Acceleration is the difference of the input force and the friction force as shown in Figure 17c, velocity is the integral of acceleration as shown in Figure 17d, and finally, the resulting friction force in Figure 17e.

2.3.2 Reset Integrator Model

2.3.2.1 Square Wave Input Force

Table 15 Parameters for square wave input force on a single mass, Reset Integrator model.

Description	Value
m, block mass	1.0 kg
F_d, dynamic friction	0.6 N
F_s, maximum static friction	0.8 N
F_i, input force	±1.0 N square wave
p_o, static friction range	0.0001 m/s
K_r, spring rate	6000 N/m
β, damping coefficient	55 N/(m/s)
a, static friction gradient	0.33
t, time	8.0 s

Consider the square wave input force. The results are shown in Figure 18 using the parameters in Table 15. Starting at initial conditions, when the block is at rest, a input force of one Newton is suddenly exerted to the block. Since the friction force for the Reset Integrator model comes from the combination of the velocity variable and the position variable for sticking and both are initially zero, the initial friction force is zero. These variables quickly respond to the input force, the position variable and the velocity

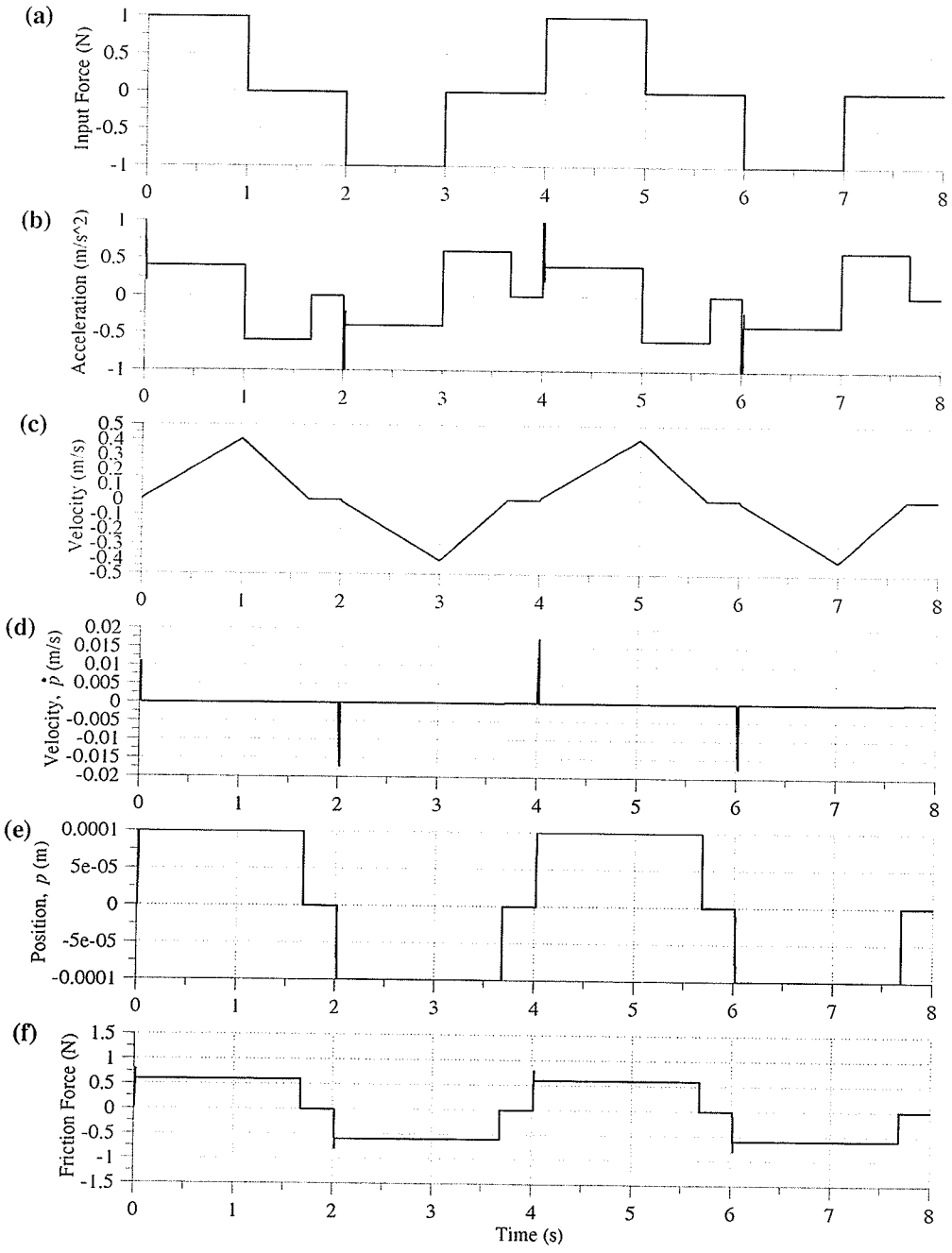

Figure 18 Square wave results, Reset Integrator model: (a) F_i; (b) $\dot{V}$; (c) V; (d) $\dot{p}$; (e) p; (f) F_f.

variable quickly increase to give a value of stick friction until the position limit, p_o is reached. The value of friction however, is greater than the given maximum friction value. The sudden change in input force caused the Reset Integrator model to add the position variable with a significant velocity variable produced due to the sudden change. The combination of these two variables caused the resultant stick friction to be greater than the given stick friction value. Recall that once the p reaches p_o, the friction force changes from stick to slip. The block is now moving in the slip region of friction. Just after one and a half seconds, the block slows down and goes into the stick region again. Once the velocity variable goes below zero velocity, the position variable starts to decrease. This is when stick friction in the Reset Integrator occurs. Since in this case, the position variable is in the positive region, and the friction force is going to decrease to zero, the friction force calculated by the Reset Integrator becomes positive for a slight moment and then drops to oscillate about the zero point of friction force, and finally settles. This damped oscillation is the nature of the Reset Integrator model because in the sticking region, it calculates friction using a second order system using the position variable and the velocity variable. Reiterating, the spike just after one and one half seconds is from the previous condition of the position variable and the damped oscillations are from the second order system of the velocity and position variable. The same trend appears in the other following stick regions in the simulation.

2.3.2.2 Triangular Wave Input Force

Consider now, the triangular input force simulation. Plots of the simulation are shown in Figure 19 using the parameters in Table 16. Compared to the square wave input force, the triangular wave input force displays the effect of how the Reset Integrator operates to calculate its stick-slip friction in steady state, that is, when there is little effect of the velocity variable in the stick region. Initially, the block is at rest with an input force linearly increasing and the friction force accurately following the input force to cancel it out. Once the input force reaches the maximum static friction, the position variable has reached p_o and the Reset Integrator switches into the slip mode and the position variable

Table 16 Parameters for triangular wave input force on a single mass, Reset Integrator model.

Description	Value
m, block mass	1.0 kg
F_d, dynamic friction	0.6 N
F_s, maximum static friction	0.8 N
F_i, input force	±1.0 N triangle wave
p_o, stick friction range	0.0001 m/s
K_r, spring rate	6000 N/m
β, damping coefficient	55 N/(m/s)
a, stick friction gradient	0.33
t, time	8.0 s

remains at the value, p_o for calculating slip friction. As the input force proceeds on its downward slope, the velocity of the block reaches a maximum velocity and starts its decent towards zero velocity. Once the block reaches zero velocity, the position variable starts to decrease indicating the start of the switch from slip back into stick mode. The transition from slip to stick for the Reset Integrator model is not as smooth as the transition from stick to slip. As shown here, the Reset Integrator's sticking region first starts at an unrealistic spike produced by the initial condition of the position variable previously used for calculating the slip friction. It then oscillates and settles on the final value of stick friction. After the stick friction settles, it once again matches the input force magnitude resulting in cancelling out acceleration and therefore producing a zero velocity of the block until it reaches p_o indicating to switch stick to slip friction once again as in the beginning. This time however, the position variable is opposite in sign. The same trend continues for the remainder of the simulation.

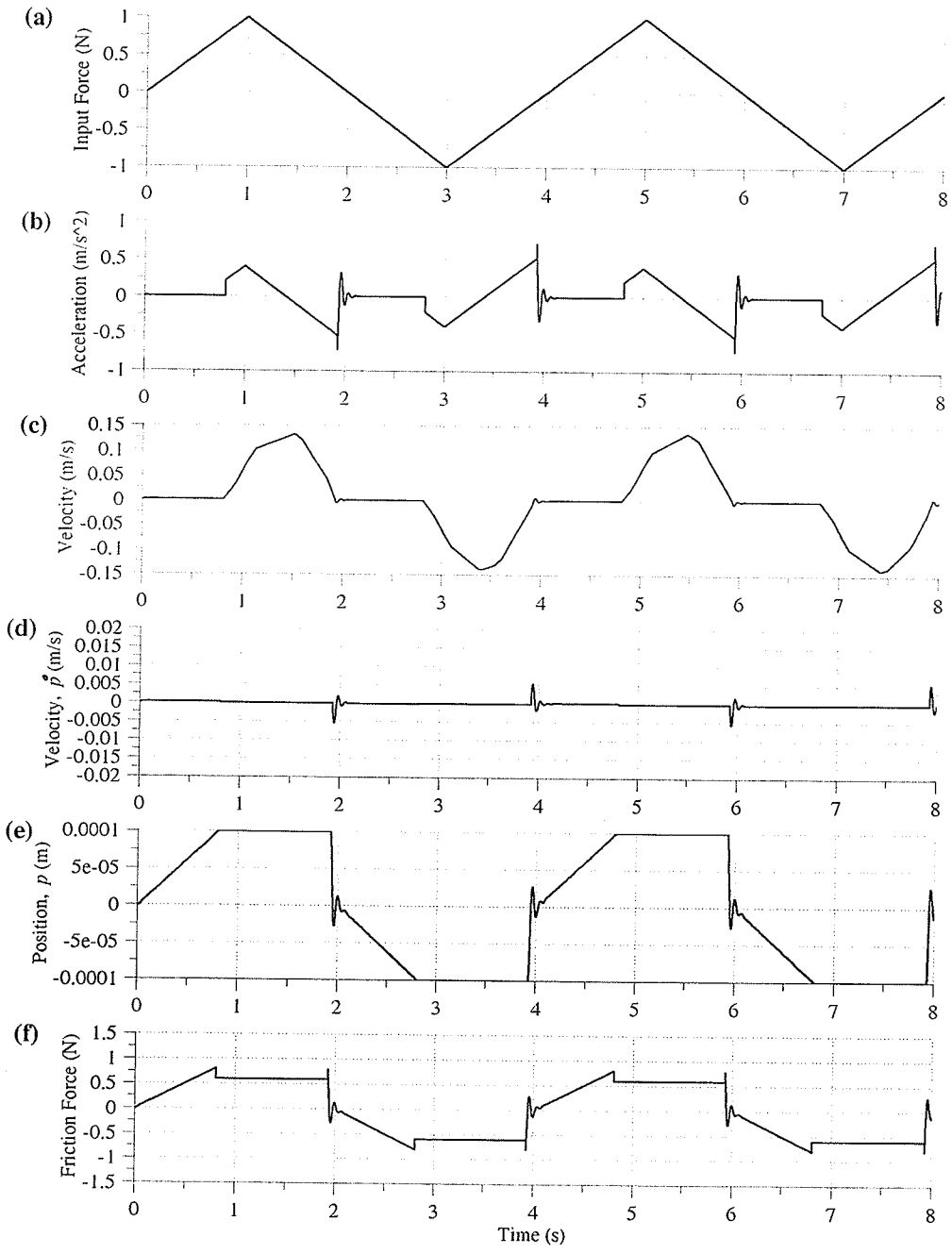

Figure 19 Triangular wave results, Reset Integrator model: (a) F_i; (b) $\dot{V}$; (c) V; (d) $\dot{p}$; (e) p; (f) F_i.

2.3.2.3 One-dof Spring-mass Revisited

Consider now the Reset Integrator model with input force induced by a constant velocity acting on a spring attached to the block. The simulation plots are shown in Figure 20 and the parameters used are the same as in Section 2.2.1.1 (Table 1 and Table 2) except that once again, the simulations times are 2.0 s. As mentioned in the Karnopp discussion of the spring-mass model, the input force is generated via the difference between the displacement of the block and the displacement produced by the constant velocity. Initially, this produces a linearly increasing force on the block which is equally opposed by a sticking friction force produced by the Reset Integrator model. Once the Reset Integrator position variable reaches p_o to indicate maximum stick friction, the model smoothly switches from stick to slip friction and the block begins to move. The velocity of the block increases due to the sudden input of acceleration produced by the spring, peaks, and then starts to decrease. Once it reaches zero velocity, the Reset Integrator kicks in the stick friction as rough as usual. The same trend then repeats itself over again starting with the block initially at rest and building up a stick friction resistance until it reaches the maximum value of the position variable, switching from stick to slip friction, the block moving, and so on.

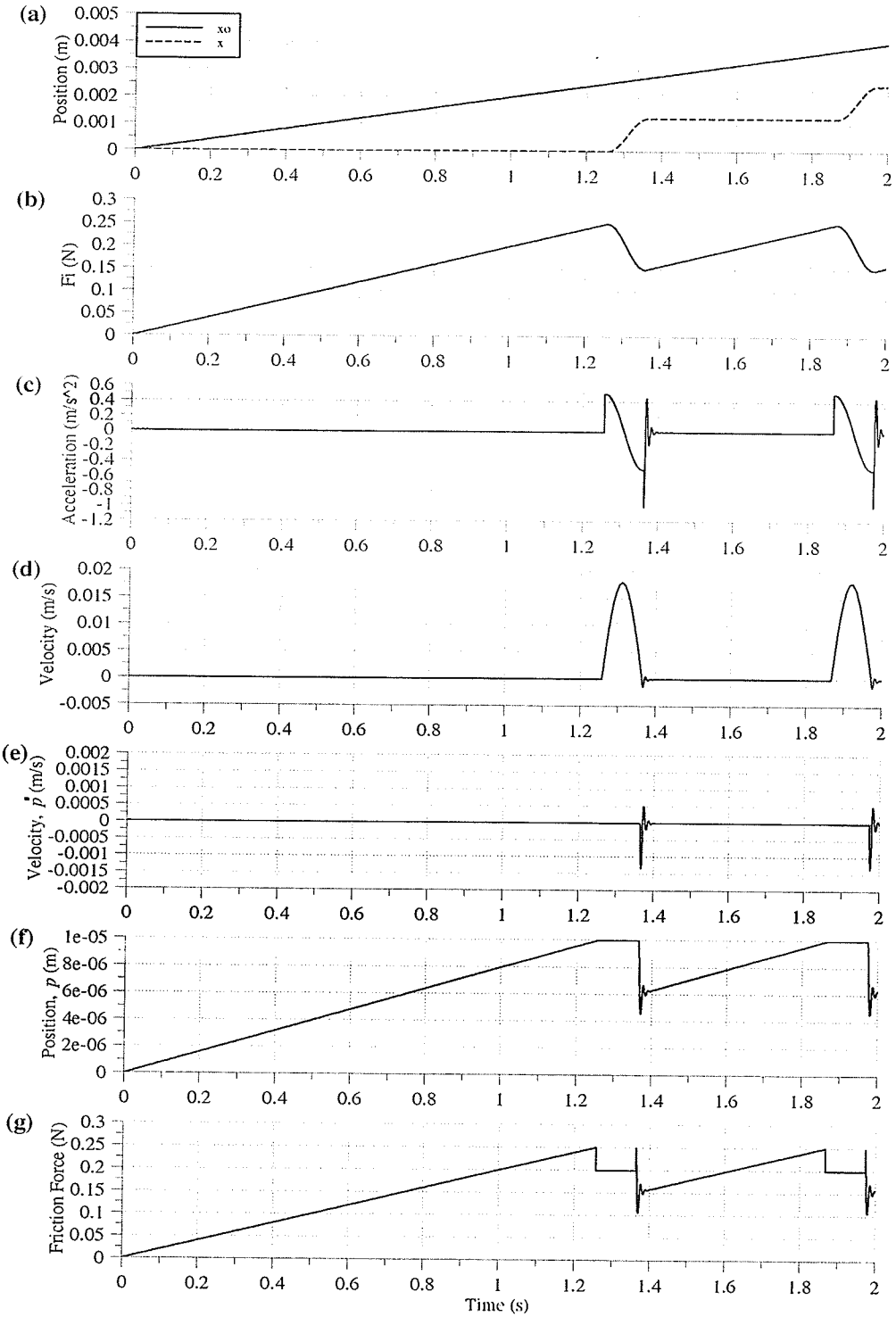

Figure 20 One-dof spring-mass, Reset Integrator model: (a) displacements; (b) F_i; (c) $\dot{V}$; (d) V; (e) $\dot{p}$; (f) p; and (g) F_i.

2.4 Summary

In the spring-mass and manipulator simulations, the Reset Integrator excels in the area of simplicity; however, the Karnopp model pulls through in computing times and accuracy. The Reset Integrator model is mathematically simpler than the Karnopp model. It is true that the Karnopp model has less parameters to consider, but its downfall is that it is not a true stand-alone friction model. That is, the Karnopp model has to be modified for each different application. The Reset Integrator is simple to use because it is truly a stand-alone friction model allowing the user to worry less about having to derive the model for each different application. For example, the Reset Integrator can easily model coulomb friction in multiple degree-of-freedom manipulators whereas the Karnopp model has to make questionable assumptions to move on. The crucial problem with the Karnopp model is including the kick-back accelerations in the two-degree-of-freedom manipulator. On the other hand, it shows consistent efficiency in computation time and has better accuracy in representing the classical stick-slip friction model. The Reset Integrator model is not too reliable and not too accurate. In some cases, the Reset Integrator simulations slow down where there is significant dissipating oscillations in the static regions. The Reset Integrator model can slow down computation time as much as three times slower than the Karnopp model for the manipulator simulations. Also, the Karnopp model is more accurate in a sense that it stays within the limits of the given values of stick friction, whereas the Reset Integrator model sometimes predicts stick friction values greater than the maximum defined. If the Reset Integrator's representation of static friction, which is the possible reason for its inaccurate static friction forces and its inconsistent computing times, were rectified, then the model would be an asset for modelling coulomb friction.

Chapter 3 Friction Compensation

The dynamics of a one-degree-of-freedom, gravity-independent manipulator with stick-slip friction is as follows:

$$T_i = J\ddot{\theta}_a + nb\dot{\theta}_a + T_f \tag{26}$$

where θ_a is the actual position, n is the gear ratio, b is the motor viscous friction, and J is the total inertia. T_f is the stick-slip friction disturbance described in the classical format as below:

$$T_f = \begin{cases} T_i & \dot{\theta}_a = 0, \quad |T_i| \le T_s \\ T_s sgn(T_i) & \dot{\theta}_a = 0, \quad |T_i| > T_s \\ T_d sgn(\dot{\theta}_a) & \dot{\theta}_a \neq 0 \end{cases} \tag{27}$$

The applied torque is $T_i = nK_tK_av(t)$, where K_t is the motor torque constant, K_a is the current amplifier gain, and $v(t)$ is the control voltage input to the amplifier.

We first start with having a PD control which is widely used because of its simplicity. More advanced controllers also often incorporate PD control such as computed torque or resolved-acceleration controls. We then build the featured compensation strategies around it. The control signal, $v(t)$, can therefore be written as follows:

$$v(t) = K_p\theta_e + K_d\dot{\theta}_e + v_c(t) \tag{28}$$

where $\theta_e = \theta_d - \theta_a$ is the error signal, K_p and K_d are the proportional and the derivative gains, respectively. $v_c(t)$ is the compensation signal.

The block diagram of the control system is given in Figure 21. I represents the motor current and τ is the motor torque before the gear transmission. The featured

compensators are plugged-in to the compensator block and will produce the added compensation voltage, $v_c(t)$.

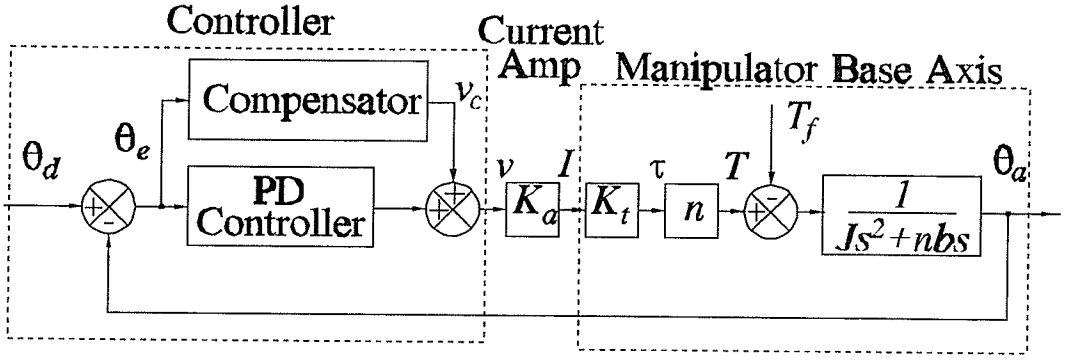

Figure 21 Control block diagram of an electric-driven manipulator base with feedback compensation.

3.1 Overview of Compensation Controllers

3.1.1 Reset Integral

The simplest integral action is the conditional reset integral described as follows:

$$v_c(t) = \begin{cases} v_c(t-\delta t) + K_i \theta_e \delta t & |\theta_e| \le \theta_{ri} \\ 0 & |\theta_e| > \theta_{ri} \end{cases} \tag{29}$$

where K_i is the integral gain, θ_{ri} is the range in which the integral action is active, and δt is the sampling time. The integral is only active at small position errors to reduce the effect of the integral windup due to large position step changes. The use of such an integral action, however, is not without a price, and may promote limit cycles with some types of friction models [33,39,43]. The block diagram of the reset integral is given in Figure 22a.

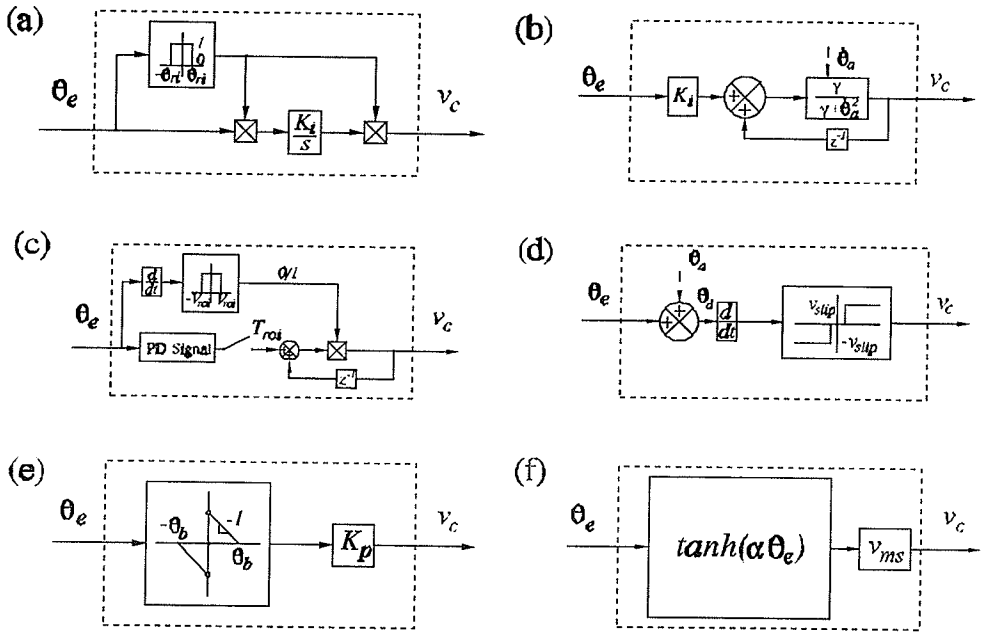

Figure 22 Selected compensation techniques: (a) RI; (b) RVI; (c) ROI; (d) Feedforward; (e) DNPF; (f) SRNF.

3.1.2 Rate Variable Integral

Morse et al. in [29] developed a variation of an integral action in which the integrator is coupled with a rate-varying multiplier. The method, termed Rate-Variable Integrator (RVI), is tuned low at high speeds to permit smooth tracking without overshoot. At low speeds, the integral action in tuned high to remove the steady-state errors. This method is seen to substantially reduce the errors due to mechanical stiction and to improve settling time and repeatability. With reference to Figure 22b, the RVI signal is formulated as follows:

$$v_c(t)=[v_c(t-\delta t)+K_i\theta_e\delta t]\left(\frac{\gamma}{\gamma+\dot{\theta}_a^{\,2}}\right) \tag{30}$$

where $\gamma/(\gamma+\dot{\theta}_a^2)$ is called the rate-varying factor. The rate-varying factor can be as high as unity when the actual velocity, $\dot{\theta}_a$, is zero, indicating a full power of the integrator, and approaches zero in a continuous fashion as the velocity increases. The integral control is therefore active when the load velocity is low in which period, sticking is imminent. The constant gain, γ, in Equation (30) actually determines a cutoff velocity between what is high and what is low.

3.1.3 Reset Offset Integral

Towards eliminating steady-state errors observed in a class of PD-controlled hydraulic manipulators, an algorithm was proposed [35] which uses an integrator termed the Reset-Offset Integrator (ROI), whereby the control measure of the steady-state error obtained from PD control is used as an offset to be added to the current control action. The integrator action is only active when the absolute velocity error $(\dot{\theta}_d-\dot{\theta}_a)$ becomes smaller than a certain value, V_{roi}. A zero velocity error is the indication of a system which has come to a steady-state error and that the PD controller has done all it could to reduce the error. The PD controller output is then essentially a measure of the steady-state error. This measure is therefore utilized as an added control, namely offset. Referring to the block diagram in Figure 22c, upon the activation of the offset integral block, two loops become active: the integrator loop and the timer loop. The timer loop delays incrementing the compensation control signal, $v_c(t)$, until the desired time, T_{roi}, has elapsed. This loop then forms a new offset control signal to be added to the PD control signal, v_{PD}. Referring to Figure 22c, the ROI signal is formulated as follows:

$$v_c(t)=v_c(t-T_{roi})+v_{PD} \tag{31}$$

The compensator block remains active as long as the velocity error remains within the threshold V_{roi}. When the velocity and position errors reduce to zero, the PD control output goes to zero and the offset value remains constant. When the velocity error exceeds the zero neighbourhood, defined by V_{roi}, the offset is set to zero and stays

inactive. This is done by multiplying the forward path of the integrator loop by a zero (see Figure 22c). This integrator in fact belongs to the class of conditional integrators. Utilizing velocity error instead of velocity to control the integration rate, has an advantage in that, the integral will only reset in situations where windup is a possibility, i.e., when the set point is changing too rapidly for the system to follow or during the velocity reversal.

3.1.4 Feedforward Compensation

The feedforward compensator eliminates friction effects in a different manner than the other selected compensators. Instead of getting friction information from feedback, this compensator relies on offline friction information and applies it to the controller in a feedforward fashion. Feedforward has the advantage of producing a smoother control signal as compared to that of feedback [8]. Also, according to Dupont and Armstrong-Hélouvry [11], feedforward is the most commonly used technique for friction compensation. With reference to the block diagram in Figure 22d, the feedforward signal is as follows:

$$v_c(t) = \begin{cases} v_{slip} sgn(\dot{\theta}_d) & |\dot{\theta}_d| > V_{ff} \\ 0.0 & |\dot{\theta}_d| \le V_{ff} \end{cases} \tag{32}$$

Tuning the feedforward compensator involves only adjusting the velocity range, V_{ff}. Offline identification of the slip friction voltage equivalent is also required.

3.1.5 Discontinuous Nonlinear Proportional Feedback

The Discontinuous-Nonlinear-Proportional Feedback (DNPF) compensator proposed by Southward et al. [39] falls in the class of nonlinear bang-bang control. This compensator has been tested numerically, and within limited experiments not including implementation

on an actual manipulator. Referring to the block diagram in Figure 22e, the DNPF compensation signal is generated as follows:

$$v_c(t) = \begin{cases} 0 & |\theta_e| > \theta_b \text{ or } \theta_e = 0 \\ K_p[\theta_b sgn(\theta_e) - \theta_e] & otherwise \end{cases} \tag{33}$$

where

$$\theta_b = \frac{v_{stick}}{K_p} + \varepsilon \tag{34}$$

The value, v_{stick}, is a voltage-equivalent value equal to the maximum value of stick friction torque resistance and ε is a positive value to insure the compensation signal exceeds this value. Tuning the DNPF compensator involves a knowledge of the stick friction value.

3.1.6 Smooth Robust Nonlinear Feedback

The Smooth Robust Nonlinear Feedback (SRNF) compensator proposed by Cai and Song in [6], uses the hyperbolic tangent function for compensation. With reference to Figure 22f, the compensation signal is generated as follows:

$$v_c(t) = v_{ms} \tanh(\alpha \theta_e) \tag{35}$$

$$v_{ms} = v_{stick} + \varepsilon \tag{36}$$

v_{stick} once again represents the maximum voltage-equivalent value of stick friction, and ε is a positive value ensuring that the value, v_{ms} is greater than the voltage-equivalent value of stick friction, just as in the DNPF compensator. The value, α, is a positive number used to adjust the degree of smoothness of the hyperbolic function $\tanh(\alpha\theta_e)$. Changing α will change the shape of the function tanh(...) with the extreme cases of being a bang-bang controller as $\alpha \to \infty$ and having no compensational effects as $\alpha \to 0$. To our knowledge, the SRNF compensator has not yet been implemented in any experimental situation despite its theoretical backing.

3.2 Experimental Test Station

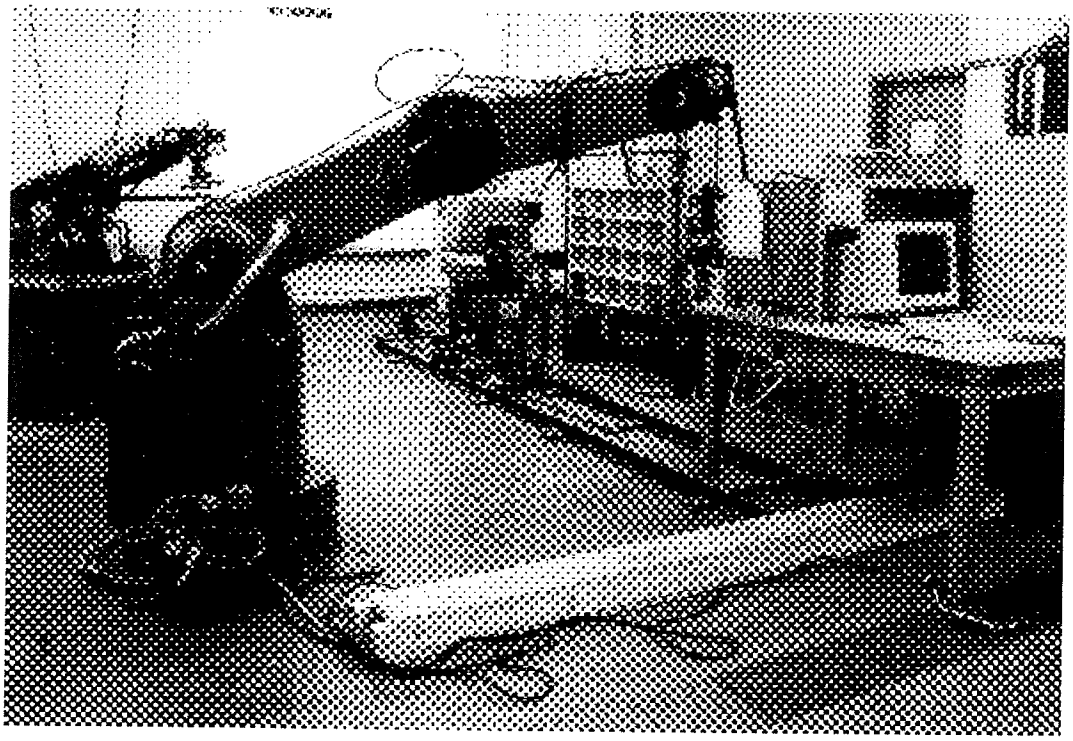

Figure 23 DK robot experimental test station.

An electrically actuated, GCA/DK-2600 five degree-of-freedom articulated robot with harmonic drive transmission was retrofitted with an external controller to establish a platform for experimentally testing various control algorithms. The main feature of the test station is its open hardware structure with high computational capacity and good software programmability so as it can easily take on different controls. A picture of the DK robot is given in Figure 23 and a block diagram of the hardware configuration for this testbed is shown in Figure 24. The components of the external controller consist of a 486/50MHz personal computer with a Metrabyte M5312 quadrature incremental encoder card, a DAS-16 analog-to-digital (A/D) card, and a DDA-06 digital-to-analog (D/A) card. The encoder card reads encoder signals from the DK robot's native quadrature encoders which have an accuracy of ±0.00242 deg. The A/D card is capable of receiving ±5 V signals from input devices, such as a joystick, with an accuracy of ±0.00488 V. The D/A

card is capable of sending ±5V signals with an accuracy of ±0.00488 V to the current amplifiers. The Pulse-Width-Modulated (PWM) current amplifier that drives the base DC motor works at a switching frequency of 22 KHz and converts the input voltage signal to an output current at a gain of 3 A/V. The rectified DC power supply originates from the manipulator native controller AC power supply. The sampling time was selected at 20 ms. Joint velocities are calculated from the joint position data using five-point linear regression.

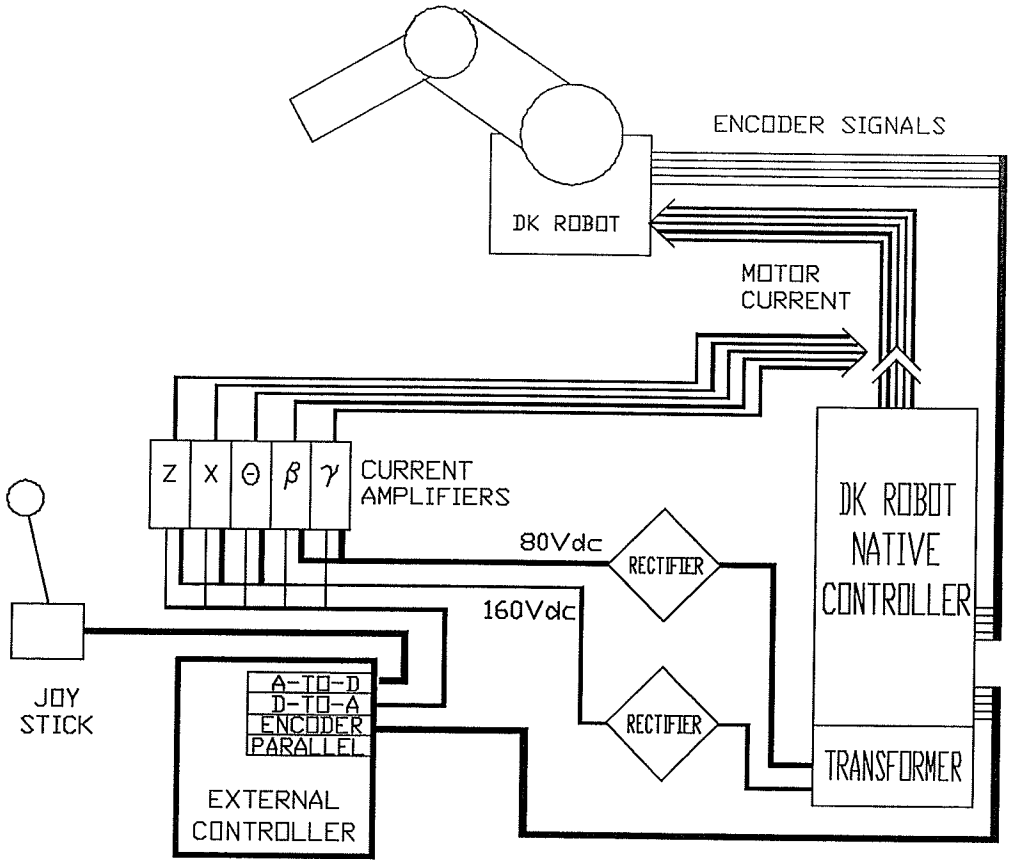

Figure 24 Experimental test station block diagram.

Preliminary experiments were performed to estimate the amount of torque dissipated through stick-slip friction on the base axis. Similar tests to identify friction dissipation can be found in [27,4]. The value of stick friction was estimated by slowly ramping up

the motor torque via the control signal on the base joint from rest until it began to move. A value for slip friction was estimated by slowly decrementing the motor torque via the control signal on the slow moving joint until it stopped. We repeated these tests along the range of the axis in both directions of rotation. On average, a control input of approximately 0.40 V was required to overcome stick friction torque resistance and 0.38 V to overcome slip friction torque resistance. With the current gain, K_a=3.0 A/V, motor torque constant, K_t=0.1 Nm/A, and the gear ratio, n=1800 (500:1 for harmonic drive, 3.6:1 for spur gear), the total torque required to overcome stick and slip friction was 216 Nm and 205 Nm, respectively. These torques were ≈8% of the total achievable motor torque of 2700 Nm.

3.3 Experimental Evaluation

3.3.1 Benchmark Tests

The experimental benchmark consisted of a number of desired paths for the purpose of comparing different characteristics of the featured control systems. Two sets of tests have been chosen. The first set consists of three step inputs: 5.0 deg, 2.5 deg, and 1.0 deg, to evaluate the controller's ability to regulate and to clearly display transient responses. The second test was a set of two trajectories, to test the ability for following the reference changes. We generated the trajectories using the method outlined by Paul in [31]. Referring to Figure 25, the tracking tests were a 50 deg rotation in both directions at 5.0 deg/s, and a 25 deg rotation at 2.5 deg/s.

In our experiments, we tuned the PD control gains and the parameters of the compensators to produce a response with the least amount of overshoot, fast rise- and settling-time for the step input response of 2.5 deg. The gains and parameters were then kept fixed throughout the remaining tests, including the tracking responses. An overview of the gains and parameters used for each controller are given in Table 17.

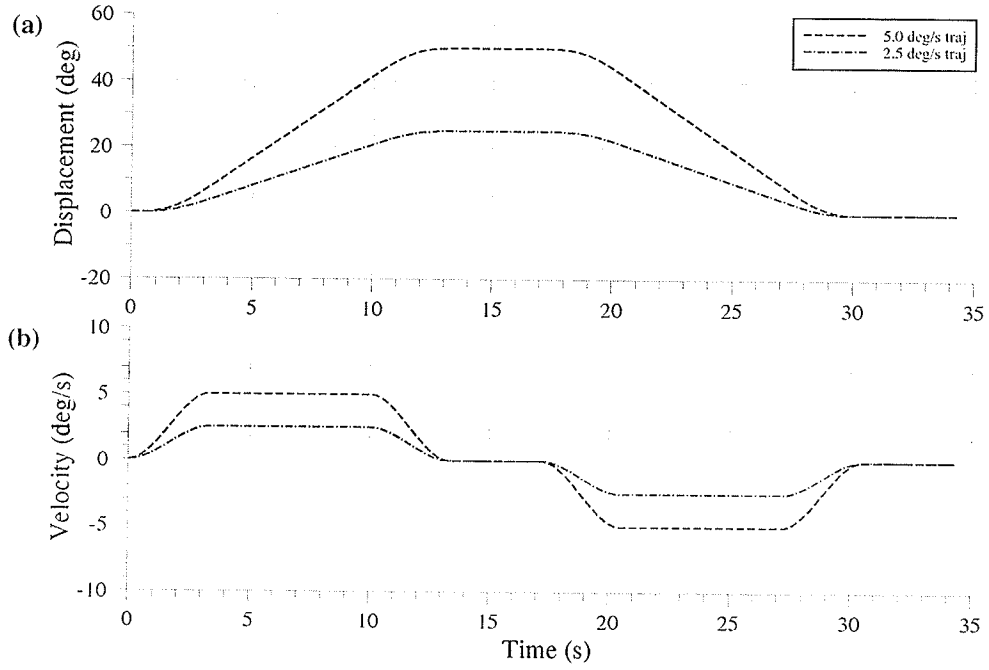

Figure 25 Experimental benchmark trajectories: (a) displacements; (b) velocities.

Table 17 Parameters for selected compensators.

Controller	K_p V/deg	K_d V/(deg/s)	Compensator Parameters
PD	1.0	0.15	N/A
PD w/RI		0.17	K_i=4.0 V/(deg·s), $\lvert\theta_e\rvert$ <0.5 deg
PD w/RVI			K_i=150 V/(deg·s), β=0.05 (deg/s)^2
PD w/ROI			T_{roi}=140 ms, V_{roi}=2.33 deg/s
PD w/Feed forward			V_{ff}=0.001 deg/s, v_{slip}=0.37 V
PD w/DNPF			θ_b=0.40 deg
PD w/SRNF		0.25	v_{ms}=0.40 V, α=100 deg^{-1}

3.3.2 PD Control

The responses to the three step inputs as well as the response with an added friction to the 5.0 deg step are shown in Figure 26. The added friction was produced by applying a braking force to the gravity-independent axis. All responses displayed different frictional effects. Depending on the initial conditions, gains, and the values of stick-slip friction, a nonzero equilibrium resulted with a phase portrait similar to those obtained in [33]. In the trajectory responses, steady-state errors resulted, just as in the step input responses, in addition to tracking errors. The tracking errors and control signal are shown in Figure 27. The position error, and the control signal for the 5.0 deg/s trajectory was slightly larger than the 2.5 deg/s trajectory. This larger control signal is believed to be due to the increased viscous friction as a result of increased velocity.

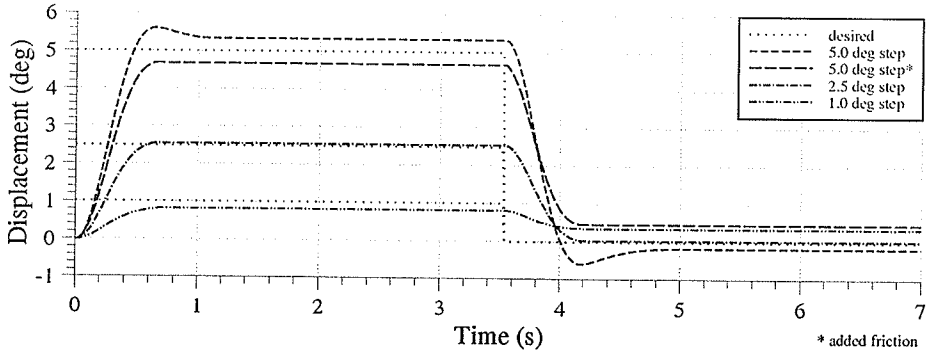

Figure 26 PD control step response displacements.

One way to overcome frictional disturbance is to increase the stiffness of the controller, i.e., by increasing the proportional and derivative gains. This however, has the drawback in that it makes the system sensitive to the payload, mechanical rigidity as well as the sensor characteristics. For example, in our experiment, when the proportional gain, K_p, was increased by five times and K_d was roughly doubled, the position error was reduced approximately four times. However, due to the noise amplification, the control signals were quite oscillatory (see also [9] for a similar observation). The noise in the encoder feedback signal was especially magnified when it was differentiated to calculate the

velocities. Experimental results of some of the selected compensators with high gains is given in Appendix A.2.

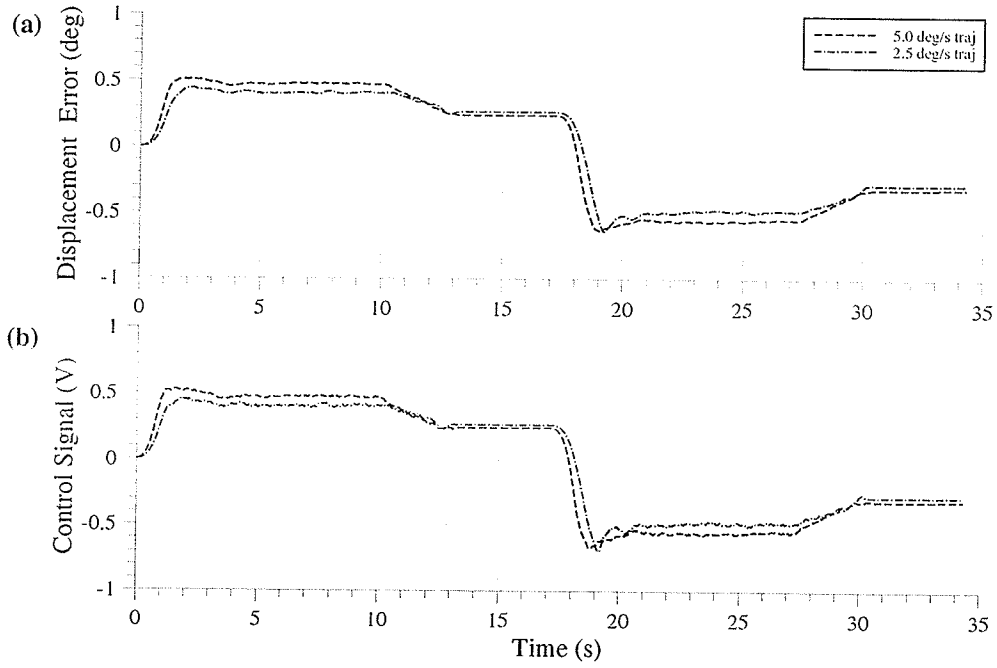

Figure 27 PD control trajectory responses: (a) displacement errors; (b) 5.0 deg/s control signal breakdown.

3.3.3 Reset Integral

The addition of the reset integral action reduced the steady-state errors in the step responses. However, the integral signal became slightly oscillatory (hunting around the set point) as seen in Figure 28. The integral signal did not wind down fast enough once stick friction was overcome, resulting in an overshoot, and consequently generated a limit cycle as cited by others [33,43]. The above observations suggest that the friction present in our experiments must have the same properties as stick friction, whereby there is an initial buildup and drop in force from the static to the dynamic level. This observation is consistent with the initial friction measurement as was described in Section 3.1. The trajectory responses, as shown in Figure 29, exhibited low steady-state and tracking errors.

Overall, the conditional reset integral action responses were too slow in eliminating stick friction effects, and if too high an integral gain was used, oscillations would arise in both tracking and regulating.

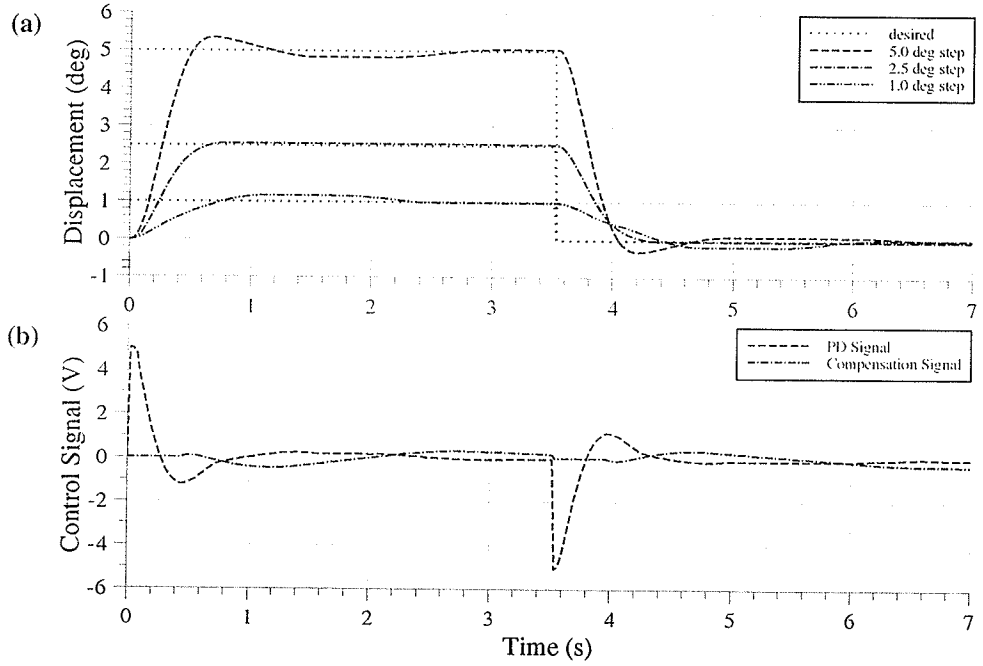

Figure 28 PD control w/RI compensation step responses: (a) displacements; (b) 5.0 deg control signal breakdown.

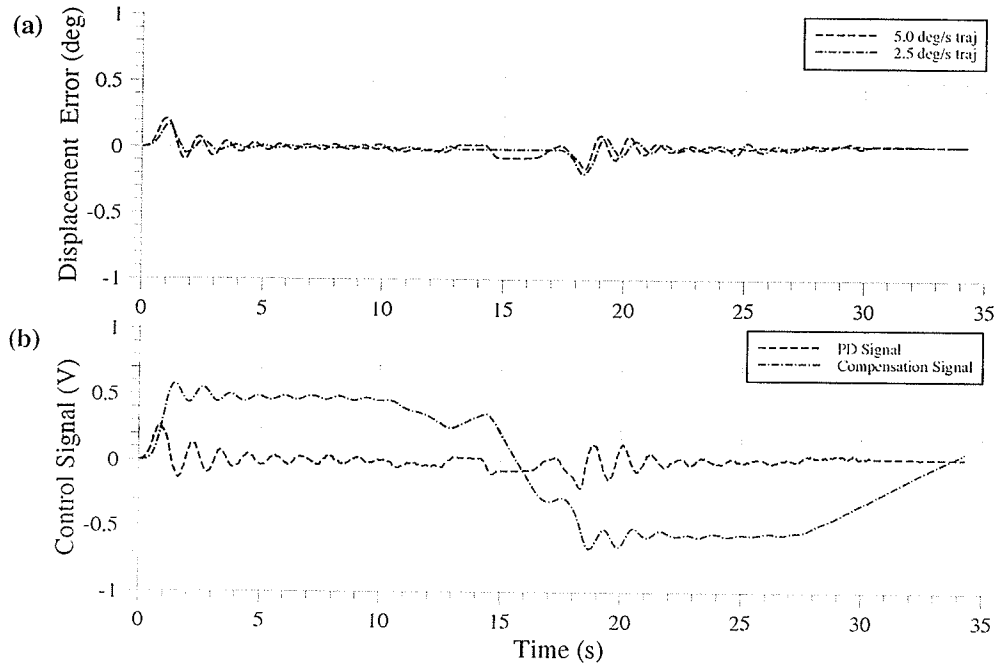

Figure 29 PD control w/RI compensation trajectory responses: (a) displacement errors; (b) 5.0 deg/s control signal breakdown.

3.3.4 Rate Variable Integral

Referring to Figure 30, the RVI worked well and was quite effective in eliminating steady-state errors. In the regulating tasks, the hunting due to stiction was eliminated, since the nonlinear rate varying factor, $\gamma/(\gamma+\dot{\theta}_a^2)$, allowed the use of higher integral gain at low velocities. Also, because the entire accumulated integral was iteratively multiplied by this factor, the integral seems to reset itself at high velocities thereby eliminating the problem of windup and overshoot. However, for that same reason, the integral failed to eliminate tracking errors in the trajectory responses as shown in Figure 31. These tracking errors are due to the fact that the method specifically pertains to controllers where the rate varying factor approaches zero in the presence of large velocities.

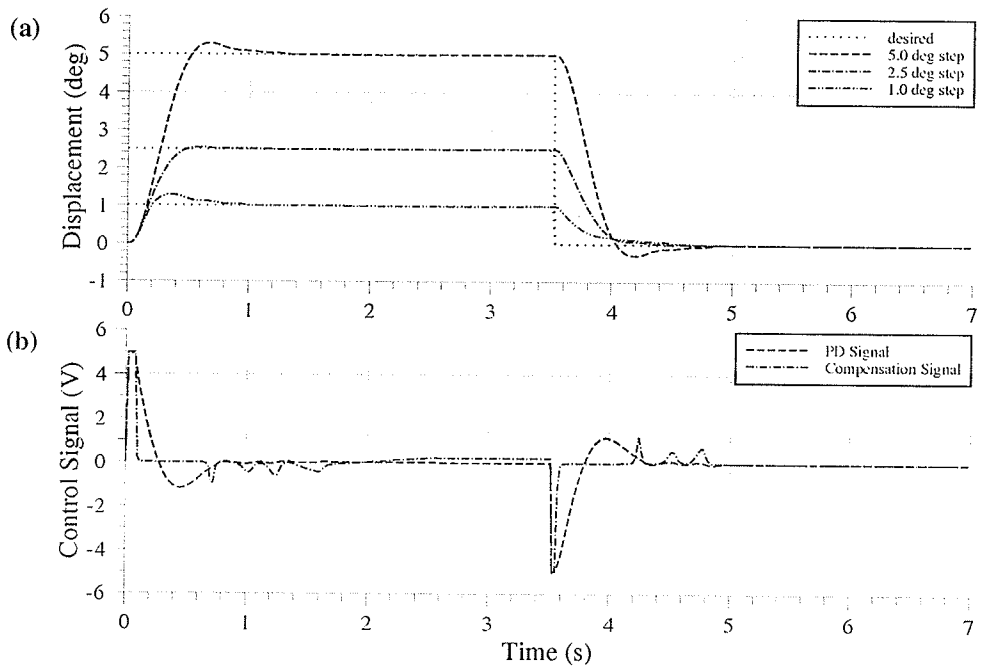

Figure 30 PD control w/RVI compensation step responses: (a) displacements; (b) 5.0 deg control signal breakdown.

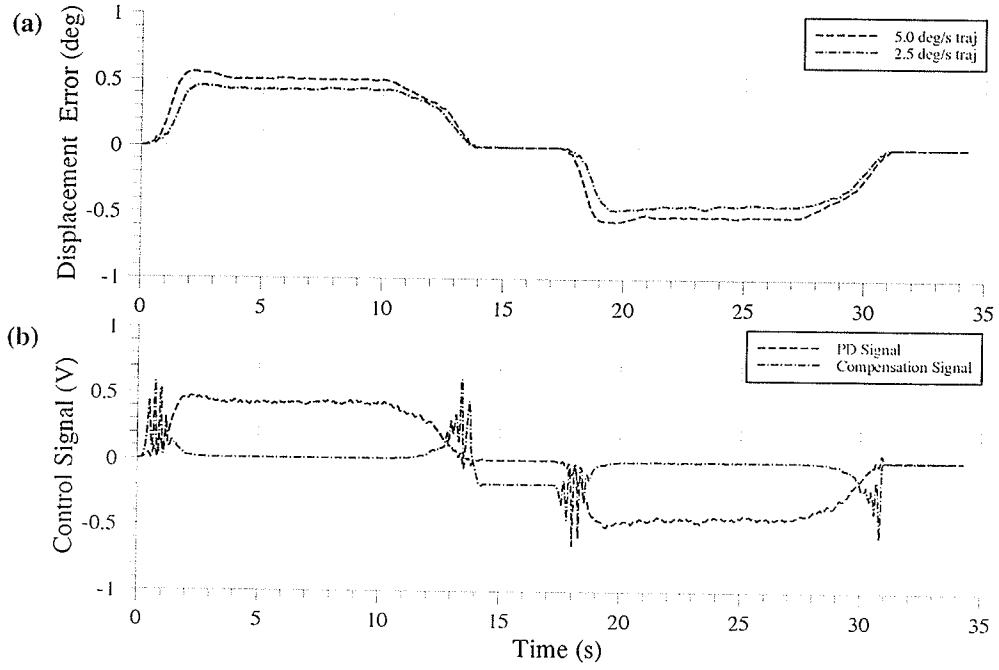

Figure 31 PD control w/RVI compensation trajectory responses: (a) displacement errors; (b) 5.0 deg/s control signal breakdown.

3.3.5 Reset Offset Integral

Since the ROI has similar traits to integral action, it was to no surprise that the results displayed some similarities. Nevertheless, the ROI compensator seemed to have better eliminated errors caused by stick friction than the reset integral action and better eliminated errors caused by slip friction than the RVI as shown in Figure 32a. Notice the stepping characteristic of ROI compensation signal in Figure 32b from the time interval, T_{roi}. The ROI action also seemed to increase the response speed during the trajectory tracking response, as seen by smaller tracking error sizes in Figure 33a compared to those of the RI action in Figure 29a. Overall, the ROI action seemed to sufficiently reduce the errors caused by friction using its own variation of integral action. There was less position error during tracking, than the rate-variable integral, without incurring any noticeable penalties for the step inputs. By keeping the velocity error threshold low enough, the ROI block would be active only during the initial response to a step, where the stiction

is imminent, and it would not be active at high speeds, thereby eliminating the integral windup problem as well.

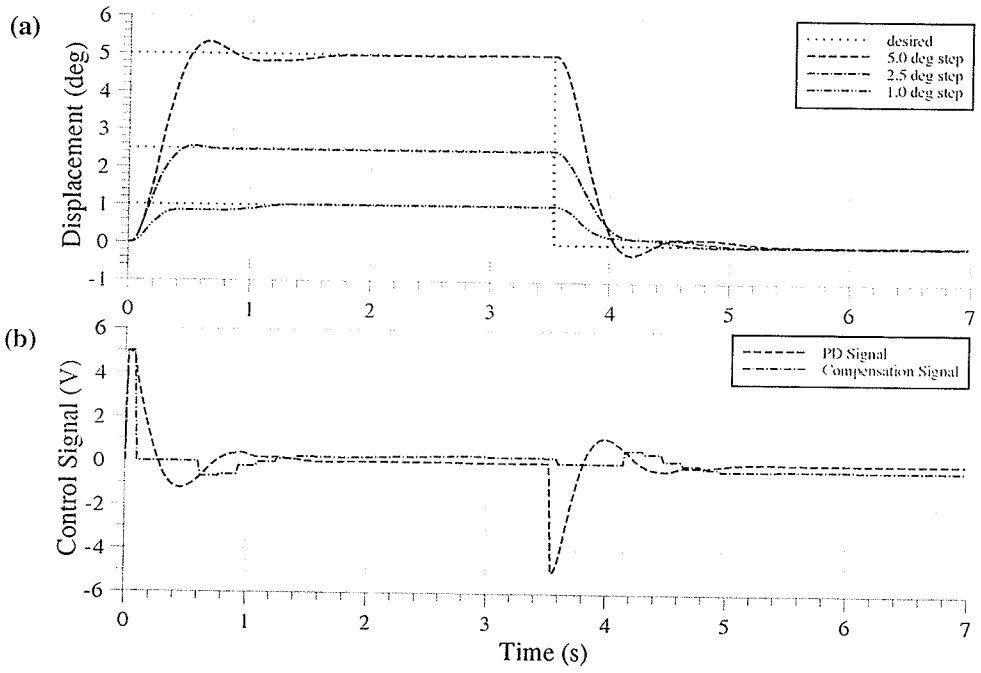

Figure 32 PD control w/ROI compensation step responses: (a) displacements; (b) 5.0 deg control signal breakdown.

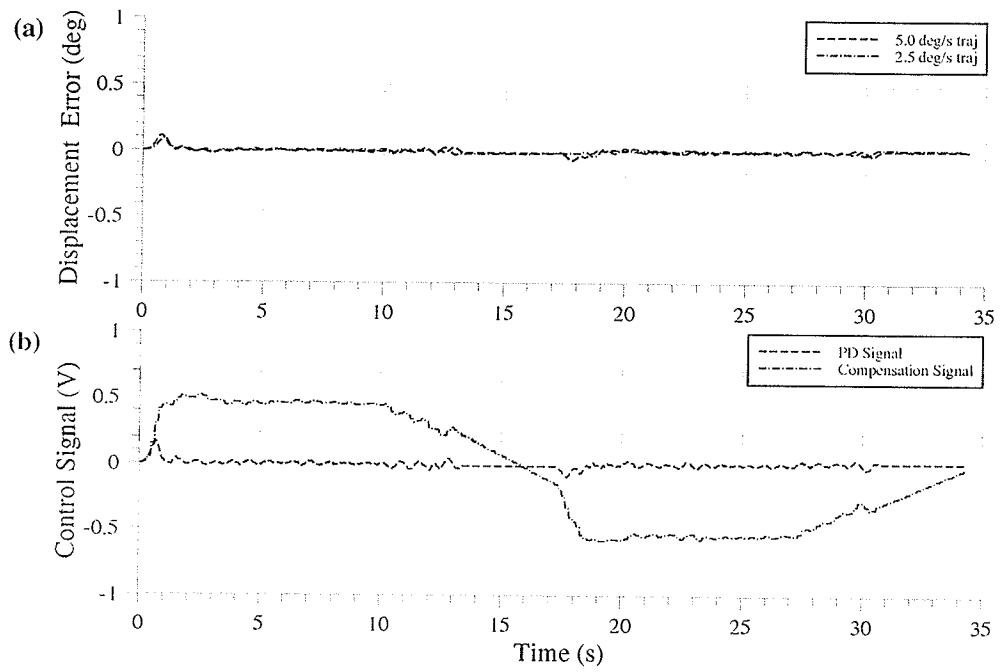

Figure 33 PD control w/ROI compensation trajectory responses: (a) displacement errors; (b) 5.0 deg/s control signal breakdown.

3.3.6 Feedforward Compensation

The proposed feedforward compensator eliminated slip friction errors with a smooth compensation signal, but did not eliminate stick friction errors. The feedforward slip friction compensator eliminated tracking errors as shown in Figure 35a with a smooth control signal. Overall however, this compensator displayed the stability of a slip friction compensation signal through feedforward action.

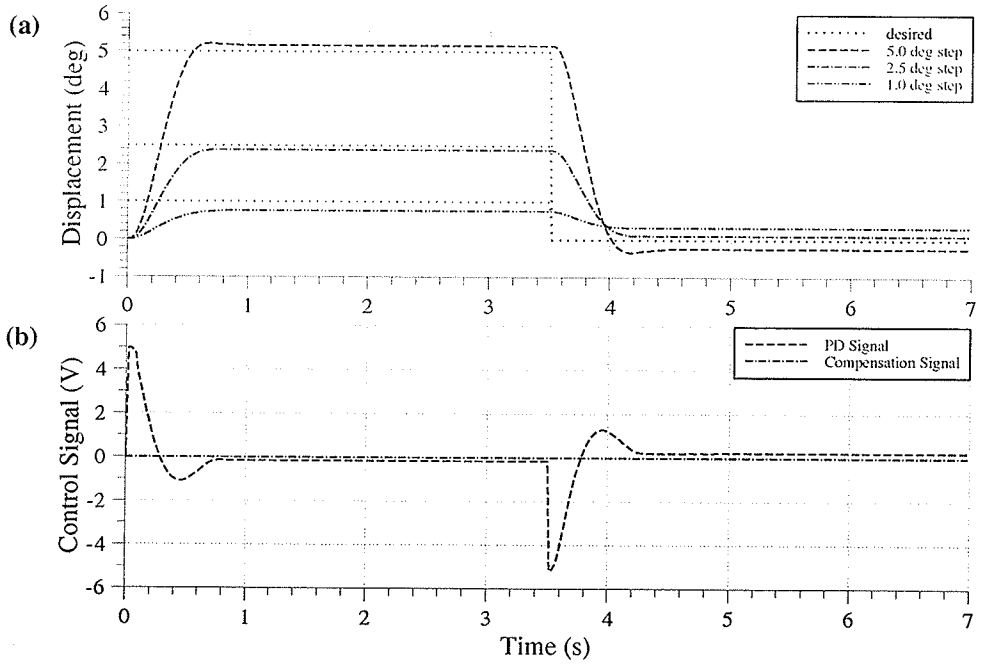

Figure 34 PD control w/Feedforward compensation step responses: (a) displacements; (b) 5.0 deg control signal breakdown.

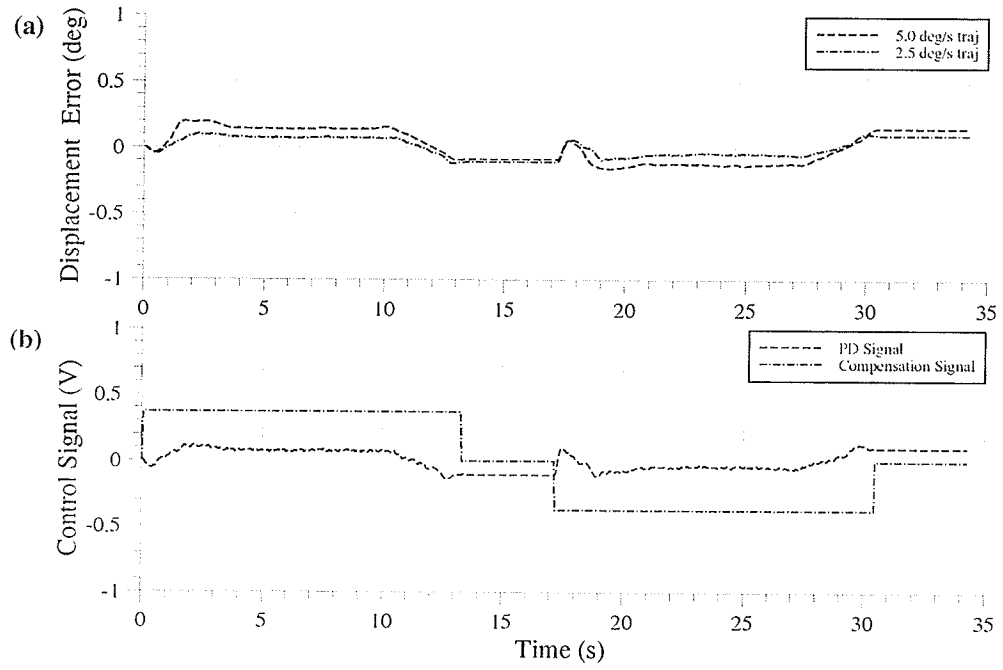

Figure 35 PD control w/Feedforward compensation trajectory responses: (a) displacement errors; (b) 5.0 deg/s control signal breakdown.

3.3.7 Discontinuous Nonlinear Proportional Feedback

The step response for DNPF compensation for the 5.0 deg step as shown in Figure 36a displayed a steady-state error. This error is most probably the result of stick friction being undercompensated. The system might have been experiencing friction breakaway characteristics as a function of angular position. In the 1.0 deg and 2.0 deg steps, the compensator eliminated the steady-state error. The breakdowns of the total control signal into compensation signal, $v_c(t)$, and PD control signal, $v_{PD}(t)$, for the 5.0 deg and 2.5 deg steps are shown in Figure 36b and Figure 36c. These oscillations seen in Figure 36c are from the discontinuous nature of the DNPF compensator at zero position error producing a bang-bang effect. Care must be taken in choosing a value for ε in Equation (34) - too large a value will overcompensate stick friction and may cause sustained oscillation; too

small a value will leave steady-state errors. Our observation showed that the DNPF compensator is quite sensitive to this parameter.

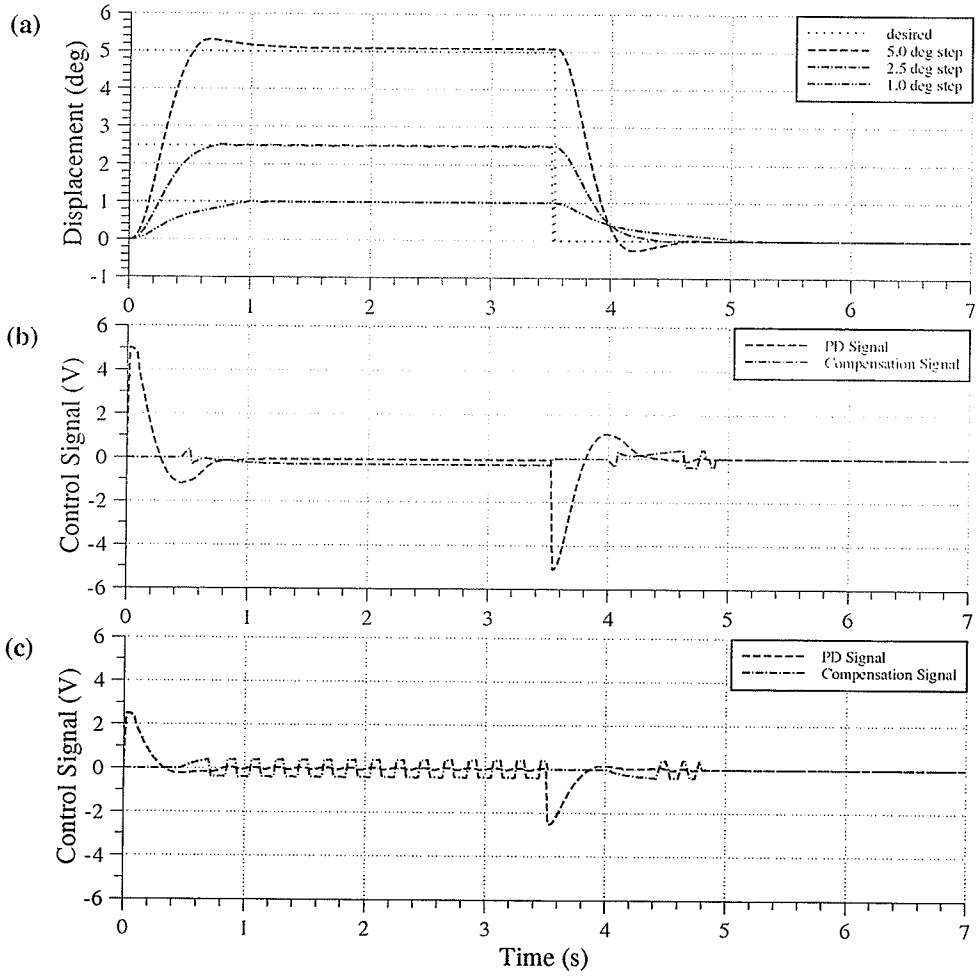

Figure 36 PD control w/DNPF compensation step responses: (a) displacements; (b) 5.0 deg control signal breakdown; (c) 2.5 deg control signal breakdown.

As for the trajectory responses, the tracking errors of the DNPF compensator in Figure 37a was as large in magnitude as those in a simple PD controller responses. Also, referring to Figure 37b, the trajectory control signal displayed some oscillatory behaviour when the manipulator was brought to a stop in either direction. The compensator was only active during small position errors; once the position error exceeded the range of $\pm\theta_b$

in Equation (33), there was no friction compensation. Referring to Figure 37b, oscillations also appeared at the beginning of the trajectory since the position error was still in the range of $\pm\theta_b$.

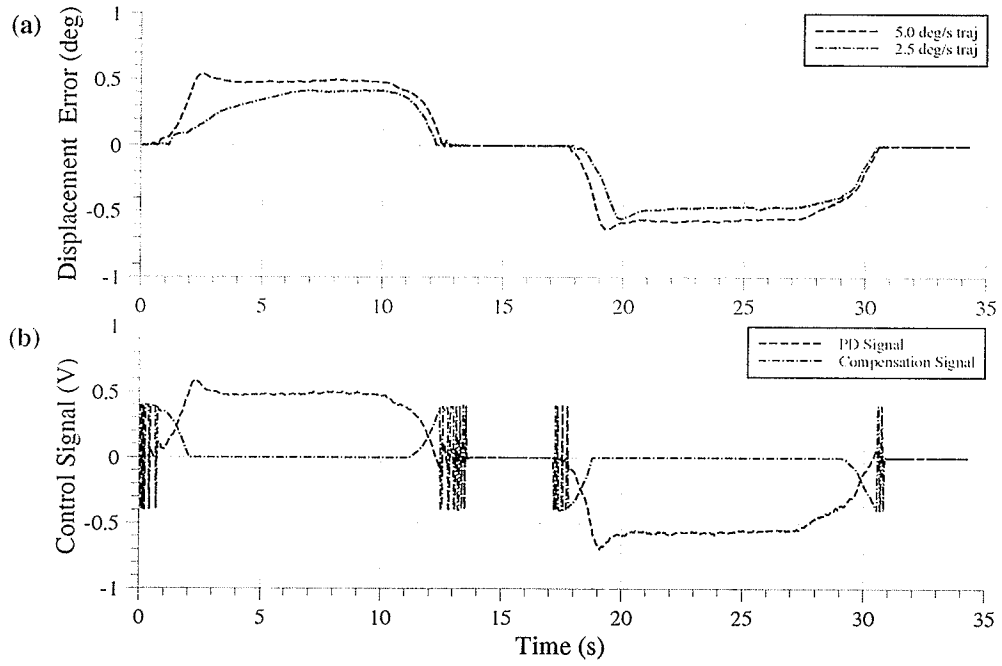

Figure 37 PD control w/DNPF compensation trajectory responses: (a) displacement errors; (b) 5.0 deg/s control signal breakdown.

Generally, the DNPF compensator performs similar to a bang-bang controller. The bang-bang control effect occurs around the zero position error, but when given ample time, these oscillations stop and the compensator eliminates the steady-state error. Bang-bang compensation should, however, be avoided since, sudden changes in torque magnitudes could be potentially harmful to the long-term wear of the hardware [6]. For the DK robot, the magnitude of these impulsive torques were in the range of ±220 Nm.

3.3.8 Smooth Robust Nonlinear Feedback

The responses of the SRNF compensator improved to those of the previous compensators. The parameters of this compensator, v_{ms} and α, were first adjusted to have the least amount of overshoot for the step input responses of 2.5 deg. The responses shown in Figure 38, possess significantly reduced steady-state errors. The tracking performances, using the same gains as in the step responses, are shown in Figure 39. The larger tracking error presented in the 5.0 deg/s as compared to the 2.5 deg/s is due to the increased viscous friction resistances. Referring to Figure 39b, the SRNF compensator eliminated both stick and slip friction by having a bang-bang type action to eliminate stick friction errors and a constant signal to eliminate slip friction effects.

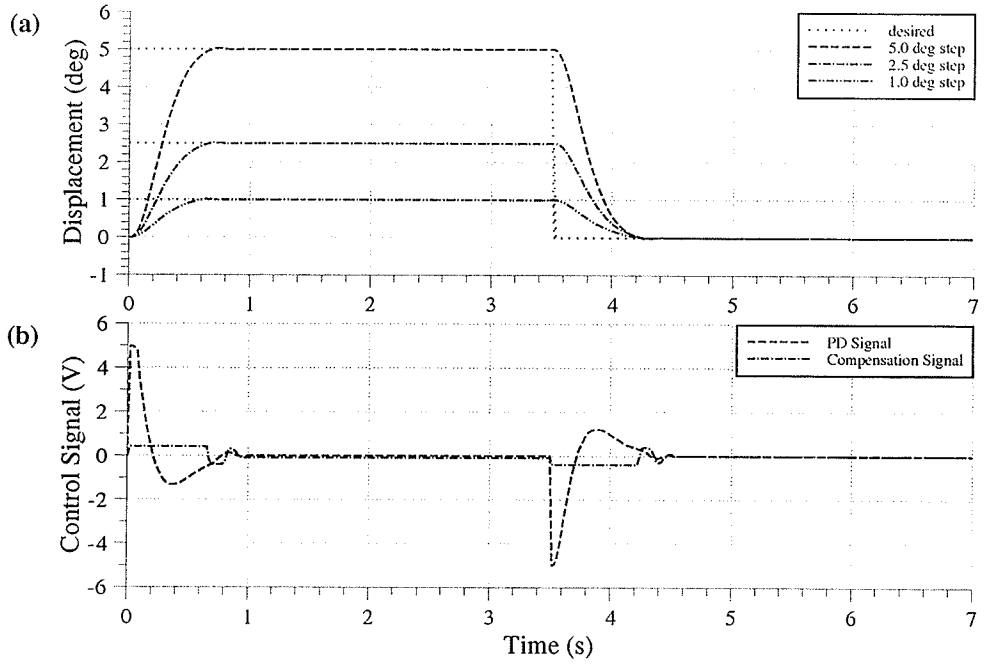

Figure 38 PD control w/SRNF compensation step responses: (a) displacements; (b) 5.0 deg control signal breakdown.

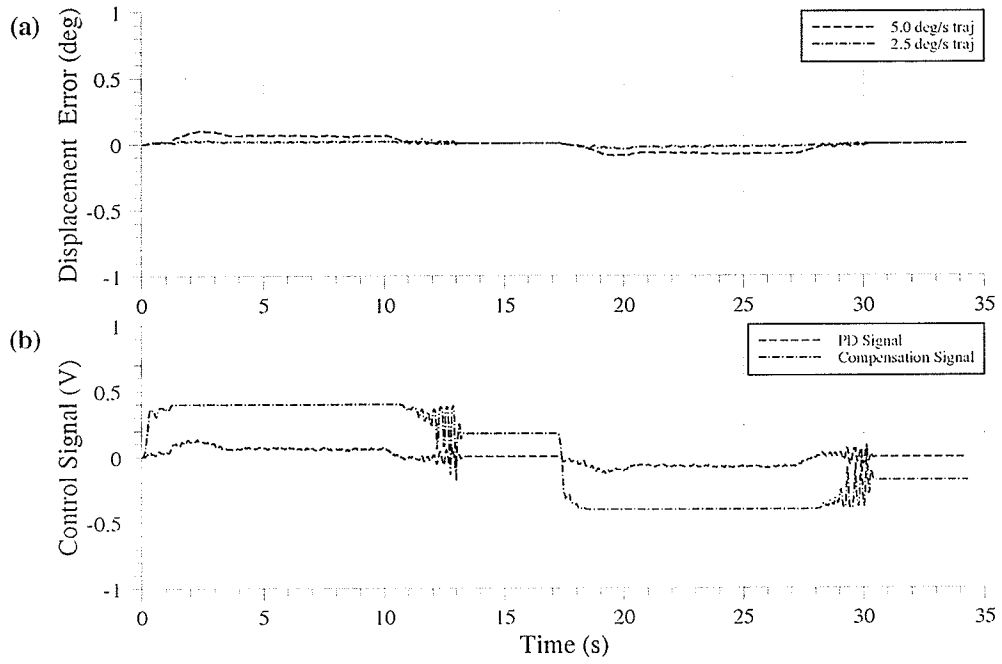

Figure 39 PD control w/SRNF compensation trajectory responses: (a) displacement errors; (b) 5.0 deg/s control signal breakdown.

3.3.8.1 Robustness Tests

Table 18 Parameters for SRNF compensation Robustness Test.

Test	v_{ms} (V)	α (deg^{-1})
1	0.5	100
2	0.2	100
3	0.4	300
4	0.4	5.0

To bring further insight into the SRNF compensator, more tests were performed with variations on the values of the parameters, v_{ms} and α. The step responses were excluded from these tests since the trajectory responses show roughly the same results. The values used for each test are given in Table 18. When the value of v_{ms} increased, i.e. the friction

was overcompensated, the tracking errors decreased as shown in Figure 40a. Overcompensating the friction may, however, risk giving rise to the control signal oscillations as is seen from Figure 40b. Using a low value of v_{ms} produced large tracking errors as shown in Figure 41a. This is due to undercompensating the stick friction as shown by the low compensation signal in Figure 41b. As shown in Figure 42, using a high value for α produced oscillatory control signals similar to the case in which a high value of v_{ms} was implemented. The oscillations, however, did not originate from overcompensating friction, but rather from transforming into a discontinuous (bang-bang) compensator. Slip friction, however, was still compensated by a constant signal (Figure 42b). As shown in Figure 43, reducing α made tanh(...) less effective, and produced this result. Throughout these tests, however, the SRNF compensator remained stable. These tests therefore strengthen the claim of Cai and Song in [6]: the SRNF compensator is indeed a robust compensator.

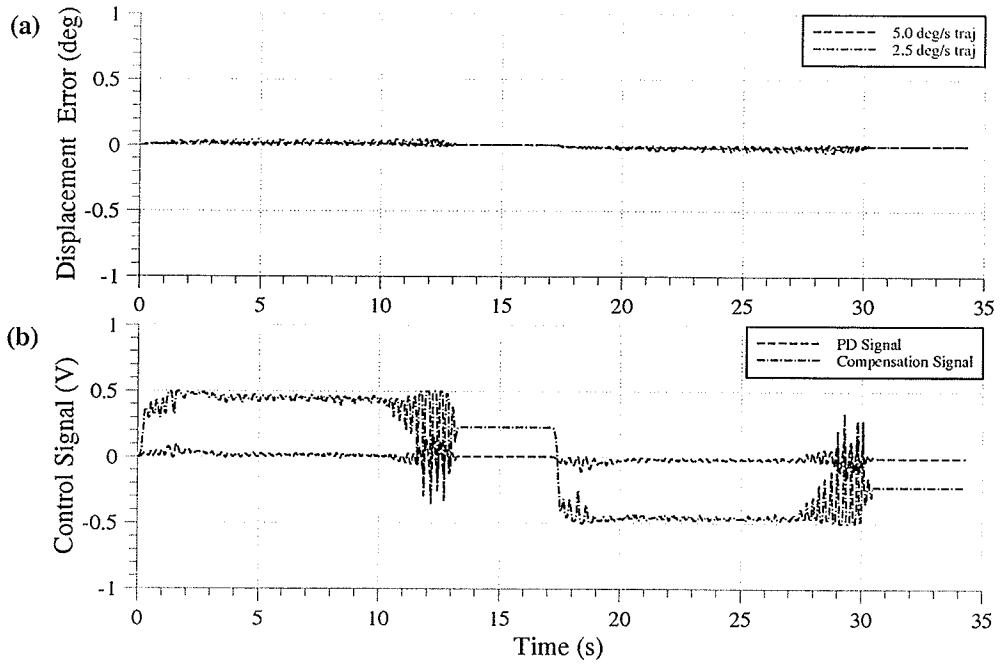

Figure 40 PD control w/SRNF compensation, Robustness Test 1: (a) displacement errors; (b) 5.0 deg/s control signal breakdown.

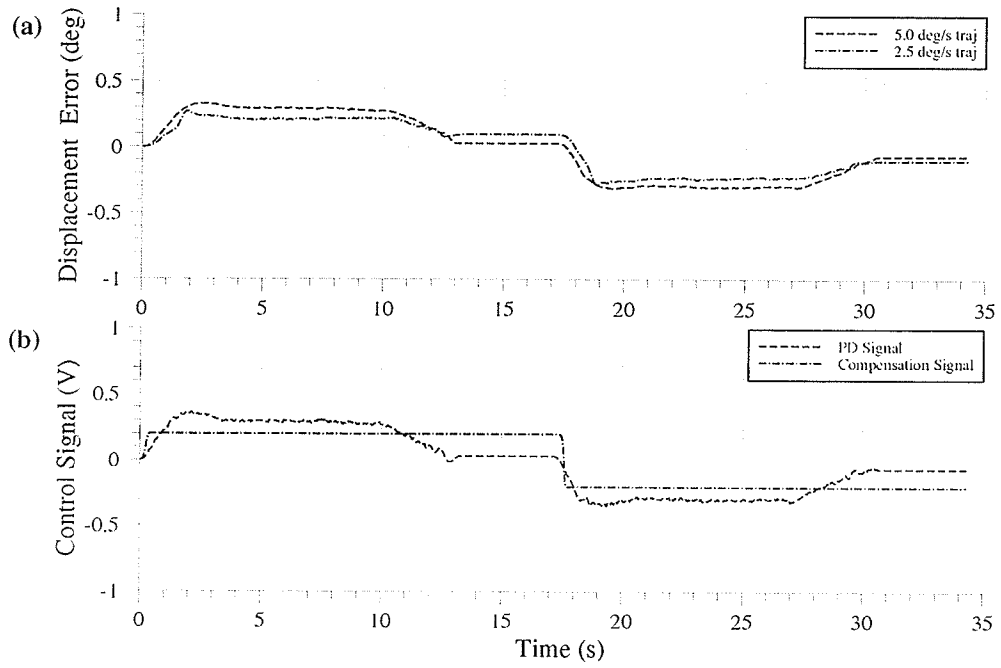

Figure 41 PD control w/SRNF compensation, Robustness Test 2: (a) displacement errors; (b) 5.0 deg/s control signal breakdown.

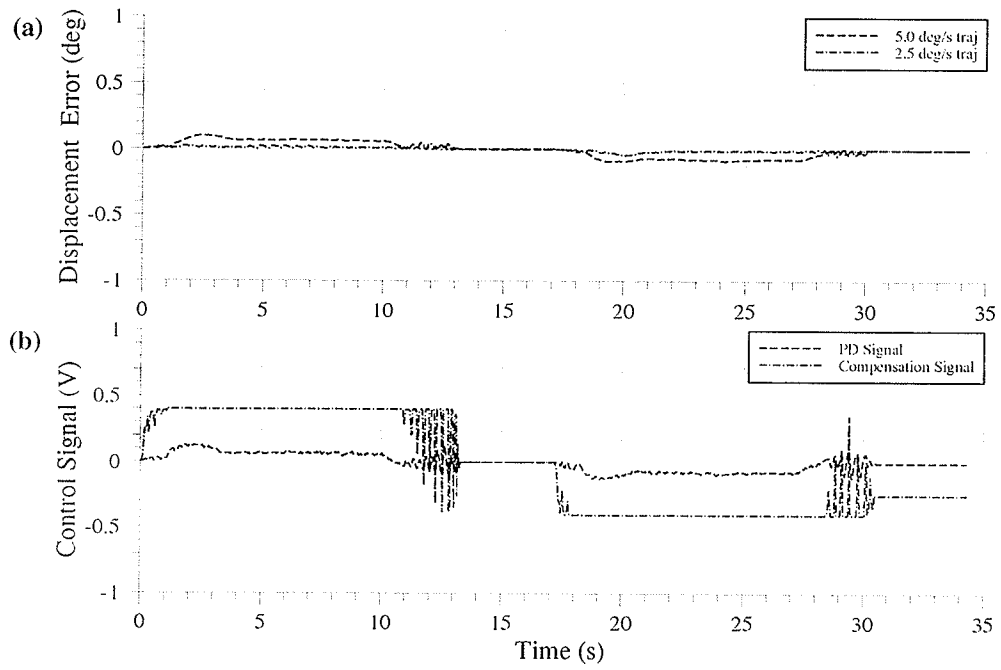

Figure 42 PD control w/SRNF compensation, Robustness Test 3: (a) displacement errors; (b) 5.0 deg/s control signal breakdown.

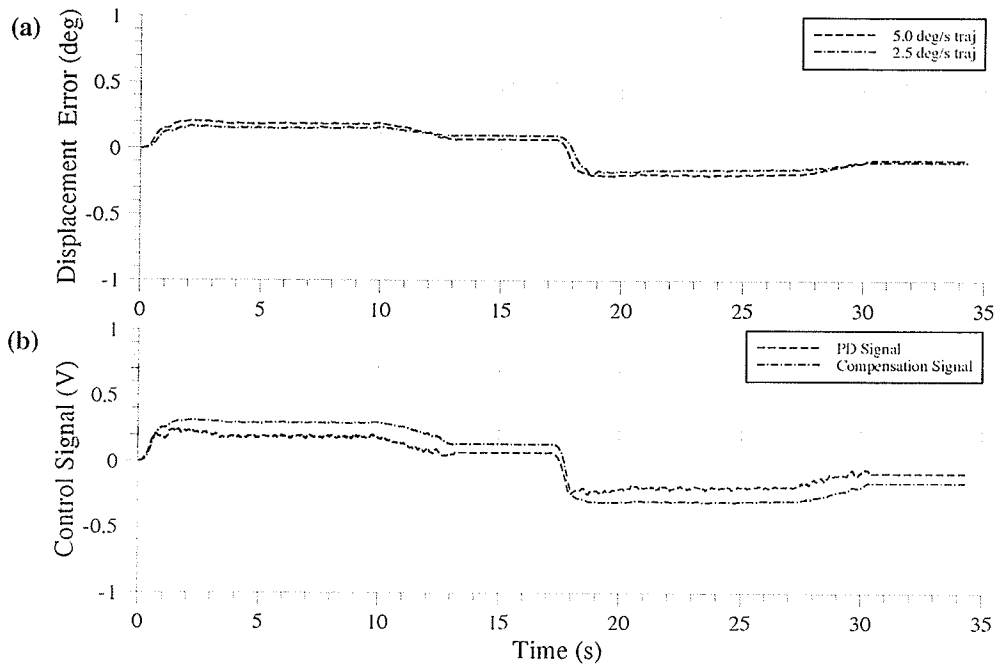

Figure 43 PD control w/SRNF compensation, Robustness Test 4: (a) displacement errors; (b) 5.0 deg/s control signal breakdown.

3.3.8.2 Friction Tests

To bring yet further insight into the SRNF compensator, 2.5 deg/s trajectory tests were performed to evaluate the effect of added friction. Only using the 2.5 deg/s trajectory from the benchmark was sufficient to display the added friction characteristics of the SRNF compensator. Two tests were performed: constant additional friction and variable additional friction. A summary of the test parameters are given in Table 19. Friction was added by simply wedging a wooden block to act as a brake in between a stationary and moving part of the DK robot base axis. Variable friction was added by manually applying the wooden wedge occasionally during the execution of the trajectory.

The friction performance results revealed a number of characteristics. For one, the SRNF compensator is not adaptive. As shown in Figure 44, when friction is added, the compensator only eliminates the amount of friction it was previously assigned. The

additional friction therefore remains uncompensated. Similar to when friction was added, the SRNF compensator did not adjust to the variable friction added to the system as shown in Figure 45. The friction compensation values should therefore be checked often using an offline identification algorithm or perhaps even an adaptive algorithm. From these observations, we could say that the SRNF compensator would work well in an environment where there is very little variation in friction.

Table 19 Parameters for SRNF compensation Friction Test.

Test	Friction	v_{ms} (V)	α (deg^{-1})
1	added	0.49	20
2	varied	0.49	20

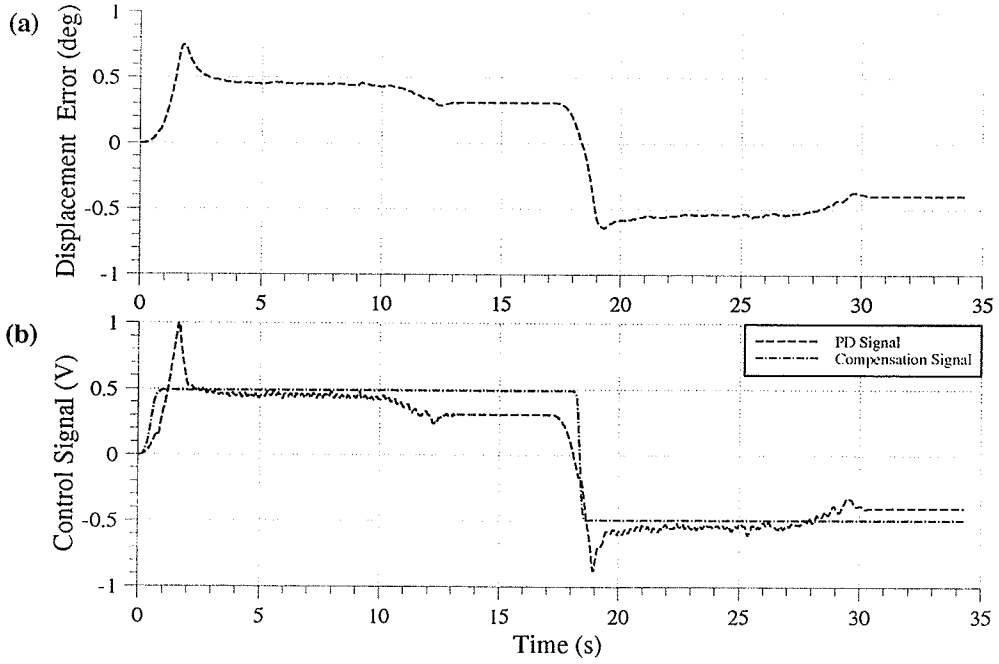

Figure 44 PD control w/SRNF compensation, Friction Test 1: (a) θ_e; (b) $v_c(t)$.

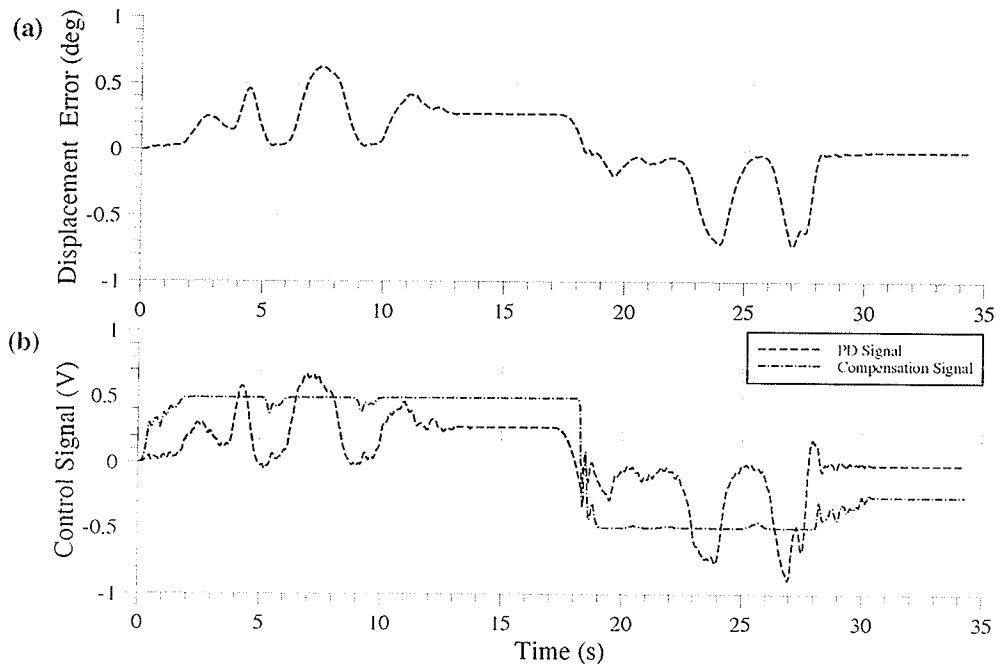

Figure 45 PD control w/SRNF compensation, Friction Test 2: (a) θ_e; (b) $v_c(t)$.

3.4 Simulation Comparison

Researchers often turn to simulation as a tool to help answer questions experimentation cannot answer. There are benefits for using simulators. For one, there is no responsibility of handling the expense of experimental equipment. The equipment could also be time-consuming for the setup. Simulations are flexible to study performance characteristics of a selected controller. In our case, the simulation comparison brings insight to the characteristics of the selected compensators that the experiments were unable to show. These simulations will also help in studying future selected compensators before experimentation.

The simulation architecture is based on the fourth-order Runge-Kutta fixed step algorithm [32]. A variation of Equation (26) is the dynamic equation used to model the base axis as follows:

$$\ddot{\theta}_a = \frac{nK_t K_a (v(t) - T_f - b\dot{\theta}_a)}{J} \tag{37}$$

where the input signal, $v(t)$, the friction torque, T_f, and the DC motor viscous friction, b, are all in units of volts. For modelling friction, we used the Karnopp friction model for this application according to Equation (1). Note that we are only using a one-degree-of-freedom gravity-independent system, there is no concern for multiple-degree-of-freedom, gravity-dependent complications. The values of inertia, gear ratio, motor torque constant, and viscous friction, are required in the simulations. Inertia was determined by inputting a constant signal to the base axis, calculating the acceleration, simplifying Equation (26) to $T_i = J\ddot{\theta}_a$, and solving for J. The gear train on the base axis consisted of a large spur gear and a harmonic drive. The gear ratio was calculated by counting the number of teeth on the spur gear and multiplying that number by the given gear ratio of the harmonic drive which was located on the casing of the base axis motor. The values of motor torque constant and viscous friction were then determined by comparing the experimental to the simulation results of the PD controller. A summary of these parameters is given in Table 20 and the parameters for the Karnopp friction model is given in Table 21. The controller parameters for the selected compensators used in these simulations are the same as per Table 17. Joint velocities are calculated just as in the experiments from the joint position data using five-point linear regression.

Table 20 Parameters for DK robot base axis.

Parameter	Value
J, base axis inertia	20 kg·m^2
n, gear ratio	1800
b, DC motor viscous friction	0.02 V/(deg/s)
K_t, DC motor torque constant	0.10 N·m/A
K_a, current amplifier gain	3.0 A/V

Table 21 Karnopp friction model parameters for DK robot simulations.

Parameter	Value
D_v, static velocity range	1.0x10^{-4} deg/s
T_s, maximum static friction torque	0.40 V
T_d, dynamic friction torque	0.38 V

3.4.1 PD Control

The simulated responses for the PD controller were very accurate to its experimental counterpart. The simulated responses to the three step inputs shown in Figure 46 are identical to those of the actual experiments: each step input response displayed the different effects of a PD controller when stick-slip friction has a significant influence on the system. The simulated trajectory responses as shown in Figure 47 also show similarities to the experimental results but with less noise present. This presence of less noise in the simulation could mean that some source of noise generation was not considered in the simulator mathematical model. There is no induced noise in these simulations. The additional noise in the experiments which are not included in the simulations are due to sources such as electrical noise and gear backlash.

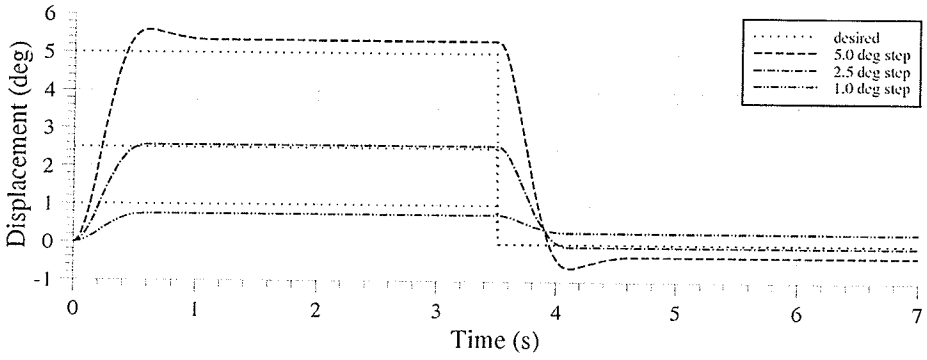

Figure 46 Simulated PD control step responses: (a) displacements; (b) 5.0 deg control signal breakdown.

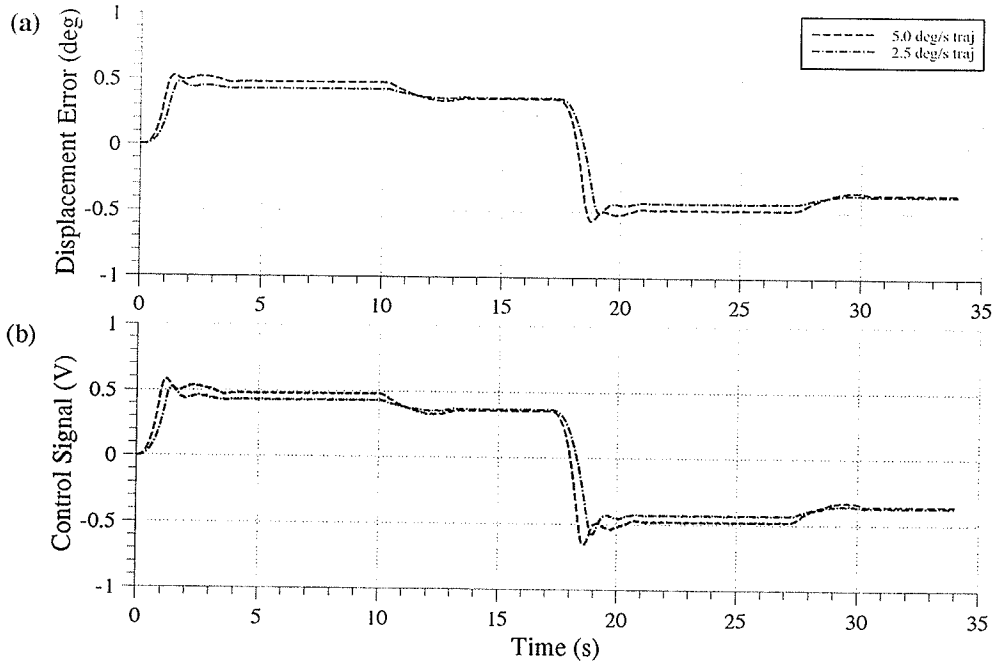

Figure 47 Simulated PD control trajectory responses: (a) displacement errors; (b) 5.0 deg/s control signal breakdown.

3.4.2 Reset Integral

The reset integral action simulation was hunting around the set point in the step responses just as in the experimental results as shown in Figure 48. This enforces what was observed earlier in the experimental responses and what was cited by others [33,43]. The friction present in our experiments is therefore stick friction. The trajectory responses as shown in Figure 49 are similar to the experimental results.

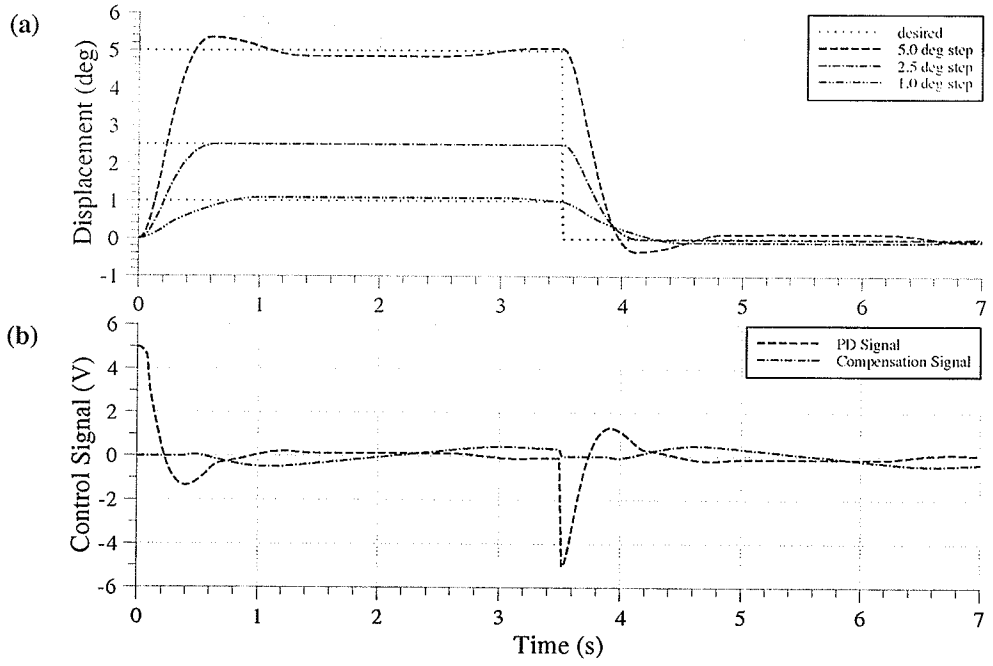

Figure 48 Simulated PD control w/RI compensation step responses: (a) displacements; (b) 5.0 deg control signal breakdown.

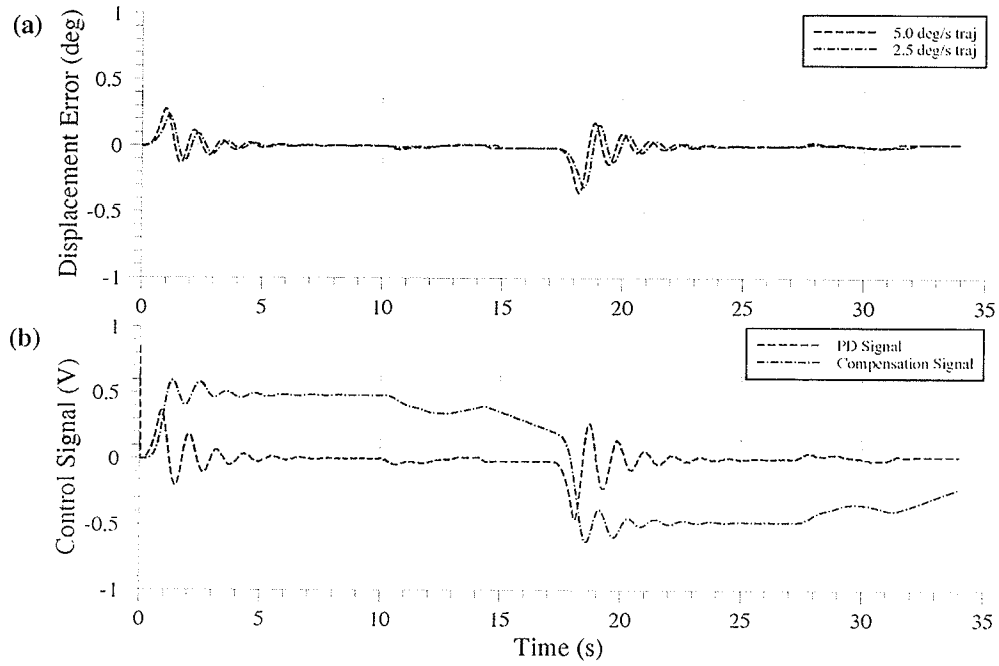

Figure 49 Simulated PD control w/RI compensation trajectory responses: (a) displacement errors; (b) 5.0 deg/s control signal breakdown.

3.4.3 Rate Variable Integral

The simulated results of the RVI action are shown in Figure 50 and Figure 51 for the step and trajectory responses, respectively, and are similar to the experimental results except for less noise in the tracking errors in the trajectory responses. Similar bang-bang action occurs near the zero error just as in the experimental results. This is due to the integral control signal hunting around zero error.

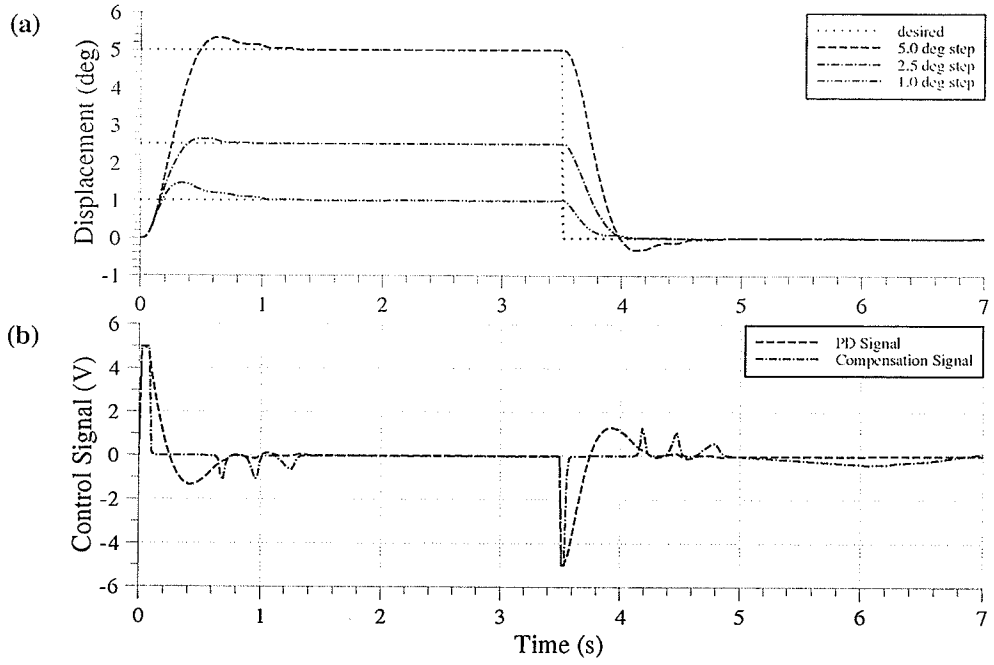

Figure 50 Simulated PD control w/RVI compensation step responses: (a) displacements; (b) 5.0 deg control signal breakdown.

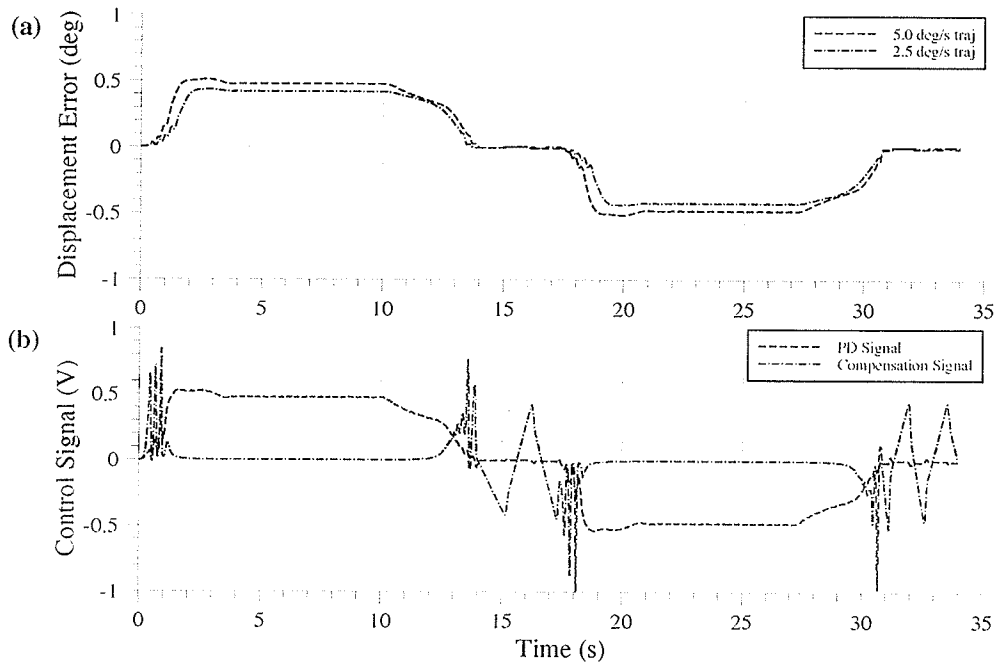

Figure 51 Simulated PD control w/RVI compensation trajectory responses: (a) displacement errors; (b) 5.0 deg/s control signal breakdown.

3.4.4 Reset Offset Integral

The ROI step responses as shown in Figure 52 display similarities to the experimental results and the trajectory responses as shown in Figure 53 display more oscillations than those in the experimental results. These increases in oscillations could be due to a slight deviation of the physical properties used in the simulation.

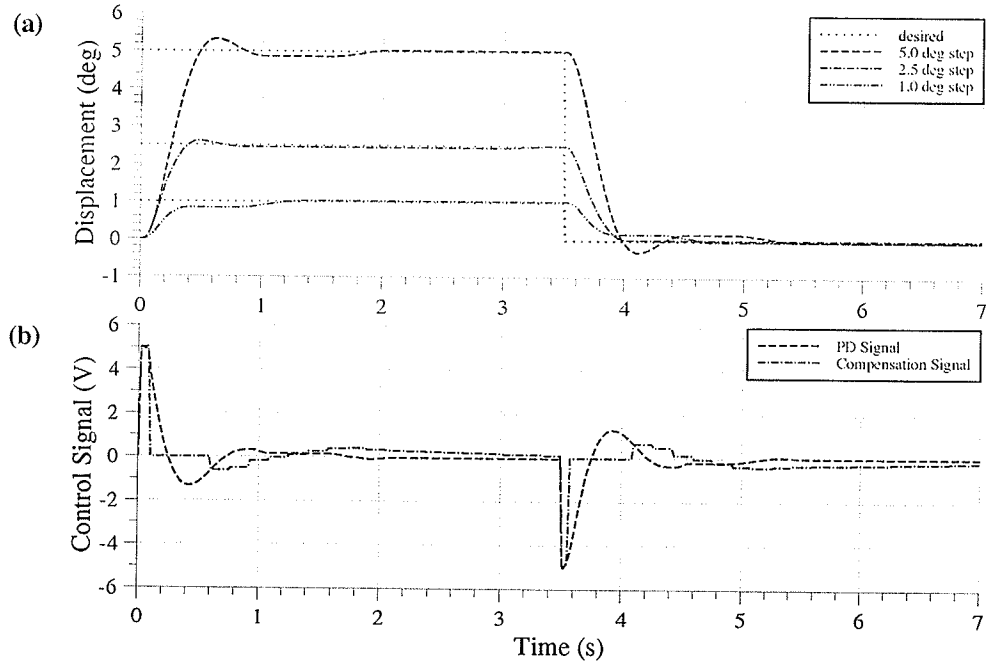

Figure 52 Simulated PD control w/ROI compensation step responses: (a) displacements; (b) 5.0 deg control signal breakdown.

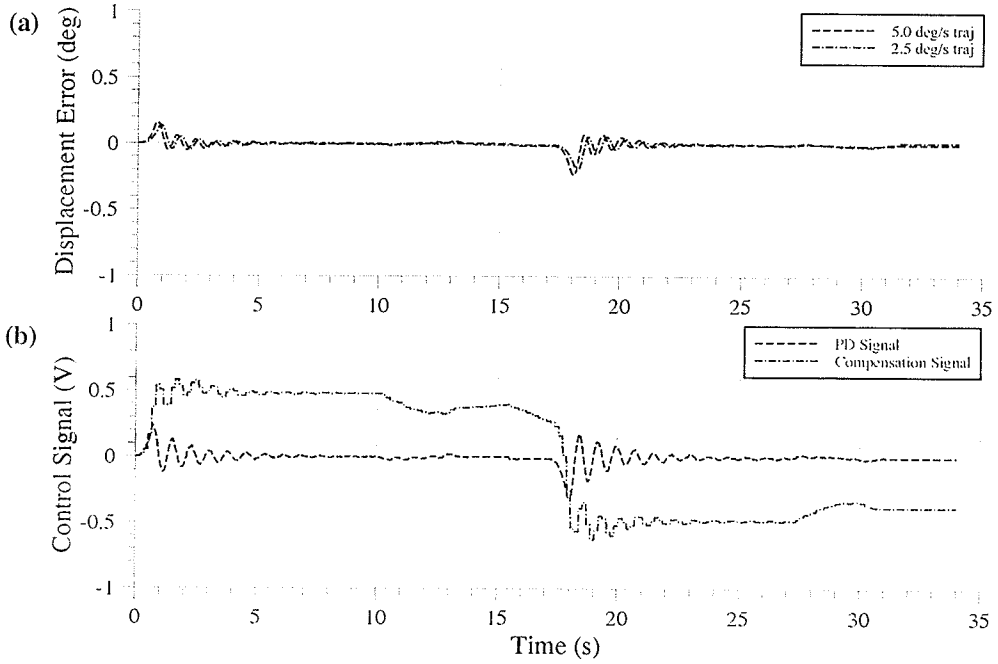

Figure 53 Simulated PD control w/ROI compensation trajectory responses: (a) displacement errors; (b) 5.0 deg/s control signal breakdown.

3.4.5 Feedforward Compensation

The simulated step responses given in Figure 54 display accurate results compared to the experiments but the trajectory responses given in Figure 55 are slightly different to the actual responses. This discrepancy could be once again due to a slight deviation of the physical properties used in the simulation. Bang-bang action is still present but not as prominent which could be the result of the absence of backlash in the gear train or less noise present in the control signal.

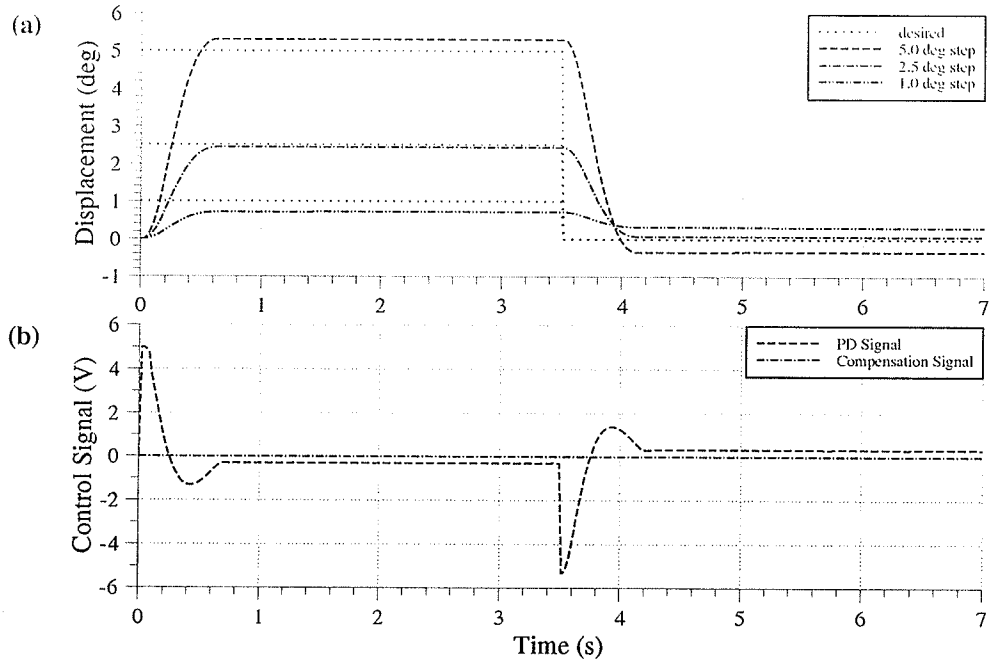

Figure 54 Simulated PD control w/Feedforward compensation step responses: (a) displacements; (b) 5.0 deg control signal breakdown.

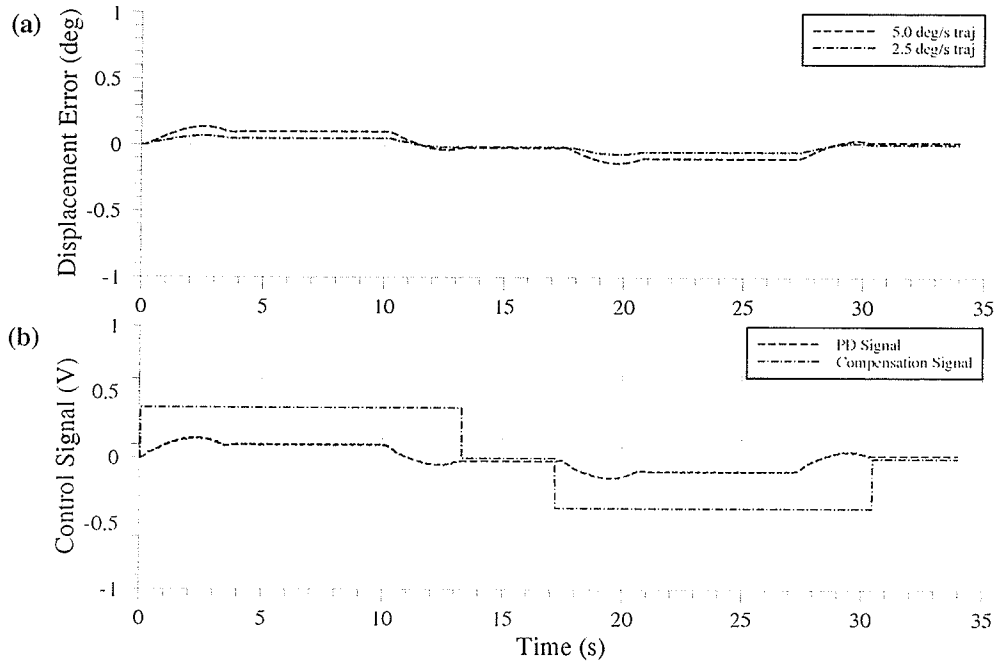

Figure 55 Simulated PD control w/Feedforward compensation trajectory responses: (a) displacement errors; (b) 5.0 deg/s control signal breakdown.

3.4.6 Discontinuous Nonlinear Proportional Feedback

The simulated responses of the DNPF compensator is given in Figure 56 and Figure 57 for step and trajectory responses, respectively. Just as in the experimental responses, these responses also show the oscillations at the 2.5 deg step input responses. A limit cycle must be present for that area of the system.

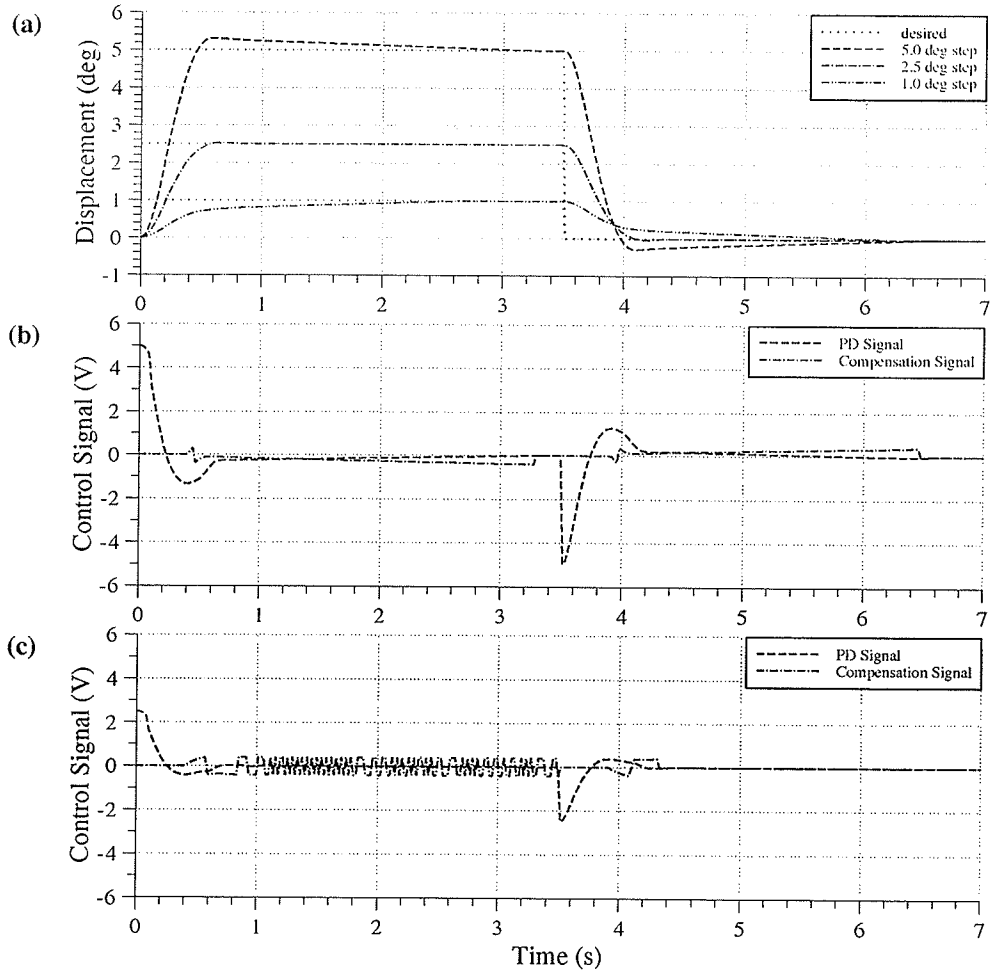

Figure 56 Simulated PD control w/DNPF compensation step responses: (a) displacements; (b) 5.0 deg control signal breakdown; (c) 2.5 deg control signal breakdown.

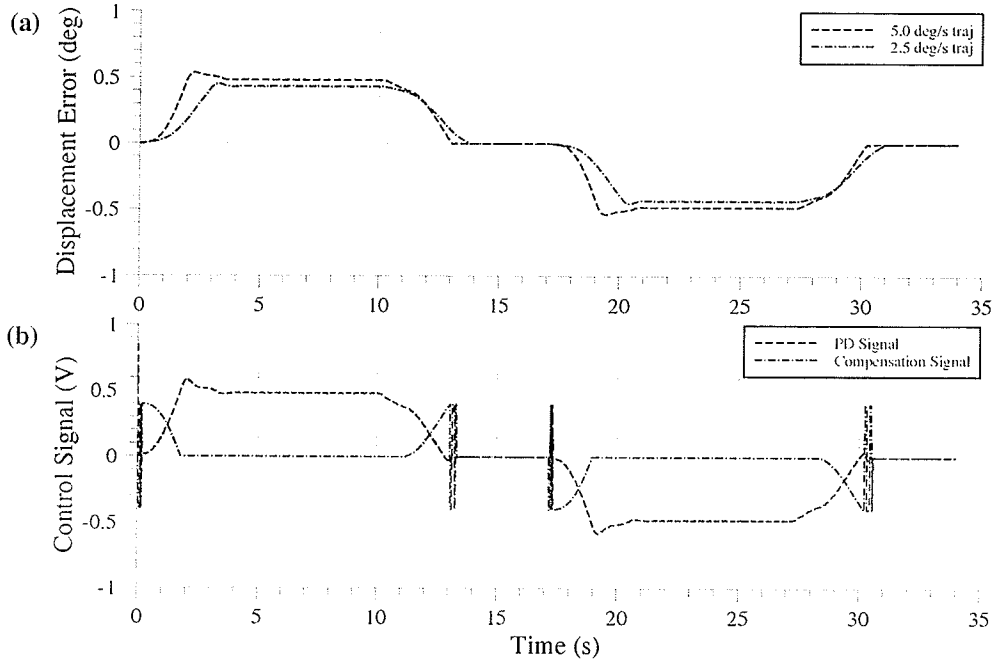

Figure 57 Simulated PD control w/DNPF compensation trajectory responses: (a) displacement errors; (b) 5.0 deg/s control signal breakdown.

3.4.7 Smooth Robust Nonlinear Feedback

The simulated responses to the SRNF compensator are given in Figure 58 and Figure 59 for the step and trajectory responses, respectively. The step responses are accurate to the actual responses. As for the trajectory responses, once again less noise is present in the control signal and differences in tracking errors is present due to no viscous friction compensation.

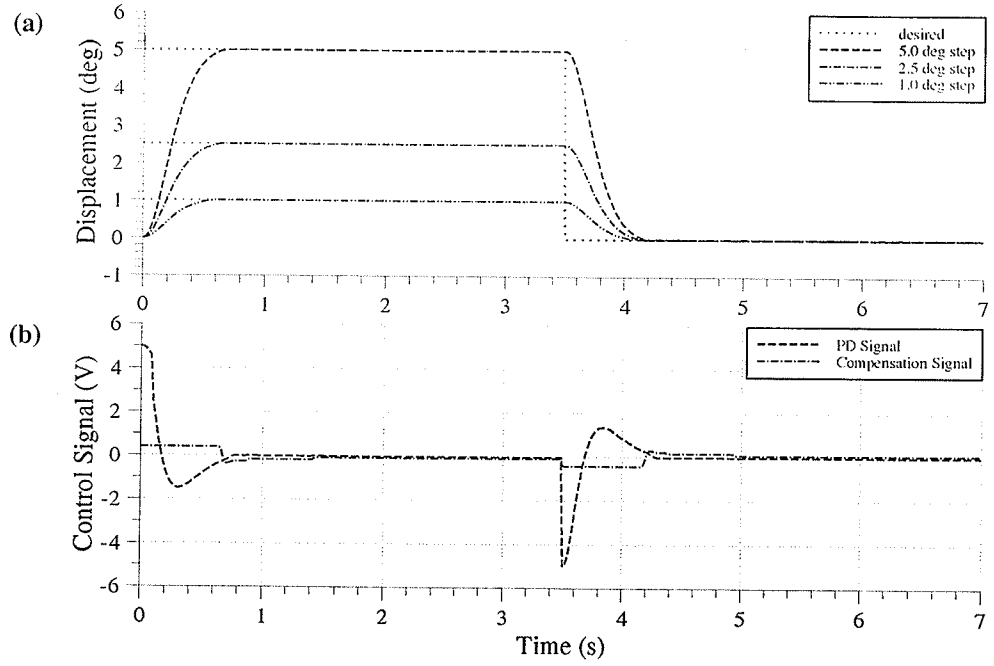

Figure 58 Simulated PD control w/SRNF compensation step responses: (a) displacements; (b) 5.0 deg control signal breakdown.

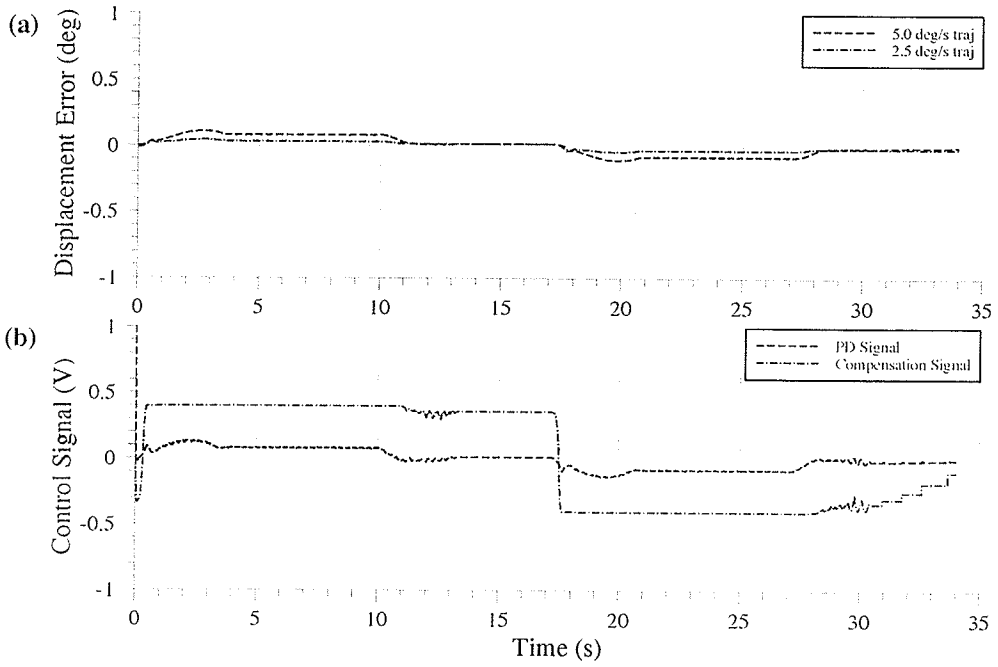

Figure 59 Simulated PD control w/SRNF compensation trajectory responses: (a) displacement errors; (b) 5.0 deg/s control signal breakdown.

3.5 Summary

This chapter documented the digital implementation and evaluation of selected integral and nonlinear feedforward and feedback controllers for compensating the effects of stick-slip friction. The analyses comprising of simulation and experimental components were conducted on the base axis of an instrumented, industrial electric robot with harmonic gear drives.

Performing these experiments fulfilled the featured friction compensators' experimental potential and brought valuable insight to their techniques. The RI compensator fails to eliminate the effects of friction through producing oscillations and therefore displays the need for a better friction compensator. The RVI compensator eliminates steady-state errors from stick friction; however, it does not eliminate tracking errors from slip friction. The ROI compensator improves the performance of the integral control by reducing the startup errors and oscillations caused by the interaction of friction and integral gain. The feedforward compensator eliminates noise generated from feedback compensation and creates a smoother compensation signal. The DNPF compensator eliminates the steady-state errors due to static friction; however, it has no slip friction compensation. The SRNF compensation method eliminates the majority of the position errors caused by stick-slip friction in both regulating and tracking tasks with the least amount of unwanted control signal oscillations compared to the other compensators.

Chapter 4 Conclusions

4.1 Contributions

This study contributes to the areas of stick-slip friction simulation and compensation. Stick-slip friction is first studied by analysing two distinct models, the Karnopp model and the Reset Integrator model, in terms of simplicity of the model, computing time, and accuracy to the classical stick-slip friction model. The Karnopp model has quicker computing times and resembles closer the classical friction model than the Reset Integrator model but is unique for each different application. The Reset Integrator on the other hand, is flexible to apply on different applications but is not accurate in resembling the classical friction model and the computation times are slower than those of the Karnopp friction model.

Six selected stick-slip friction compensation techniques on a PD-based controller are then studied on a one-degree-of-freedom, gravity-independent robot manipulator in both experiments and simulations, namely, three integral methods (RI, RVI, and ROI), one slip friction feedforward method, and two feedback methods (DNPF and SRNF). The tests performed on the selected friction models and compensation techniques in this study brought insight to their characteristics. The RI compensator eliminates steady-state errors from slip friction but hunts about the zero displacement error when compensating for stick friction. The RVI compensator eliminates the errors from stick friction but it does not compensate for slip friction. The ROI compensator eliminates the steady-state errors from slip friction and stick friction similar to that of the RI compensator but it does not hunt about the zero displacement error when compensating for stick friction. The slip friction feedforward method compensates for slip friction using a smooth signal; however, it does not compensate for stick friction. The DNPF compensator eliminates only errors from stick friction using a bang-bang compensation and sometimes hunts about the zero

displacement error. The SRNF compensator eliminated both stick and slip friction errors using the *tanh*(...) function with the minimal amount of oscillations compared to the other selected compensators. Overall, the RVI, ROI, Feedforward, and SRNF compensators demonstrate potential in creating more accurate and simpler compensators for friction, the SRNF compensator displaying the most potential.

4.2 Recommendations

In the area of friction simulations, one may contribute to the improvement of the Karnopp friction model towards its flexibility to different applications as well as improvements to handling kick-back accelerations in multiple-degree-of-freedom manipulators. One possible approach to handling the kick-back accelerations would be to add a hyperbolic function (such as in the SRNF compensator) to smooth out the transitions between stick and slip.

It is also recommended to continue studies on the ROI, RVI, Feedforward, and SRNF compensators. These compensators could implement viscous components in their algorithms and perhaps some of these compensators could be combined to make up a hybrid compensator. Multiple-degree-of-freedom, gravity-dependent tests should also be performed to study the effects of acceleration and gravity on these compensators.

References

[1] Armstrong-Hélouvry, B., Dupont, P., Canudas de Wit, C. 1994. A Survey of Models, Analysis Tools and Compensation Methods for the Control of Machines with Friction. *Automatica.* v.30. no.7. pp. 1083-1138.

[2] Armstrong-Hélouvry, B. 1993. Stick Slip and Control in Low-Speed Motion. *IEEE Transactions on Automatic Control.* v.38. no.10. pp.1483-1496.

[3] Armstrong-Hélouvry, B. 1993. Friction Modelling for Control. *Proceedings of the 1993 American Control Conference.* San Francisco, CA. v.2. pp.1905-1909.

[4] Armstrong, B. 1988. Friction: Experimental Determination, Modelling, and Compensation. *Proceedings: 1988 IEEE International Conference on Robotics and Automation.* Philadelphia, PA. v.3. pp.1422-1427.

[5] Bona, B., Indri, M. 1993. Friction Compensation and Robust Hybrid Control. *Proceedings: 1993 IEEE International Conference on Robotics and Automation.* Atlanta, GA. pp.81-86.

[6] Cai, L., Song, G. 1993. A Smooth Robust Nonlinear Controller for Robot Manipulators with Joint Stick-Slip Friction. *Proceedings: 1993 IEEE International Conference on Robotics and Automation.* Atlanta, GA. v.3. pp.449-454.

[7] Canudas de Wit, C. 1993. Robust Control for Servo-mechanisms Under Inexact Friction Compensation. *Automatica.* v.29. no.3. pp.757-761.

[8] Canudas de Wit, C., Noël, P., Aubin, A., Brogliato, B. 1991. Adaptive Friction Compensation in Robot Manipulators: Low Velocities. *The International Journal of Robotics Research.* v.10. no.3. pp.189-199.

[9] Canudas, C., Åström, K.J., Braun, K. 1986. Adaptive Friction Compensation in DC Motor Drives. *Proceedings: 1986 IEEE International Conference on Robotics and Automation.* San Francisco, CA. v.3. pp.1556-1561.

[10] Craig, J.J. 1989. *Introduction to Robotics: Mechanics and Control.* Reading, MA. Addison-Wesley. Ch. 6. pp.214-215.

[11] Dupont, P., Armstrong-Hélouvry, B. 1993. Compensation Techniques for Servos with Friction. *Proceedings of the 1993 American Control Conference.* San Francisco, CA. v.2. pp.1915-1919.

[12] Gautier, M., Khalil, W. 1988. On the Identification of the Inertial Parameters of Robots. *Proceedings: 1988 IEEE International Conference on Robotics and Automation.* Philadelphia, PA. v.3. pp.1683-1687.

[13] Gibson, J.E. 1963. *Nonlinear Automatic Control.* New York, NY. McGraw-Hill. Ch. 7. pp.237-290.

[14] Gogoussis, A., Donath, M. 1990. A Method for Real Time Solution of the Forward Dynamics Problem for Robots Incorporating Friction. *Journal of Dynamic Systems, Measurement, and Control.* v.112. no.4. pp.630-639.

[15] Gogoussis, A., Donath, M. 1988. Coulomb Friction Effects on the Dynamics of Bearings and Transmissions in Precision Robot Mechanisms. *Proceedings:*

1988 IEEE International Conference on Robotics and Automation. Philadelphia, PA. v.3. pp.1440-1446.

[16] Gogoussis, A., Donath, M. 1987. Coulomb Friction Joint and Drive Effects in Robot Mechanisms. *Proceedings: 1987 IEEE International Conference on Robotics and Automation.* Raleigh, NC. v.2. pp.828-836.

[17] Gomes, S.C.P., Chétien, J.P. 1992. Dynamics Modelling and Friction Compensated Control of a Robot Manipulator Joint. *Proceedings: 1992 IEEE International Conference on Robotics and Automation.* Nice, France. v.2. pp.1429-1435.

[18] Goyal, S., Ruina, A. Papadopoulos, J. 1991. Planar Sliding with Dry Friction. *Wear.* v.143. n.2. pp.307-352.

[19] Guglielmo, K., Sadegh, N. 1991. A New Adaptive Controller with Generalized Friction Estimation. *Dynamic Systems and Control.* v.33. pp.37-44.

[20] Haessig, D.A., Friedland, B. 1991. On the Modelling and Simulation of Friction. *Journal of Dynamic Systems, Measurement, and Control.* v.113. no.3. pp.354-362.

[21] Held, V., Maron, C. 1988. Estimation of Friction Characteristics, Inertial and Coupling Coefficients in Robotic Joints Based on Current and Speed Measurements. *IFAC Robot Control.* n.10. pp.207-212.

[22] Karnopp, D. 1985. Computer Simulation of Stick-Slip Friction in Mechanical Dynamic Systems. *Journal of Dynamic Systems, Measurement, and Control.* v.107. no.1. pp.100-103.

[23] Kolston, P.J. 1988. Modelling Mechanical Stick-Slip Friction Using Electrical Circuit Analysis. *Journal of Dynamic Systems, Measurement, and Control.* v.110. no.4. pp.440-443.

[24] Koren, Y. 1985. *Robotics for Engineers.* New York. McGraw-Hill.

[25] Kubo, T., Anwar, G., Tomizuka, M. 1986. Application of Nonlinear Friction Compensation to Robot Arm Control. *Proceedings: 1986 IEEE International Conference on Robotics and Automation.* San Francisco, CA. v.2. pp.722-727.

[26] Mabie, H.H., Rienholtz, C.F. 1987. *Mechanisms and Dynamics of Machinery.* 4th Edition. New York. John Wiley and Sons.

[27] Marilier, T., Richard, J.A. 1989. Nonlinear Mechanical and Electric Behaviour of a Robot Axis with a "Harmonic Drive" Gear. *Robotics and Computer-Integrated Manufacturing.* v.5. n.2/3. pp.129-136.

[28] Moore, D.F. 1975. *Principles and Applications of Tribology.* New York. Pergamon Press.

[29] Morse, R.A., Day, C.P., Stoddard, K.A. 1990. *Positional Control Method and System Utilizing Same.* U.S. Patent #4,727,303. Date of Patent: 23 February 1988.

[30] Ogata, K. 1990. *Modern Control Engineering.* New Jersey. Prentice Hall.

[31] Paul, R.P. 1981. *Robot Manipulators: Mathematics, Programming, and Control: the Control of Robot Manipulators.* Cambridge, MA. MIT Press.

[32] Press, W.H., Flannery, B.P., Teukolsky, S.A., Vetterling, W.T. 1988. *Numerical Recipes in C.* New York. Cambridge University Press.

[33] Radcliffe, C.J., Southward, S.C. 1990. A Property of Stick-Slip Friction Models which Promotes Limit Cycle Generation. *Proceedings of the 1990 American Control Conference.* San Diego, CA. v.2. pp.1198-1203.

[34] Schäfer, U., Brandenburg, G. 1993. Model Reference Position Control of an Elastic Two-Mass System with Compensation of Coulomb Friction. *Proceedings of the 1993 American Control Conference.* San Francisco, CA. v.2. pp.1937-1941.

[35] Sepehri, N., Corbet, T., Lawrence, P. 1995. Fuzzy Control of Robots with Flow Deadband Nonlinearities. *International Journal of Mechatronics.* v.5. pp.623-643.

[36] Sepehri, N., Lawrence, P.D., Sassani, F. 1989. Gear Backlash and Stick-Slip Friction in a Teleoperated Heavy-Duty Hydraulic Manipulator. *Canadian Conference on Electrical and Computer Engineering.* Montreal, Canada. pp.45-48.

[37] Shinners, S.M. 1978. *Modern Control Theory and Application.* Reading, MA. Addison-Wesley. Ch.8. pp.369-472.

[38] Siljak, D.D. 1969. *Nonlinear Systems: The Parameter Analysis and Design.* New York. John Wiley & Sons.

[39] Southward, S.C., Radcliffe, C.J., MacCluer, C.R. 1991. Robust Nonlinear Stick-Slip Friction Compensation. *Journal of Dynamic Systems, Measurement and Control.* v.113. no.4. pp.639-644.

[40] Sun, Q., Anderson, J.N., Alouani, A.T. 1990. A Scheme for Estimating Joint Friction Using a Model-Based Controller. *Proceedings of the Annual Southeastern Symposium on System Theory.* Cookeville, TN. pp.137-140.

[41] Tomizuka, M. Horowitz, R., Anwar, G., Jia, Y.L. 1988. Implementation of Adaptive Techniques for Motion Control of Robotic Manipulators. *Journal of Dynamic Systems, Measurement, and Control.* v.110. no.1. pp.62-69.

[42] Tomizuka, M., Jabbari, A., Horowitz, R., Auslander, D.M., Denome, M. 1985. Modelling and Identification of Mechanical Systems with Nonlinearities. *IFAC Identification and System Parameter Estimation.* pp.845-850.

[43] Townsend, W.T., Salisbury, J.K.Jr. 1987. The Effect of Coulomb Friction and Stiction on Force Control. *Proceedings: 1987 IEEE International Conference on Robotics and Automation.* Raleigh, NC. v.2. pp.883-889.

[44] Tung, E.D., Anwar, G., Tomizuka, M. 1993. Low Velocity Friction Compensation and Feedforward Solution Based on Repetitive Control. *Journal of Dynamic Systems, Measurement, and Control.* v.115. no.2(a). pp.279-284.

[45] Tustin, A. 1947. The Effects of Backlash and of Speed Dependent Friction on the Stability of Closed-Cycle Control Systems. *Journal of the Institution of Electrical Engineers.* v.94(2A). pp.143-151.

[46] Volpe, R., Khosla, P. 1992. An Experimental Evaluation and Comparison of Explicit Force Control Strategies For Robotic Manipulators. *Proceedings of the 1992 IEEE International Conference on Robotics and Automation*. Nice, France. v.2. pp.1387-1393.

[47] Yang, Y.P., Chu, J.S. 1993. Adaptive Velocity Control of DC Motors with Coulomb Friction Identification. *Journal of Dynamic Systems, Measurement and Control*. v.115. no.1. pp.95-102.

Appendices

A.1 Independent Two-dof Spring-mass

The purpose of this simulation is to study the performances of the Karnopp and the Reset Integrator models in a two-degree-of-freedom situation with less dependence on either blocks. A diagram of the two-degree-of-freedom spring-mass is given in Figure 60. The dynamic equation for the independent, two-degree-of-freedom spring-mass is as follows:

$$\begin{pmatrix} K_1 V_o t \\ 0 \end{pmatrix} = \begin{bmatrix} m_1 & 0 \\ 0 & m_2 \end{bmatrix} \begin{pmatrix} \dot{V}_1 \\ \dot{V}_2 \end{pmatrix} + \begin{bmatrix} (K_1 + K_2) & -K_2 \\ -K_2 & K_2 \end{bmatrix} \begin{pmatrix} \int V_1 dt \\ \int V_2 dt \end{pmatrix} + \begin{pmatrix} F_{f1} \\ F_{f2} \end{pmatrix} \tag{38}$$

The properties and conditions used are given in Table 22, and the friction model parameters are given in Table 23. Results of the two models are given in Figure 61 and Figure 62. For this test, a sine wave is used as a position input for the simulation instead of a ramp position input for a given amount of time. The sine wave input will display the same frictional characteristics just as in the constant velocity input tests. Both results are quite similar to the previous spring-mass tests.

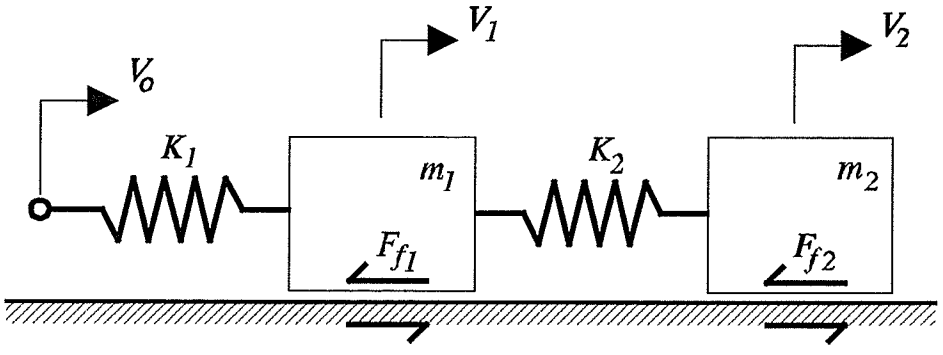

Figure 60 Independent two-dof spring-mass.

Table 22 Properties and conditions for independent, two-dof spring-mass.

Description	Block 1	Block 2
m_n, mass	0.1 kg	0.1 kg
F_{dn}, dynamic friction	1.6 N	1.6 N
F_{sn}, maximum static friction	2.4 N	2.4 N
K_n, spring constant	100 N/m	100 N/m
V_o, input velocity	$\pi/5 \cos(4\pi t)$ m/s	
t, time	0.7 s	

Table 23 Friction model parameters for independent, two-dof spring-mass.

Model	Parameter	Block 1	Block 2
Karnopp	D_{vn}, static velocity range	2.0×10^{-5} m/s	2.0×10^{-5} m/s
	F_{sn}, maximum static friction	2.4 N	2.4 N
	F_{dn}, dynamic friction	1.6 N	1.6 N
Reset Integrator	p_{on}, static friction range	1.0×10^{-5} m	1.0×10^{-5} m
	K_{rn}, spring rate	1.6×10^{5} N/m	1.6×10^{5} N/m
	β_n, damping coefficient	90 N/(m/s)	90 N/(m/s)
	a_n, static friction gradient	0.5	0.5

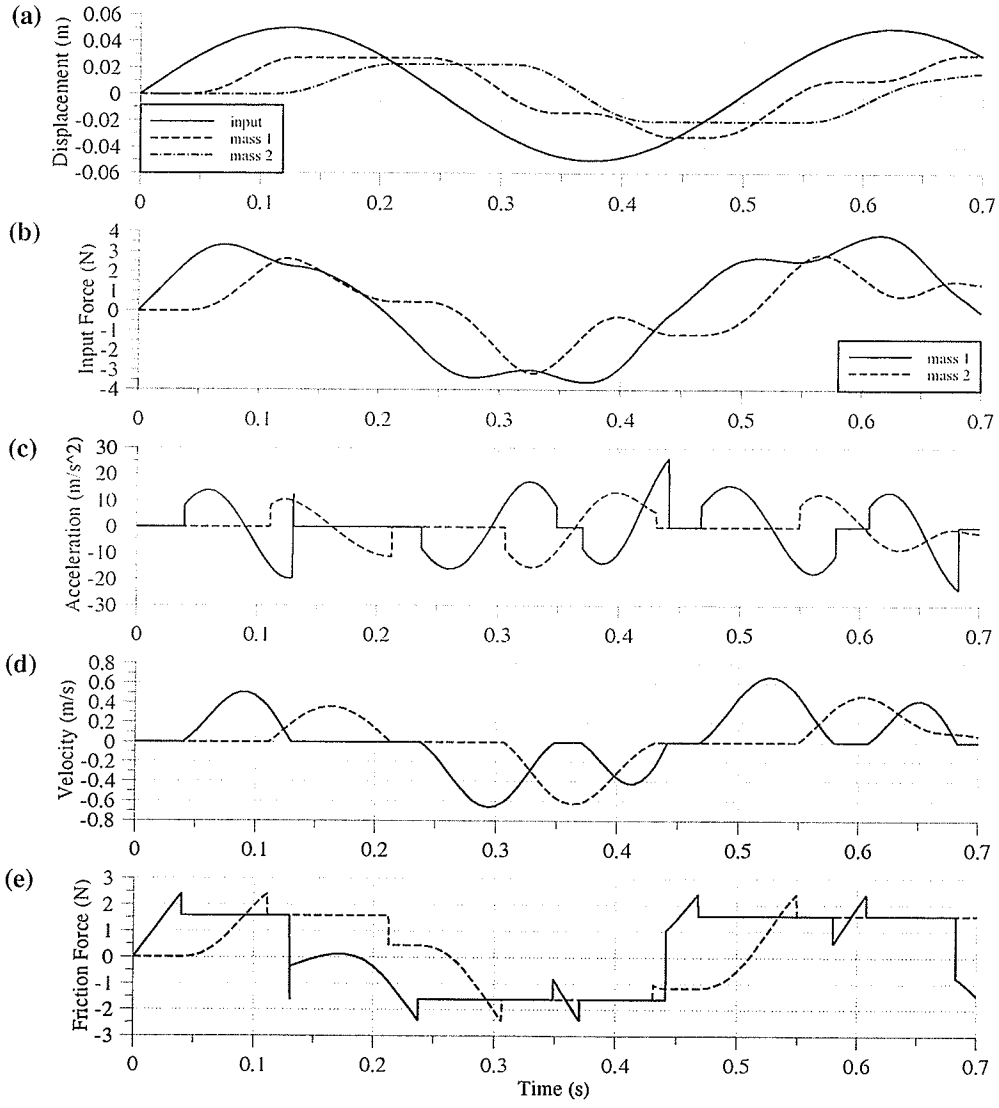

Figure 61 Independent two-dof spring-mass, Karnopp model: (a) displacements; (b) F_i; (c) $\dot{V}$; (d) V; and (e) F_f.

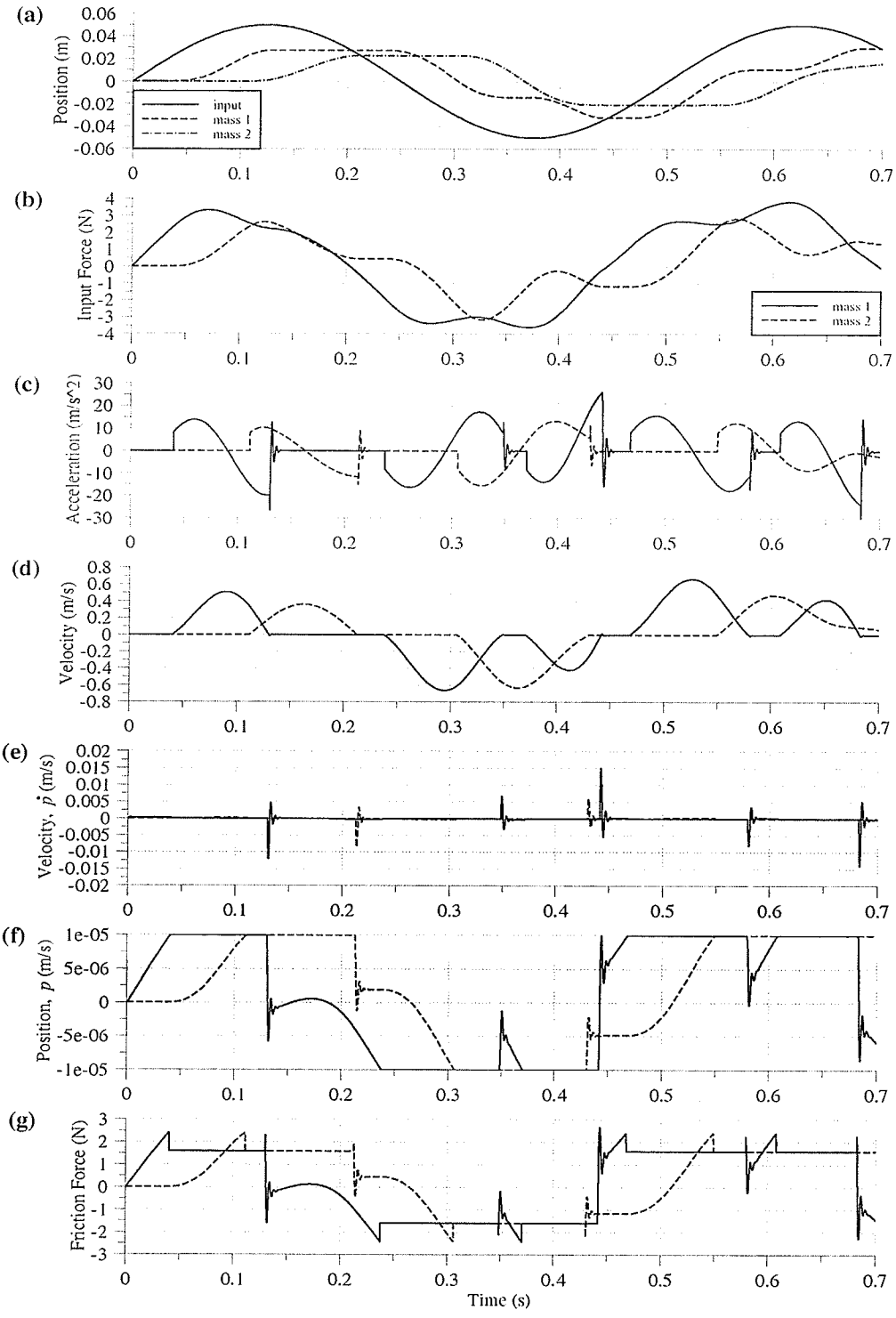

Figure 62 Independent two-dof spring-mass, Reset Integrator model: (a) displacements; (b) F_i; (c) $\dot{V}$; (d) V; (e) $\dot{p}$; (f) p; and (g) F_f.

A.2 Sensitivity Tests on Some Selected Compensators

Additional tests are performed on some of the selected compensators to study the effects of utilizing higher gain controls and their potential to friction compensation. PD control, PD control with RI compensation, PD control with ROI compensation, PD control with DNPF compensation and PD control with SRNF compensation are tested with high gains. The parameters used in these tests are given in Table 24. Only the trajectory tracking tests are used since the step input tests will generate signals much too large for the current amplifier hardware due to the large initial displacement errors. The trajectory tests have gradual initial increases in displacement errors and therefore do not have these large increases in the input signal. The results of these test are shown in Figure 63 to Figure 67 inclusive. All of these tests display a decrease in steady-state errors but an increase in oscillations found in the control signal and displacement errors. These oscillations are also visibly noticeable. Smaller oscillations are present in the lower control gain tests of Section 3.3. These high gain results reveal that increasing control gains reduce steady-state errors, but amplify oscillations. These oscillations are from unwanted noise present in the control system. High gains should therefore be avoided for stick-slip friction compensation since they amplify unwanted oscillations.

Table 24 Sensitivity parameters for some selected compensators.

Controller	K_p V/deg	K_d V/(deg/s)	Compensator Parameters
PD	5.0	0.25	N/A
PD w/RI		0.40	K_i=40.0 V/(deg·s), $\lvert \theta_e \rvert$ <0.5 deg
PD w/ROI		0.25	T_{roi}=300 ms, V_{roi}=2.33 deg/s
PD w/DNPF			θ_b=0.40 deg
PD w/SRNF			v_{ms}=0.40 V, α=100 deg^{-1}

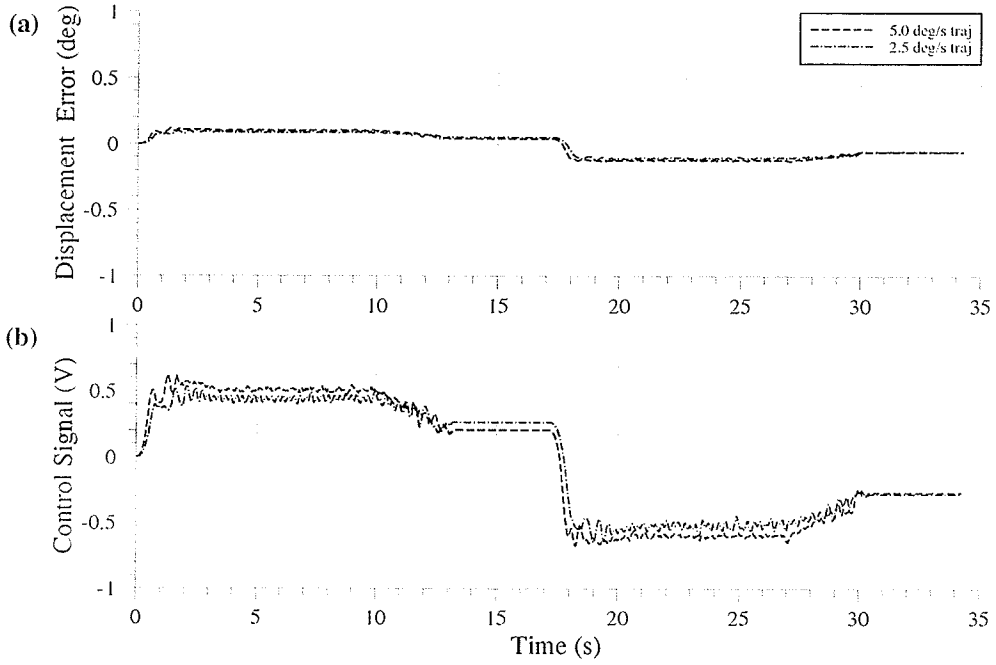

Figure 63 PD Control trajectory responses, Sensitivity Test: (a) displacement errors; (b) 5.0 deg/s control signal breakdown.

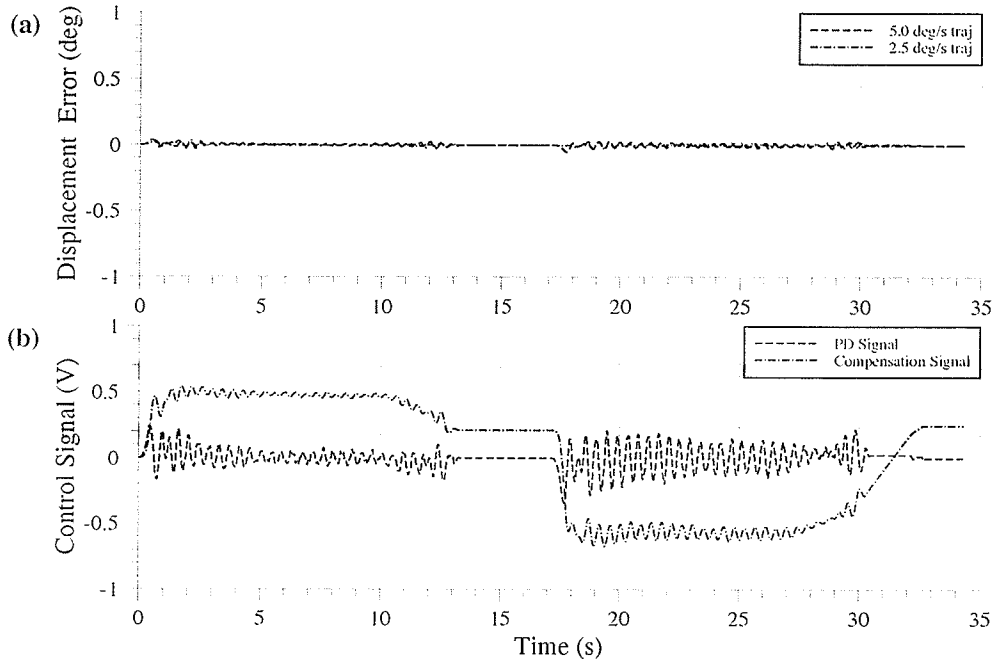

Figure 64 PD Control w/RI compensation trajectory responses, Sensitivity Test: (a) displacement errors; (b) 5.0 deg/s control signal breakdown.

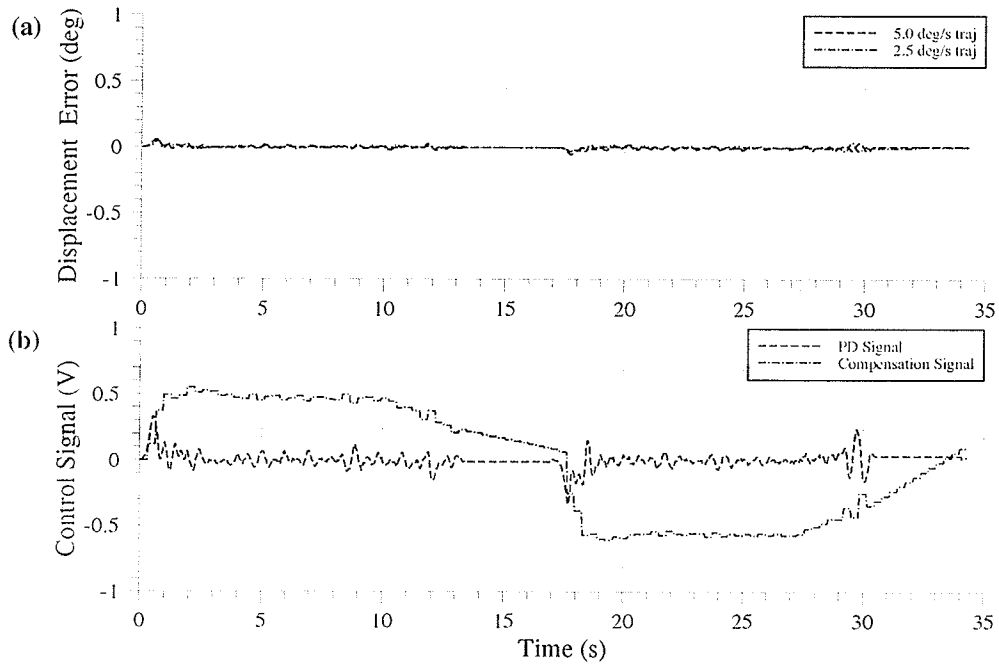

Figure 65 PD Control w/ROI compensation trajectory responses, Sensitivity Test: (a) displacement errors; (b) 5.0 deg/s control signal breakdown.

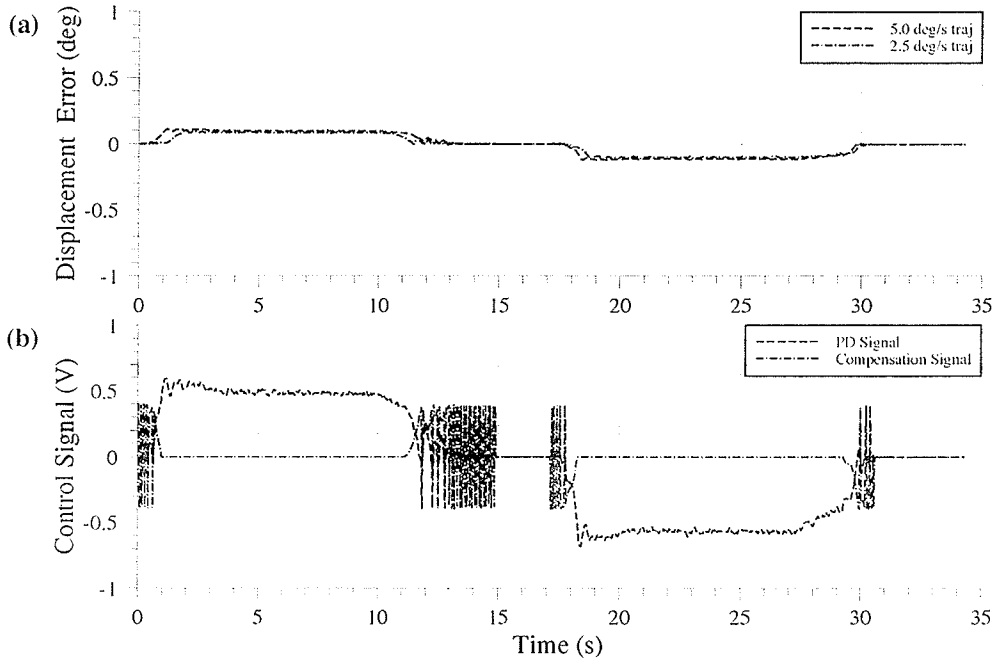

Figure 66 PD Control w/DNPF compensation trajectory responses, Sensitivity Test: (a) displacement errors; (b) 5.0 deg/s control signal breakdown.

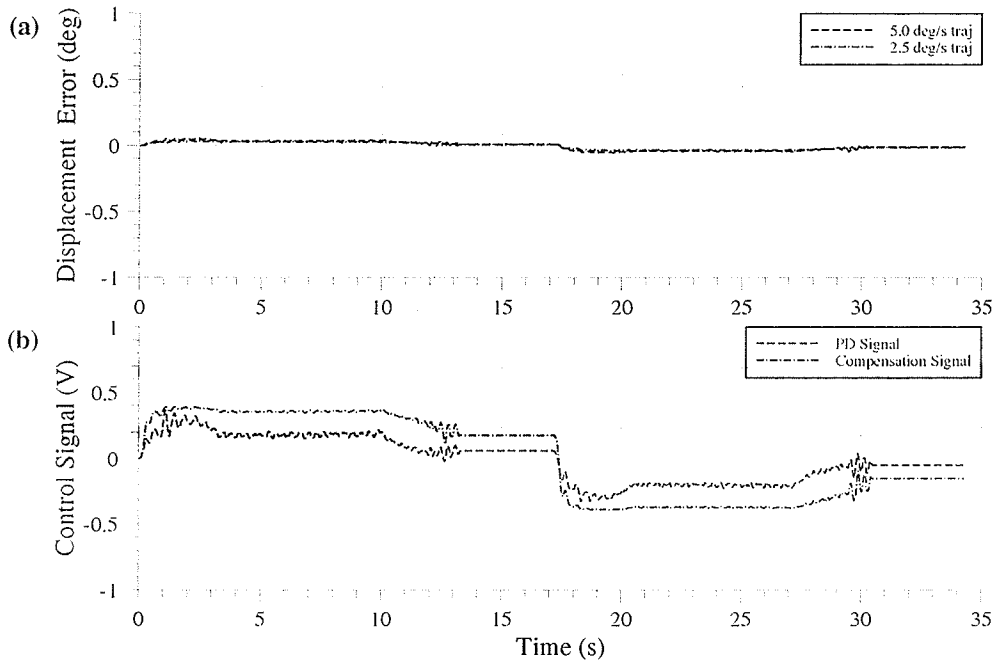

Figure 67 PD Control w/SRNF compensation trajectory responses, Sensitivity Test: (a) displacement errors; (b) 5.0 deg/s control signal breakdown.